Radiation and kinetics of high-temperature gas mixtures

Sean Mcguire

Habilitation à diriger des recherches

université PARIS-SACLAY

Radiation and kinetics of high-temperature gas mixtures

Habilitation à diriger des recherches de l'Université Paris-Saclay

présentée et soutenue à Gif-sur-Yvette, le 14 janvier 2025, par

Sean MCGUIRE

Composition du jury

Khaled HASSOUNI Professeur, Université Paris 13 Nord (LSPM)	Rapporteur
Arnaud BULTEL Professeur, Université de Rouen-Normandie (CORIA)	Rapporteur
Thierry MAGIN Professeur, Université Libre de Bruxelles	Rapporteur
Brigitte ATTAL-TRETOUT Directrice de recherche (émerite), ONERA	Examinatrice
David PAI Chargé de recherche, Laboratoire de Physique des Plasmas	Examinateur
Christophe LAUX Professeur, CentraleSupélec (EM2C)	Examinateur

université
PARIS-SACLAY

Titre : Rayonnement et Cinétique des Mélanges Gazeux à Haute Température

Mots clés : rentrée atmosphérique, plasma faiblement ionisé, rayonnement

Résumé : Ce manuscrit a été préparé dans le cadre de ma candidature au diplôme d'Habilitation à Diriger des Recherches de l'Université Paris-Saclay et est organisé en deux parties principales. La première partie comprend mon Curriculum Vitae, ainsi qu'un résumé de mes activités d'enseignement et de mes diverses responsabilités à CentraleSupélec. Le CV décrit les projets récents (subventions et collaborations), liste les étudiants et chercheurs postdoctoraux que j'ai encadrés, et détaille mes publications dans des revues à comité de lecture, conférences et chapitres de livres. La deuxième partie du manuscrit se concentre sur mes activités de recherche, en particulier celles impliquant le plasma inductif couplé au laboratoire EM2C de CentraleSupélec. Le dernier chapitre aborde les projets de recherche en cours et les perspectives de recherche futures.

Title : Radiation and kinetics of high-temperature gas mixtures

Keywords : atmospheric reentry, weakly-ionized plasma, radiation

Abstract : This manuscript has been prepared as part of my application for the “Habilitation à Diriger des Recherches” diploma at Université Paris-Saclay and is organized into two main parts. The first part includes my Curriculum Vitae, along with a summary of my teaching activities and various responsibilities at CentraleSupélec. The CV outlines recent projects (grants and collaborations), lists the students and postdoctoral researchers I have supervised, and details my publications in peer-reviewed journals, conferences, and book chapters. The second part of the manuscript focuses on my research activities, particularly those involving the inductively coupled plasma torch at CentraleSupélec’s EM2C laboratory. The final chapter discusses ongoing research projects and future research directions.

Table of Contents

Chapter 1 Introduction & CV

1.1 Overview

I obtained my PhD degree in Mechanical & Aerospace Engineering in September of 2015 from Princeton University, where my research was supervised by Prof. Richard Miles. In October of 2015, I joined the plasma research team at the EM2C laboratory (CNRS) as a postdoctoral researcher. My postdoctoral research focused on the implementation of optical diagnostics for the study of an inductively coupled plasma discharge. In 2017, I became a Maître de Conférences at CentraleSupélec, where I continue to work as part of the plasma research team at the EM2C laboratory. This chapter will present my curriculum vitae. The remaining chapters are organized as follows:

- Chapter 2 : Teaching activities
- Chapter 3 : Atmospheric entry research at EM2C (research overview and context)
- Chapter 4 : Fundamental radiation studies in the vacuum ultraviolet spectral region
- Chapter 5 : Chemical non-equilibrium studies in a CO_2/Ar mixture
- Chapter 6 : Chemical non-equilibrium studies in N_2/Ar and Air mixtures
- Chapter 7 : Conclusion and Discussion

Chapter 3 provides context for the research presented in Chapters 4 – 6. Chapter 7 includes a discussion of upcoming research activities.

1.2 Curriculum Vitae

Education and Academic Employment

Education

2006 – 2010	Whitworth University, Bachelor of Science (Physics) and Bachelor of Arts (Math)
2010 – 2015	Princeton University, PhD in Mechanical and Aerospace Engineering Thesis Supervisor: Richard Miles

Academic Employment

2015 – 2017	Postdoctoral Researcher, Laboratoire EM2C (CNRS)

2017 – present Maître de Conférences, CentraleSupélec
Plasma research team, laboratoire EM2C (CNRS)

Research Activities

Grants and Collaborations

Research Grants

2018 – 2022 Principal Investigator, ANR JCJC research grant "*CO2REC*" (252 828 €)

2021 – 2026 Partner, ERC Advanced Grant "*GreenBlue*" (Principal Investigator: Christophe Laux, 2 497 336 €)

2022 – 2024 Principal Investigator, Labex LaSIPS grant PlasmaCARS (57 500 €)

2024 – present Principal Investigator, ANR PRCE research grant "*CH4Kin*" (615 952 €)

Collaborations

2021 – 2025 NASA (Space Act agreement), *Studies of recombining plasma dynamics in N_2, CO_2, and air flows*

2022 – present ONERA, *Hybrid fs/ps CARS measurements in N_2/CH_4 plasmas*

2022 – present Princeton University, *Modeling of THz radiation from fs-filaments*

- Princeton Collaborative Low Temperature Plasma Research Facility award received in 2024

2023 University of Queensland, *LIF measurements of N atom density in a recombining N_2/CH_4 mixture*

2024 – present SPARK Cleantech, *Fundamental studies of methane plasmalysis dynamics in an NRP discharge*

Supervision

Doctoral Supervision

2016 – 2019 Augustin Tibère-Inglesse
Radiation of nonequilibrium recombining plasma flows

- 50% of supervision, Cifre thesis with ArianeGroupe
- 5 peer-reviewed publications, 2 conference papers

2018 – 2023 Corentin Grimaldi
Experimental study of a recombining CO_2 plasma

- 50% of supervision, thesis funded by CO2REC grant
- 3 conference papers (2 publications in preparation)

2022 – present Cyrine Merhaben

Experimental study of a recombining CH_4/N_2 plasma

- Director (waver obtained to direct thesis without HDR)
- 75% of supervision, thesis funded by doctoral school grant
- 1 conference paper

2023 – present Jean-Loup Du Garreau De La Méchenie

Study of the quenching reactions of excited nitrogen molecules: measurement of the quenching rate constants and the population densities of the produced species

- 30% of supervision

2024 – present Sara Delahaie

Experimental study of methane plasmalysis dynamics in an NRP discharge

- 33% of supervision, Cifre thesis funded by SPARK Cleantech

2024 – present Pierre-Antoine Goutier

Numerical study of methane plasmalysis dynamics in an NRP discharge

- 33% of supervision, Cifre thesis funded by SPARK Cleantech

Postdoctoral Supervision

2023 – present Laila Dakroub, co-supervised with ONERA

2024 – present Thomas Vazquez, co-supervised with Christophe Laux

Interns

2018 Mirae Leigh Parker (France-Stanford exchange program summer internship)

2019 Will Schlyder (summer internship, level M1)

2022 Cyrine Merhaben (Masters project, level M2)

2022 Mateo Benjamin Massey (France-Stanford exchange program summer internship)

2023 Hunter Hollenbeck (France-Stanford exchange program summer internship)

2023 Mragank Singh (6 month visiting doctoral student from University of Queensland)

Publications

Peer-reviewed publications

Tibère-Inglesse, A., McGuire, S., and Laux, C., *Inferring gas temperature from N_2 emission via rotational distributions of the N2 $B\ ^3\Pi_g$ and C $^3\Pi_u$ states*, Plasma Sources Science & Technology, 32 (7), 2023.

McGuire, S., Jacobs, C., Mariotto, P., Grimaldi, C., Tibère-Inglesse, A., and Laux, C., *Measurements and Modeling of Air Plasma Radiation in the VUV*, AIAA Journal of Thermophysics & Heat Transfer," 37 (4), 2023.

Tibère-Inglesse, A., McGuire, S., Mariotto, P., and Laux, C., *Measurements and Analysis of Rotational Temperatures obtained with Raman and Optical Emission Spectroscopy in a Nonequilibrium Nitrogen Plasma*, Plasma Sources Science & Technology, 30 (125019), 2021.

Tibère-Inglesse, A., McGuire, S., Mariotto, P., and Laux, C., *Experimental study of recombining nitrogen plasmas. Part II: Electronic population distributions and nonequilibrium radiation of atoms*, Plasma Sources Science & Technology, 30 (125020), 2021.

McGuire, S., Tibère-Inglesse, A., Mariotto, P., Cruden, B., and Laux, C. *Measurements and modeling of CO 4th positive (A - X) radiation*, Journ. of Quant. Spect. and Rad. Transf., 245 (106855), 2020.

Tibère-Inglesse, A., McGuire, S., Mariotto, P. and Laux, C., *Experimental study of recombining nitrogen plasmas: I. Vibronic population distributions and nonequilibrium molecular radiation*, Plasma Sources Science & Technology, 28 (7), 2019.

Tibère-Inglesse, A., McGuire, S., Mariotto, P., and Laux, C., *Validation cases for recombining nitrogen and air plasmas*, Plasma Sources Science & Technology, 27 (11), 2018.

McGuire, S., Tibère-Inglesse, A., and Laux, C., *Ultraviolet Raman spectroscopy of N_2 in a recombining atmospheric pressure plasma*, Plasma Sources Science & Technology, 26 (11), 2017.

McGuire, S., Tibère-Inglesse, A., and Laux, C., *Infrared spectroscopic measurements of Carbon Monoxide within a high temperature ablative boundary layer*, Journ. Physics D: Applied Physics, 49(48):485502, 2016.

Miles, R.B., *McGuire, S.*, et al., *New diagnostic methods for laser plasma- and microwave-enhanced combustion*, Phil. Trans. R. Soc. A, 373, 20140338 (2015)

McGuire, S. and Miles, R. B., *Collision induced ultraviolet structure in nitrogen radar REMPI spectra*, Journal of Chemical Physics, 141, 244301 (2014)

Book chapters

Laux, C., McGuire, S. *et al*., *Experimental investigation of meteorites : ground test facilities*, in *Hypersonic Meteoroid Entry Physics,* IOP publishing Ltd, 2019.

Conference papers

Merhaben, C., McGuire, S., and Laux, C. *Study of a reacting N_2/CH_4 plasma*, 2024 AIAA Scitech Meeting, (AIAA 2024-0448).

Grimaldi, C., McGuire, S., and Laux, C. *Infrared emission measurements of a recombining CO_2 plasma at atmospheric pressure*, 9th International Workshop on Radiation of High Temperature Gases, september 2022.

Grimaldi, C., McGuire, S., and Laux, C. *Infrared emission measurements of a recombining CO_2 plasma at atmospheric pressure*, 2022 AIAA Scitech Meeting, (AIAA 2022-1782).

Grimaldi, C., McGuire, S., Tibère-Inglesse, A., and Laux, C. *Infrared radiation measurements of a recombining CO2 plasma at atmospheric pressure*, 2021 AIAA Scitech Meeting, (AIAA 2021-0104).

McGuire, S., Tibère-Inglesse, A., Mariotto, P., Cruden, B. and Laux, C. *VUV radiation of high temperature CO_2/Ar plasma*, 2020 AIAA Scitech Meeting, (AIAA 2020-0732).
• Presented at AIAA Scitech 2020

Grimaldi, C., McGuire, S., and Laux, C. *Temperature and radiation measurements of an atmospheric pressure CO2 plasma*, 2020 AIAA Scitech Meeting, (AIAA 2020-1708).

McGuire, S., Tibère-Inglesse, A., and Laux, C. *Carbon monoxide radiation in an equilibrium plasma torch facility*, 2019 AIAA Aerospace Sciences Meeting, AIAA SciTech Forum, (AIAA 2019-1775).
• Presented at 56th AIAA Aerospace Sciences Meeting

Tibère-Inglesse, A., McGuire, S., and Laux, C. *Atomic radiation from a recombining nitrogen plasma*, 2019 AIAA Aerospace Sciences Meeting, AIAA SciTech Forum, (AIAA 2019-2068).

McGuire, S., Bailet, G. and Laux, C. *Development of a probe for in-situ radiative heat flux measurements at the surface of an ablator*, 2018 AIAA Aerospace Sciences Meeting, AIAA SciTech Forum, (AIAA 2018-0498).
• Presented at 56th AIAA Aerospace Sciences Meeting

Tibère-Inglesse, A., McGuire, S., and Laux, C. *Nonequilibrium radiation from a recombining nitrogen plasma*, 2018 AIAA Aerospace Sciences Meeting, AIAA SciTech Forum, (AIAA 2018-0241).

McGuire, S. and Laux, C., *Experimental analysis of atomic Carbon and Carbon Monoxide production within a high temperature ablative boundary layer*, 55th AIAA Aerospace Sciences Meeting, American Institute of Aeronautics and Astronautics, 2017.
• Presented at 55th AIAA Aerospace Sciences Meeting

McGuire, S. and Miles, R. B., *Methods for Enhancing Radar REMPI Sensitivity*, 53rd Aerospace Sciences Meeting, American Institute of Aeronautics and Astronautics, 2015.
• Presented at 53rd AIAA Aerospace Sciences Meeting

McGuire, S. and Miles, R. B., *Radar REMPI measurements of N2 rotational temperature*, 45th Plasmadynamics and Lasers Conference, American Institute of Aeronautics and Astronautics, 2014.
• Presented at AIAA 45th Plasmadynamics and Lasers Conference

McGuire, S., Chng, T. L. and Miles, R. B., *Nanosecond time-resolved 2+2 Radar REMPI measurements performed in molecular nitrogen*, 44th Plasmadynamics and Lasers Conference, American Institute of Aeronautics and Astronautics, 2013.
• Presented at AIAA 44th Plasmadynamics and Lasers Conference

McGuire, S., Zaidi, S., Dogariu, A. and Miles, R. B., *The intrinsic phase shift and its effect upon the measurement of airflow velocities using LITRA*, 51st AIAA Aerospace Sciences Meeting, American Institute of Aeronautics and Astronautics, 2013.
• Presented at 51st AIAA Aerospace Sciences Meeting

McGuire, S., Zaidi, S., Dogariu, A., Howard, P. and Miles, R. B., *Measuring the Velocity of a Supersonic Airflow Using Laser Ionization Tagged Radar Anemometry (LITRA)*, 50th AIAA Aerospace Sciences Meeting, American Institute of Aeronautics and Astronautics, 2012.
• Presented at 50th AIAA Aerospace Sciences Meeting

Other activities

Journal Referee: AIAA Journal of Thermophysics and Heat Transfer, Plasma Sources Science and Technology, Physics of Plasmas, Combustion and Flame, Applied Optics, Journal of Physics D : Applied Physics, Journal of Quantitative Spectroscopy and Radiative Transfer, European Physical Journal D, Physical Review E

Chapter 2 Teaching Activities

My teaching activities are primarily carried out within the « Mécanique, Energie et Procédes (MEP) » department at CentraleSupélec across the 3 years of engineering curriculum. As a lecturer, I have taught the Applied Thermodynamics and Unsteady Heat Transfer courses. The Applied Thermodynamics course was modified significantly as part of the merger between Ecole Centrale Paris and Supélec. In collaboration with Marie-Laurence Giorgi, I participated in the development of new course material and wrote part of the course manuscript (polycopie). As part of this effort, I have focused on including practical applications of classical Thermodynamics principles across several domains. These domains include plasma physics, climate science, propulsion/combustion, and chemical processing. In addition to the Applied Thermodynamics and Unsteady Heat Transfer lectures, I have also lectured for a portion of the Fluid Mechanics course (level M1) at the school. Specifically, I developed the course material for a Hypersonics thematic block which includes 3 lectures and requires the students to work in teams on one of several subjects related to a hypersonic vehicle (aerodynamics forces related to pressure and viscuous drag, heat transfer to the vehicle surface, shock geometry, etc.).

I have administered TDs in several courses – Heat Transfer (both at the L3 level and M2 level), Transport Physics (Sciences de Transfert, level L3), and Fluid Mechanics (level M1). Since beginning as a Maître de Conférences, I have participated in the Professional skills workshops (« Ateliers Pratiques de l'Ingenieur » and « Ateliers Projet Professionnel ») at CentraleSupélec. Finally, I have also participated in the supervision of several projects at all levels of the engineering curriculum at the school – mainly within the CentraleSupélec space center and within the 3rd year mention Effacité Energétique.

My current teaching responsibilities include the following activities:

- Manager and organizer of M2 level projects for students in the « *mention Effacité Energétique* », « *M2 Aeronautique et Spatial* », and « *M2 Transport et Conversion de l'Energie* » programs (~50 students total). The projects proposed to students include academic projects proposed by researchers at the school and projects proposed by industrial partners. My role as manager involves 3 primary tasks: 1) recruiting subjects, 2) coordinating projects with industrial partners, and 3) monitoring and evaluating projects.
- Co-director of the « Séquence Thématique 2: Transition Energétique », a level L3 sequence dealing with topics of relevance for a transition to carbon-neutral energy

sources (~100 students total). My role as co-director of this sequence is to help organize invited speaker seminars for the students, and to organize a 1-week integration course in partnership with EDF for ~50 students. This 1-week course requires students to use EDF software to assess and improve the energy consumption of a residential neighborhood.

The teaching activities summarized above are listed below.

Courses taught

Lectures

2018 – present **Applied Thermodynamics**

- Topics covered: thermodynamic cycles (open/closed), phase diagrams, thermodynamics of mixtures (binary and ternary), chemical thermodynamics

2024 – present **Unsteady heat transfer**

- Topics covered: Fourier's law of conduction, energy balance, nondimensional numbers and Buckingham Pi theorem, unsteady conduction through semi-infinite and finite size walls

TD (travaux dirigé)

2017 – 2018 **Heat Transfer, Level L3**

2017 – present **Heat Transfer, Level M2**

2018 – 2019 **Transport Physics (Sciences de Transfert)**

2020 – present **Fluid Mechanics**
*Developed material for thematic block focused on hypersonics

Other

2017 – present **Professional skills workshop** (« Ateliers Pratiques de l'Ingenieur », « Ateliers Projet Professionnel »)

2017 – present **Project supervision**

Teaching responsibilities

2017 – present	Project Organization - Organization of M2 level projects - ~ 50 students divided between several programs (mention Efficacité Energétique, M2 « Transport et Conversion de l'Energie », M2 « Aéronautique et spatial »)
2019 – present	Integrative module (« enseignement d'integration ») in partnership with EDF - ~ 50 students work in teams and use EDF thermal design software to model energy consumption of residential housing
2023 – present	ST2 covering energy transition (« séquence thématique » ST2 sur la transition energétique) - ~ 100 students introduced to challenges and potential solutions associated with transition to lower carbon energy sources - Organized with Mohamed Bensetti

Chapter 3 Atmospheric entry research at EM2C

My research involves the study of *plasmas* for engineering applications. The work that will be presented in the remaining chapters of this manuscript primarily targets applications involving hypersonic flight, especially atmospheric entry, wherein a space capsule enters a planet's atmosphere at hypersonic speeds. This will be the application invoked the most. However, the work presented is also relevant for the experimental characterization of high-enthalpy wind tunnels that are used to test hypersonic prototype vehicles. Other applications in the field of energy sciences will be cited where relevant. Finally, the scope of my recent work has expanded to include potential applications in other fields such as telecommunications. These new applications that I am targeting will be addressed in the final chapter looking at future work and perspectives.

This chapter has two primary goals. The first goal is to introduce the subject of atmospheric entry, which is a primary focus of my work. The second goal is to provide an overview of the inductively coupled plasma torch facility used for the work presented in this manuscript. Follow on chapters will discuss specific projects.

3.1 Atmospheric entry

Atmospheric entry, as illustrated in Figure 3.1, involves the entry of a space capsule into the atmosphere of a planet at hypersonic speeds. The strong shock in front of the vehicle heats the gas to high temperatures, requiring heat shields to protect the capsule from disintegrating and burning up. In the early 1950's, engineers were unable to design a vehicle capable of withstanding the heat flux generated during reentry. Up until that time, there had been a continual push towards slender vehicles that minimized pressure drag (Swenson Jr., Grimwood et al. 1989). The eventual solution was proposed by Harry Julian Allen, an engineer at NACA – a precursor to NASA. Allen showed that the total kinetic energy converted to heat and convected to the vehicle surface scales as $C_f S/2C_D A$, where C_f and C_D are the skin friction drag coefficient per unit area and pressure drag coefficient per unit area, respectively (Allen 1958). S and A are reference areas associated with the geometry. This realization showed that slender vehicles that minimize pressure drag were ill suited for atmospheric entry. Rather, minimizing the heat flux requires the use of blunt bodies that minimize the ratio of skin friction drag to pressure drag. For this reason, missions involving atmospheric entry use blunt body geometries like that shown in Figure 3.1.

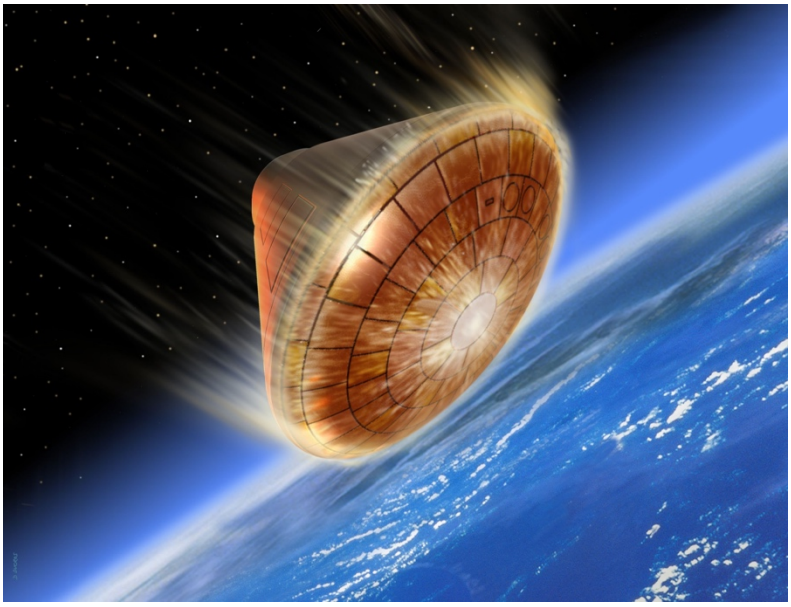

Figure 3.1 : Artist's impression of atmospheric entry (source: ESA, D. Ducros).

The heat shields (or Thermal Protection System – TPS) used to protect the reentering spacecraft are designed according to several design principals. First, they act to absorb and redistribute the heat directed towards the reentering capsule. Second, they can also radiate away from the capsule some of the thermal energy received. Third, for higher entry velocity missions, ablative heat shields are used. With ablative heat shields, the TPS degrades during entry through processes such as pyrolysis and sublimation. The lost mass redirects thermal energy away from the capsule. Ablative heat shields have seen widespread use. For example, they were used for the Apollo missions, the Mars 2020 mission, and are currently used on the SpaceX Dragon capsule.

Figure 3.2 shows some characteristic velocities and post-shock temperatures associated with Earth reentry. Vehicles returning from Earth orbit reenter at approximately 8 km/s and encounter temperatures on the order of 7 000 K. Lunar return missions, such as those of the Apollo program, involve higher entry velocities and shock temperatures on the order of 11 km/s and 12 000 K, respectively. A future Mars return mission would involve even higher reentry velocities and temperatures (around 15 km/s and 15 000 K, respectively). At such conditions, real gas effects become important. This can be seen in Figure 3.2 by comparing the two curves *calorically perfect gas* and *equilibrium chemically reacting gas*, which yield vastly different estimates of the gas temperature in the post-shock region. The difference in temperature estimates is already larger than a factor of two for a reentry velocity of 5 km/s, and the discrepancy increases sharply with velocity.

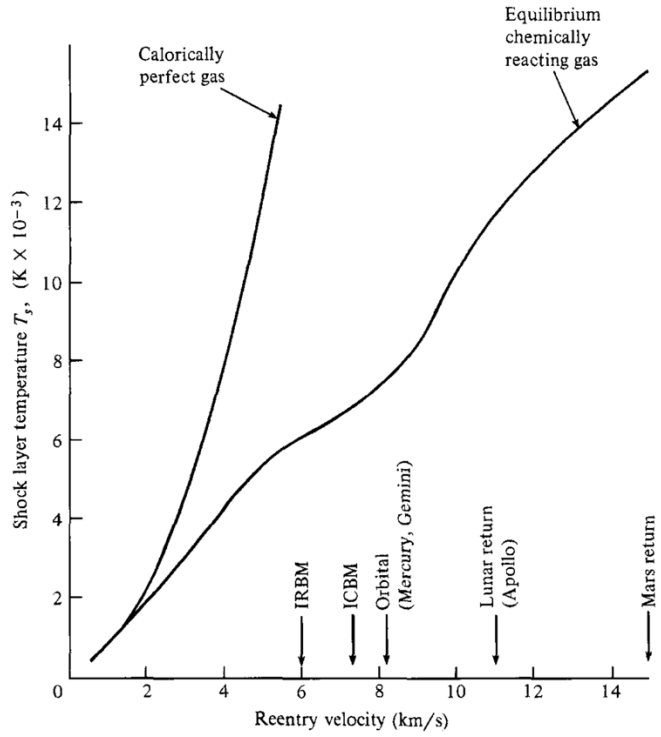

Figure 3.2 : Reentry velocities and shock layer temperatures associated with several missions. Figure taken from (Anderson Jr. 2003) and reprinted with permission.

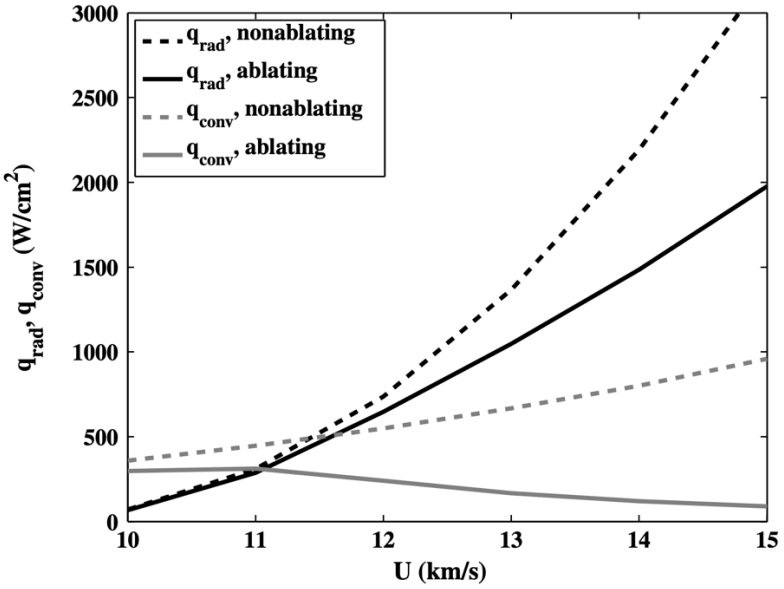

Figure 3.3 : Convective and radiative heating components plotted versus entry velocity at the stagnation point of a 1-m radius sphere, both with and without ablation. Figure taken from (Johnston, Mazaheri et al. 2013) and reprinted with permission.

The high gas temperatures generate a large heat flux to the capsule surface. This heat flux to can be broken down into two components, called the *convective* and *radiative* components. The convective component is determined by the temperature gradient at the wall as well as any exothermic/endothermic chemical reactions occurring at the wall. The radiative component is due to emission from the plasma directed towards the capsule surface. Figure 3.3 shows the relative magnitude of these two components at the stagnation point of a capsule reentering Earth's atmosphere. At lower velocities ($<$ 8 km/s), the convective heat flux dominates, and the radiative heat flux can be ignored. Above 8 km/s, the radiative heat flux quickly overtakes the convective heat flux and becomes the dominant contributor to the total heat flux. In extreme cases, the radiation can trigger additional dynamics such as *precursor radiation* and a breakdown in the *adiabatic* flow assumption. In the latter case, radiation is sufficiently strong that the flow can no longer considered to be adiabatic. In such non-adiabatic cases, the radiation dynamics are coupled to the hydrodynamics. Precursor radiation is radiation that propagates upstream of the shock and, upon being absorbed, changes the chemical composition of the pre-shocked gas (Johnston, Mazaheri et al. 2013).

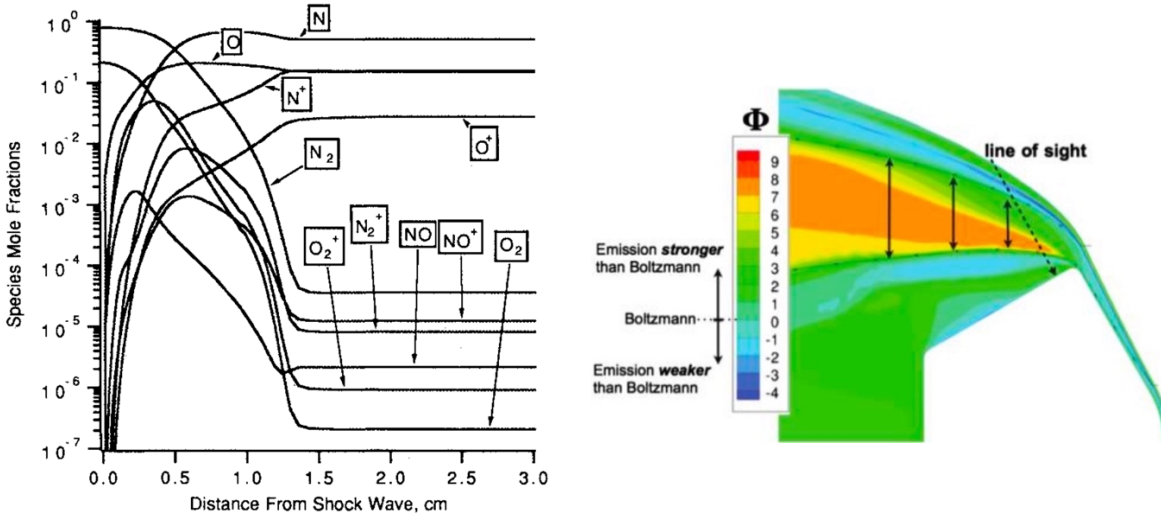

Figure 3.4 : (left) Variation in chemical composition behind a $\mathbf{12}\ \boldsymbol{km/s}$ shockwave calculated using the Park two-temperature model. Figure taken from (Park 1993) and reprinted with permission. (right) Impact of chemical equilibrium on afterbody radiation. Figure taken from (Johnston and Brandis 2014) and reprinted with permission. The orange zone highlighted is located in the vehicle afterbody and indicates a region where chemical nonequilibrium effects are important for the calculation of the radiative heat flux.

In addition to the above effects, nonequilibrium zones can also develop in the flowfield. In the post-shock region, near the stagnation point, the flow is near equilibrium due to the comparatively high pressures and low velocity of the gas. However, in other zones the flow

can leave chemical equilibrium and become a nonequilibrium flow. Two examples of this are in the zone just after the shock and in the afterbody region, or wakefield (see Figure 3.4). In these zones, the timescale of the chemistry is longer than the hydrodynamic time scales. Modeling such nonequilibrium flows is necessary to accurately predict the radiative heat flux in cases where such nonequilibrium zones contribute significantly to the heat flux. This is the case for Earth reentry at high speeds (e.g. Lunar or Mars return conditions).

As briefly summarized above, atmospheric reentry involves the following effects, which are important to varying degrees depending upon the flight conditions.

- *Real gas effects*: Variation of parameters such as the heat capacity and gas constant with temperature due to molecular dissociation and ionization of neutrals.
- *Flowfield radiation*: The high temperature flow produced by the shock radiates. At higher velocity, this radiation is the dominant contribution to the surface heat flux.
- *Nonequilibrium dynamics*: Departure from chemical equilibrium in certain zones of the flowfield.
- *Gas-surface interactions*: Chemical reactions occurring at the surface can play a strong role in the heat flux to the surface. For example, the wall *catalycity* plays an important role in the heat flux by promoting or preventing exothermic recombination reactions at the surface (Anderson Jr. 2006).

These various effects are often coupled to one another – for example, nonequilibrium dynamics can have a strong impact on the flowfield radiation. Whereas *real gas effects* are well understood and can be accounted for using up-to-date thermodynamic models (McBride, Zehe et al.), the remaining three effects are areas of active research within the atmospheric reentry community.

The research presented in Chapters 4 – 6 deals primarily with topics of relevance for *flowfield radiation* and *nonequilibrium dynamics*.

3.2 Plasma source – ICP torch

The experimental work presented in this thesis made use of an inductively coupled plasma (ICP) torch facility (Figure 3.5). The torch is a TAFA Model 66 torch powered by a 120 kVA radio frequency LEPEL Model T-50-3 power supply. The torch can couple up to 50 kW of power to the plasma. The LEPEL power supply supplies a 4 MHz radiofrequency (RF) current to the RF coil shown in Figure 3.5. The RF coil is immersed in cooling water to maintain a reasonable temperature. A quartz tube, mounted coaxially with the RF coil, separates the cooling water and RF coil from the plasma generated in the central zone. The azimuthal

current passing through the RF coil generates an axial RF magnetic field which, in turn, generates an azimuthal RF electric field. This electric field accelerates the electrons that then impart their energy to heavy particles via collisions. A portion of this energy goes into gas heating, while the remainder goes into altering the gas composition through chemical processes such as dissociation and ionization. At steady state, the production rate of electrons is balanced by loss processes such as diffusion. In this way, a steady-state plasma may be produced. This plasma is estimated to have a temperature of around 10 000 K in the central induction region where the plasma is created. The plasma then passes through an exit nozzle and directly into ambient air. The plasma temperature at the nozzle exit can be measured using Optical Emission Spectroscopy (for example, see Section 4.4.1) and is typically between 6 500 – 7 500 K depending upon the gas mixture used. At these temperatures, electrons and ions are generally present in mole fractions on the order of $10^{-5} - 10^{-3}$. The plasma is therefore a *weakly ionized, atmospheric pressure plasma*.

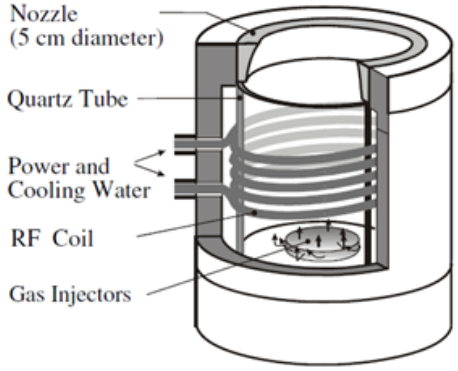

Figure 3.5 : Cutaway view of the torch head and nozzle assembly, showing the placement of the gas injectors, RF coil, quartz tube and nozzle.

Gas injectors at the base of the torch head are used to introduce the working gas, that is then heated and ionized to form the plasma. Calibrated flow meters are used to control the mass flow rate of each gas through the system. Mixtures of gases are pre-mixed before injection into the torch. Radial, swirl and axial injectors are available and used to varying degrees to produce a stable, symmetric plasma at the nozzle exit. Radial injection is the preferred method of injection as it tends to produce a temperature profile that is sharply peaked in the center. Such a profile is good for having an accurate estimate of temperature in the central zone of the jet where the temperatures are highest. This is because the measurement of temperature requires taking emission measured by the optical system – which is path integrated along the line-of-sight – and performing a transform known as *Abel inversion* that determines the spatially resolved volumetric emission. Only then can the spatially resolved temperature of the jet be determined. The uncertainty on the volumetric emission output by the Abel inversion is

largest in the center of the jet. Peaked emission profiles tend to keep the uncertainty in the central zone to a manageable level, because the measured line-of-sight emission is dominated by this central zone. For flatter emission profiles, the center contributes comparatively less to the measured emission, making the uncertainty larger. However, in many cases, pure radial injection is not possible because the plasma emission is found to be asymmetric about the central jet axis. In such cases, introducing swirl injection is found to make the plasma emission symmetric. However, swirl injection can also lead to flatter temperature profiles and/or unstable operation, both of which are disadvantageous. Therefore, the minimum required level of swirl is used. Finally, introducing a small amount of axial injection has been found to help stabilize the plasma in cases where this is necessary. A recent, detailed overview of the plasma torch used for this work can be found in (Grimaldi 2023).

The primary advantage of the ICP plasma torch at the EM2C laboratory is the fact that it provides a plasma at or close to local thermodynamic equilibrium (LTE). This makes it very easy to fully characterize the plasma jet – i.e. determine its temperature and chemical composition. The plasma is therefore perfectly adapted to cases where knowledge of these parameters is necessary. Two primary examples are as follows:

- Validation of radiative models: the intensity of a given line depends on the product of the density of the radiating state and the Einstein coefficient. Measurements of the line intensity therefore only provide information on this product. To validate a radiative model – i.e., a set of Einstein coefficients – the density of the radiating state must be known, but can easily be determined in the ICP plasma torch.
- Validating chemical kinetic models: Validating chemical kinetic models requires knowledge of an initial condition. A typical experiment might begin with shock heating a gas initially at ambient temperature. Such an experiment is well-suited to the validation of dissociation kinetics because the initial conditions – ambient gas – are well known. However, recombination kinetics are more difficult to validate. Oftentimes, recombination kinetics involve reaction mechanisms altogether different from dissociation mechanisms. For example, a molecule can be dissociated from its ground state via electron impact association: e.g. $N_2 + e^- \leftrightharpoons N + N + e^-$. While the reverse process is possible, alternate pathways not involved in the dissociation process are also possible. For example, atomic nitrogen can recombine through excited states of molecular nitrogen: e.g. $N + N + M \leftrightharpoons N_2(B) + M$, where $N_2(B)$ represents the excited B-state of molecular nitrogen. The torch is well-suited for the validation of such alternate recombination pathways because it produces a plasma in LTE – the atomic nitrogen density is known.

These advantages give the EM2C laboratory a unique capability to assist the atmospheric entry community. This has led to numerous collaborations with space agencies such as ESA, JAXA, DLR, CNES and NASA, as well as universities such as the University of Queensland in Australia.

Chapter 4 Fundamental Radiation Studies

The focus of this chapter is the experimental validation of radiative models used to calculate molecular emission in the VUV spectral region. The higher entry speeds typically associated with trajectories where the radiative heat flux is significant lead to high gas temperatures. At these conditions, the ultraviolet (UV) and vacuum ultraviolet (VUV) spectral regions play an important role, either because they emit or absorb radiation (Laux, Winter et al. 2009, Johnston, Mazaheri et al. 2013). Radiative models must therefore be tested against measurements in these spectral regions to ensure they are accurate. Whereas the ultraviolet spectral region has been extensively studied, the VUV spectral region has seen comparatively little attention due to the difficulty of making measurements. Ambient molecular oxygen in the optical path strongly absorbs any signal in this spectral region (as do other trace species such as CO_2) and thus must be completely removed. Our goal was to provide measurements of VUV emission under well-characterized conditions (known temperature and chemical composition) for the purpose of evaluating radiative model performance.

The work presented in this chapter was conducted as part of a collaboration with Brett Cruden of NASA Ames via a NASA Space Act agreement. There were two primary specific research objectives as follows:

1. Evaluate models of the CO 4^{th} positive molecular system against measurements made in the plasma torch. CO 4^{th} positive is an important contributor to the radiative heat flux for missions to Mars (Cruden, Prabhu et al. 2012).
2. Evaluate models of high temperature VUV air emission, which involves contributions from several molecular bands, against measurements made in the plasma torch. This work is relevant for atmospheric reentry into the Earth atmosphere.

These goals, the motivations behind them, and our work addressing them will be addressed in Sections 4.3 and 4.4 of this chapter. First, however, the following sections (4.1 and 4.2) will introduce the optical setup used for the measurements as well as details associated with the spectral modeling.

4.1 VUV emission measurement system

As discussed above, any VUV measurement must eliminate absorbing species from the optical path – particularly O_2 which absorbs very strongly in the VUV. To avoid this absorption, the optical system can either be put under vacuum or purged with a non-absorbing gas. The

ICP torch produces an atmospheric pressure jet that exits directly into ambient air. While a system could be designed to lower the pressure at the exit of the torch, this would not diminish the pressure sufficiently to eliminate absorption. Furthermore, the lower pressure would reduce the collision frequency and cause the plasma to deviate from local thermodynamic equilibrium. Therefore, this is not a solution that was pursued. Another option is to design an optical system that is purged or under vacuum, and that extends all the way to the boundary of the plasma jet. In this way, most ambient oxygen can be eliminated from the optical path. This was the strategy used for this work.

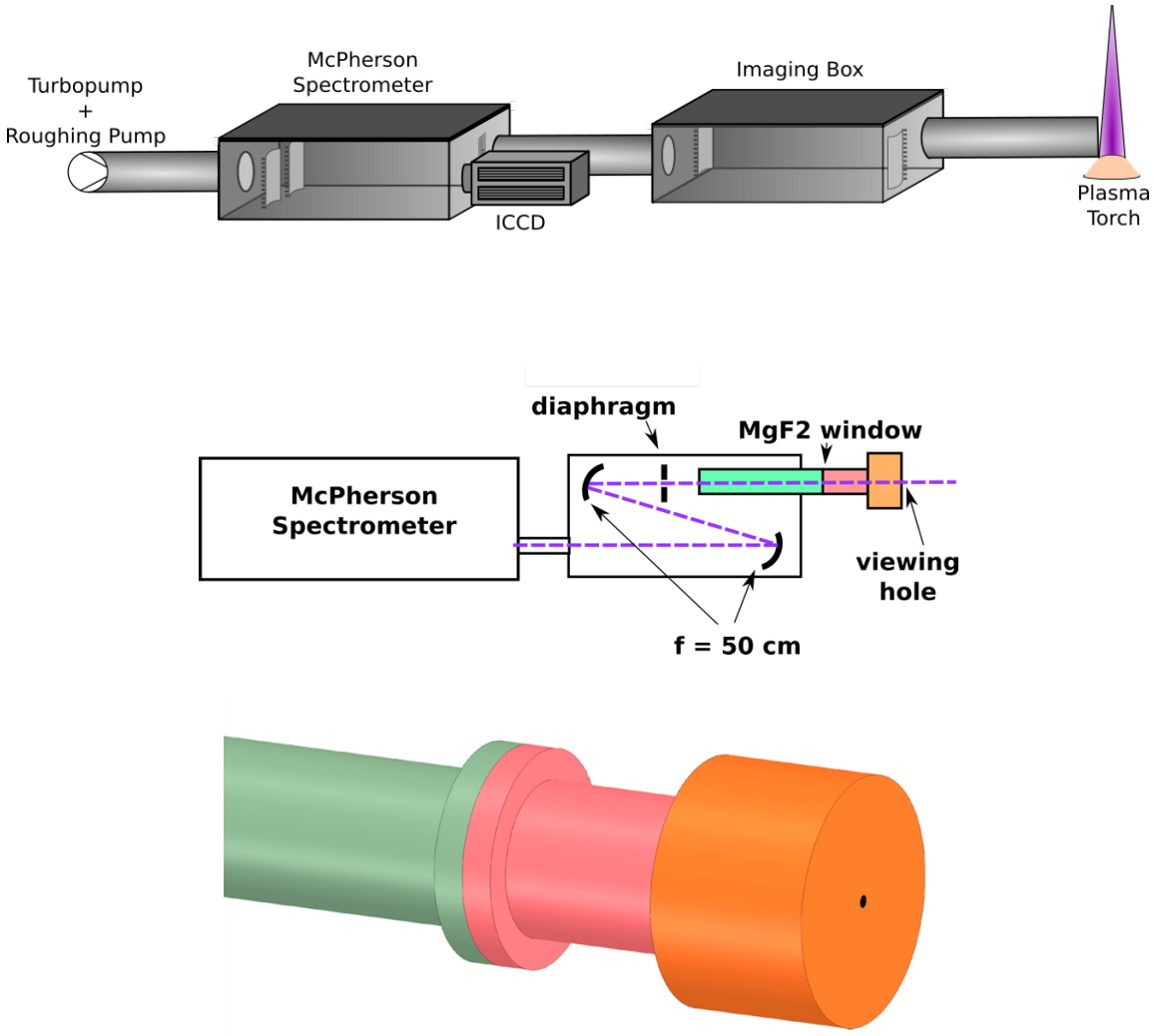

Figure 4.1: *top*) VUV spectrometer and imaging system used for making spectrally resolved VUV measurements. *middle*) Optical layout of the VUV system showing the mirrors, diaphragm, adapting tube and their relative locations with respect to the spectrometer. *bottom*) Detail of the final tube protruding from the imaging box and touching the plasma jet.

Figure 4.1 shows a diagram of the VUV system used for the measurements. This system was the final iteration of a system initially put in place by Carolyn Jacobs (Jacobs, Sheikh et al. 2013), who used a nitrogen purged setup. Measurements were obtained down to 170 nm with this initial system, but oxygen absorption was affecting the measurements below a wavelength of about 180 nm, making it somewhat difficult to compare with radiative model predictions. For this work, a McPherson vacuum spectrometer capable of making measurements down to 120 nm was used. An imaging box with two mirrors (Acton optics with a #1200 coating for 120 nm reflection) was attached to the spectrometer for imaging the spectrometer slit onto the plasma. An adapting tube protruded from this imaging box and terminated at the plasma boundary to avoid absorption by the O_2 Schumann–Runge in ambient air.

The adapting tube was designed to withstand the thermal heat flux coming from the hot plasma. It also provided electrical isolation between the spectrometer and plasma torch, which is at a potential of 10kV. A portion of this adapting tube was manufactured out of PEEK plastic (green section, Figure 4.1). This PEEK plastic section, together with the imaging box and spectrometer, was put under vacuum ($< 10^{-3}$ Torr) using a rotary vane roughing pump and a turbopump (80 l/s). The rotary vane pump was equipped with a zeolite adsorbent filter to prevent oil backstreaming into the optical system. The red section in Figure 4.1 is manufactured out of Teflon. The final piece in contact with the plasma was a water-cooled copper piece (orange section, Figure 4.1). A 2 mm hole provided optical access. The Teflon and water-cooled copper sections together made up the final 10 cm of the optical path and were placed under an argon purge. The argon purge was run at a pressure slightly above 1 atm to prevent oxygen from leaking into the system. Pressure relief ports were drilled in the Teflon piece to permit a portion of the argon to exit via these holes, rather than entirely into the plasma. The remaining portion exited through the final viewing hole, directly entering the plasma jet. Our measurements indicated that this purge did not affect the measured radiation. An MgF2 window separated the vacuum section from the argon purge section.

For calibration, an argon discharge supplied radiation traceable to NIST standards in the VUV/UV spectral regions (Klose, Bridges et al. 1988). The adapting arm linking the imaging box to the plasma was replaced with a separate adaptor for these measurements so that the argon discharge was located at the system focus. A diaphragm was used to limit the aperture of the imaging setup and to ensure that the same aperture was used for both the calibration and plasma torch measurements. Finally, due to high levels of stray light during the calibration measurement, a VUV transmission filter (eSource Optics 50150FBB) was installed for the calibration measurements. The spectrally resolved transmission of this filter was known and verified by performing calibrations both with and without the filter. For spectral regions where it was possible to compare the two calibrations, the measurements reproduced the quoted

transmission profile. This transmission filter was not used in the plasma torch measurements where stray light was not a problem.

For all emission measurements, a VUV-compatible PI-MAX2 camera from Princeton Instruments was used. The raw measurements were therefore images, with one axis corresponding to wavelength and the second axis corresponding to plasma jet radius. To produce the final spectra, the zone along the spatial axis corresponding to the center of the plasma jet was first identified. The images were then binned across this zone to produce a spectrum. The same binning was also applied to stray light measurements, which were obtained by tuning the spectrometer to 120 nm where no signal was observed. The resulting stray light signal was subtracted from all spectra. Finally, any residual background due to dark current was also subtracted. This dark current was determined by registering the signal in zones on the camera detector where no light was incident due to the spectrometer design. This same procedure was applied to obtain calibration spectra. Multiplying the emission spectra in the torch by the calibration spectra produced the final spectra, calibrated in absolute intensity. The slit function for the VUV/UV measurements is shown in Figure 4.2. The VUV system provided line-of-sight measurements along the chord intersecting the plasma centerline, 2.5-cm downstream of the nozzle exit. This can be compared with the nozzle diameter of 5-cm diameter nozzle used for all measurements.

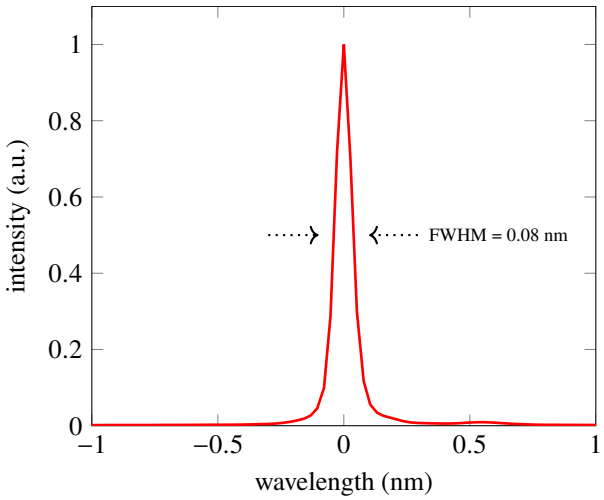

Figure 4.2: Measured slit function of the VUV system.

The intensity of the measured VUV/UV emission was a product of two measurements: the signal recorded in the torch and the calibration factor. Each of these factors has a corresponding uncertainty. δU_{calib} and δU_{signal} will denote the relative uncertainty in the calibration and the signal recorded in the torch, respectively. Assuming these two errors to be uncorrelated, the relative uncertainty in the intensity is given by $\delta U_{intensity} =$

$\sqrt{\delta U_{calib}{}^2 + \delta U_{signal}{}^2}$ (where $\delta U_i = \Delta U_i / U_i$ and ΔU_i is the absolute uncertainty in U_i). The dominant source of uncertainty comes from the calibration signal. The reported intensity curve is a smooth function. However, the measurements indicate that this intensity fluctuates slightly with wavelength. These fluctuations are less than 5% of the measured amplitude across the measured wavelength range. The only other known source of uncertainty is the camera dark current signal, but this is negligible in comparison. Therefore, the relative uncertainty in the absolute intensity of the final measurements was taken to be less than 5% across the entire wavelength range.

4.2 Modeling: SPECAIR radiation code

For a generic band system, the Einstein coefficients included in SPECAIR are calculated using the method outlined in Laux and Kruger (Laux and Kruger 1992, Laux 1993), which yields the following equation:

$$A_{\nu',\nu''} = \frac{64\pi^4 \nu^3}{3hc^3} \frac{\left(2 - \delta_{0,\Lambda'+\Lambda''}\right)}{\left(2 - \delta_{0,\Lambda'}\right)} \left(R_e^{\nu',\nu''}\right)^2 \qquad \textbf{4-1}$$

where

$$\left(R_e^{\nu',\nu''}\right)^2 = \left[\int_0^\infty \psi_{\nu'}(r)\, Re(r)\, \psi_{\nu''}(r)\, dr\right]^2 \qquad \textbf{4-2}$$

$R_e^{\nu',\nu''}$ is the electronic-vibrational transition moment; $\psi_{\nu'}$ and $\psi_{\nu''}$ represent the vibrational wavefunctions of the upper and lower states, respectively; Λ' and Λ'' are quantum numbers associated with the projection of the orbital angular momentum of the upper and lower states, respectively; and $\delta_{i,j}$ is the Kronecker delta function. The above expressions are taken from Schadee (Schadee 1978) and CGS units are used. These lead to a set of equations linking the square of the electronic-vibrational transition moment $\left(R_e^{\nu',\nu''}\right)^2$ to other conventional values as follows:

$$A_{\nu',\nu''} = \frac{64\pi^4 \nu^3}{3hc^3} \frac{\left(2 - \delta_{0,\Lambda'+\Lambda''}\right)}{\left(2 - \delta_{0,\Lambda'}\right)} \left(R_e^{\nu',\nu''}\right)^2$$

$$= (2.026 \times 10^{-6})\left(\bar{\nu}_{\nu',\nu''}\right)^3 \frac{\left(2 - \delta_{0,\Lambda'+\Lambda''}\right)}{\left(2 - \delta_{0,\Lambda'}\right)} \left(\frac{R_e^{\nu',\nu''}}{e a_0}\right)^2$$

$$
\begin{aligned}
f_{v',v''}^{abs} &= \frac{8\pi^2 m_e \nu}{3he^2} \frac{\left(2-\delta_{0,\Lambda'+\Lambda''}\right)}{\left(2-\delta_{0,\Lambda''}\right)} \left(R_e^{v',v''}\right)^2 \\
&= (3.0376 \times 10^{-6}) \bar{\nu}_{v',v''} \frac{\left(2-\delta_{0,\Lambda'+\Lambda''}\right)}{\left(2-\delta_{0,\Lambda''}\right)} \left(\frac{R_e^{v',v''}}{ea_0}\right)^2 \\
f_{v',v''}^{emis} &= \frac{\left(2-\delta_{0,\Lambda''}\right)}{\left(2-\delta_{0,\Lambda'}\right)} f_{v',v''}^{abs} \\
\sum \left(R_e^{v',v''}\right)^2 &= \left(\mathbf{2}-\boldsymbol{\delta}_{\mathbf{0},\boldsymbol{\Lambda}'+\boldsymbol{\Lambda}''}\right)(\mathbf{2}\boldsymbol{S}+\mathbf{1}) \left(\boldsymbol{R}_{\boldsymbol{e}}^{\boldsymbol{v}',\boldsymbol{v}''}\right)^{\mathbf{2}}
\end{aligned}
$$

4-3

where $\Sigma\left(R_e^{v',v''}\right)^2$ represents the sum of the electronic-vibrational transition moment across all electronic subtransitions. The above equations hold as long as the electronic-vibrational transition moment $R_e(r)$ has been calculated according to the convention of Whiting *et al* (Whiting, Schadee et al. 1980). In the above expressions, $h = 6.626 \times 10^{-27} erg \cdot s$, $c = 3.00 \times 10^{10}\ cm/s$, $e = 4.803 \times 10^{-10}\ statC$, $m_e = 9.11 \times 10^{-28}\ g$, $a_0 = 5.291 \times 10^{-9} cm$ (Bohr radius), ν is the frequency in Hz, $\bar{\nu}_{v',v''}$ is the wavenumber of the transition in cm^{-1}, and $R_e^{v',v''}$ is in atomic units (multiple of ea_0). Meanwhile, the Hönl-London factors are calculated using the method of Whiting *et al*. These are then used along with the Einstein coefficients to determine the line strength of a specific rovibrational transition. The Rydberg-Klein-Rees (RKR) method is used to determine the potentially energy curves for the relevant electronic states. The vibrational wave-functions are then calculated and used, along with the electronic-vibrational transition moment function taken from the literature, to calculate a set of Einstein coefficients for a given band system.

The following two sections deal with the CO(4+) band system and high temperature air measurements, respectively. Each section will be broken down into several subsections dealing with *i*) the temperature profile of the jet at the measurement location, *ii*) modeling of the molecular emission using the SPECAIR radiation code, and *iii*) comparisons between the modeled and measured spectra.

4.3 CO measurements

A CO_2-based mixture was injected into the torch to produce emission from the CO(4+) system. The gas heating driven by the torch dissociates the CO_2 to produce the heated CO. However,

the torch could not be operated with large quantities of CO_2 as it could not sustain the level of ionization necessary for preserving a stable plasma. Therefore, the CO_2 was heavily diluted with argon using a pre-mixing apparatus prior to injection into the torch. Argon is comparatively easy to ionize and enables stable operation of the plasma torch.

A significant effort was invested in determining suitable proportions of CO_2 and Ar, and to identify the relative proportions of radial/swirl/axial injection for introducing a stable plasma whose emission was symmetric about the jet centerline. When using air injection, smooth and axisymmetric temperature profiles are quite easily obtained and are not sensitive to the relative values of radial, swirl and axial injection. However, argon is the predominant species in the experiments reported here. For several CO_2/Ar mixtures and radial/swirl/axial injection combinations, it was found that the emission profiles obtained were asymmetric about the centerline axis. This posed a problem because a symmetric profile was necessary for the Abel inversion procedure used in the calculation of the temperature profile (*c.f.* section 4.3.1). We found that increasing the swirl had two effects. First, it helped ensure that the radial emission profile was axisymmetric. Axisymmetry was checked by comparing left/right half profiles. Second, it made the emission profile flatter near the center of the jet. This latter effect is undesirable as it leads to a large uncertainty in the Abel inversion procedure for temperature measurements. Our final choice of radial/swirl injection reflected a compromise between these two effects.

For the results presented here, $3.79\ g/s$ of Ar ($> 99.99\%$ purity) and $0.352\ g/s$ of CO_2 ($> 99.9\%$ purity) were injected into the torch. The uncertainties on these mass flow rates are both on the order of $\pm 2\%$. This combination provided a stable plasma with a relatively hot centerline temperature. The large majority of the mixture injected ($\sim 91\%$) passed via the radial and swirl injectors and was premixed. As a percentage of the total flow rate, approximately 54% was injected via the radial injector and 37% via the swirl injector. A small amount of axial injection ($\sim 10\%$) of pure argon was also used. This small amount of argon axial injection was found to enhance the plasma stability during operation. The reported value of $3.79\ g/s$ argon injected includes this axial component. Argon emission does not significantly interfere with the emission from the CO(4+) band in the plasma. It is included in the subsequent SPECAIR calculations to account for any argon lines that appear in the spectra.

4.3.1 Temperature profile

Temperature measurements were obtained from the absolute intensity of emission lines of atomic carbon (833 nm, ${}^1S - {}^1P^o$), oxygen (777 nm, ${}^5P - {}^5S^o$) and argon (764 nm, ${}^2[{}^3/_2] - {}^2[{}^3/_2]^o$). These measurements were made using a UV-VIS spectrometer (Acton SpectraPro

500i), intensified PI-MAX camera and imaging setup. A longpass filter was installed in the optical path to suppress higher order diffraction interferences. The imaging system was comprised of two parabolic mirrors and a periscope to image the spectrometer slit across the jet profile. Intensity measurements were Abel-inverted to provide spatially resolved intensity measurements. The procedure for these emission-based temperature measurements is documented in (Laux 1993, MacDonald, Jacobs et al. 2014). The analysis relies upon the assumption of thermochemical equilibrium and rotational symmetry of the plasma jet. It also assumes that the atomic emission used for the temperature analysis is optically thin.

Figure 4.3 shows the temperature measurements for the mixture studied. The difference in the nominal temperatures between the argon, carbon and oxygen lines is approximately 85 K. We therefore treat the plasma to be in equilibrium and apply the maximum uncertainty range, highlighted in Figure 4.3. This range will be used later in the SPECAIR calculations to determine maximum and minimum emission spectra. Figure 4.3 shows the chemical composition of the plasma determined with NASA CEA (McBride, Zehe et al. , McBride and Gordon 1992) and using the nominal temperature from the argon 764 nm line.

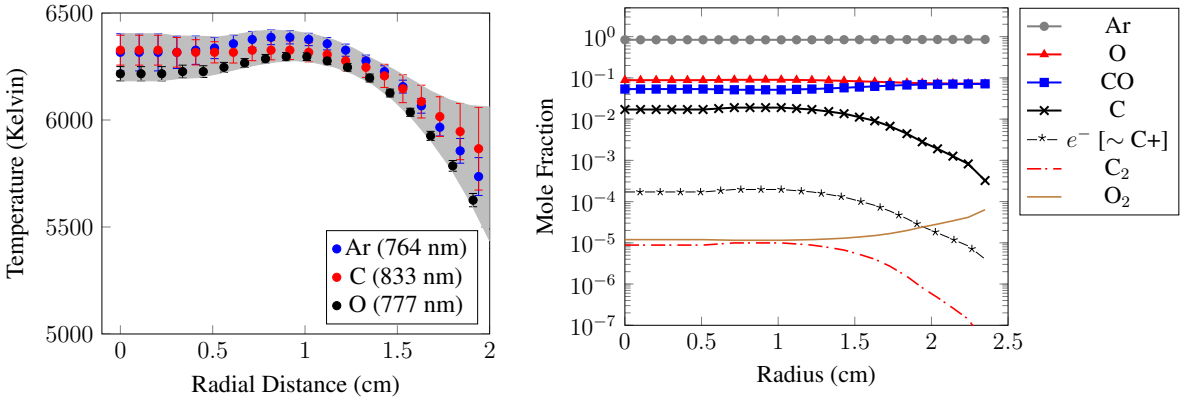

Figure 4.3: (*left*) Radial temperature profiles obtained by measuring absolute emission from several atomic features. The grey region is bounded by the maximum and minimum temperature profiles. (*right*) Radial equilibrium mole fraction profiles.

As an additional confirmation that the plasma is in thermochemical equilibrium, we measured C_2 $d\left(\,^3\Pi_g\right) - a\left(\,^3\Pi_u\right)$ (Swan system) emission using the UV/VIS spectrometer setup. A grating of 600 grooves/mm blazed at 300 nm was used and the slit function had a FWHM of approximately 0.2 nm. A long pass filter ($\lambda > 350\ nm$) was also used to suppress higher order interferences within the spectrometer. These measurements were compared with SPECAIR predictions based upon the measured temperature profiles of Figure 4.3. SPECAIR modeling of C_2 Swan radiation has been previously validated by Caillault *et al*

(Caillaut, Adreasson et al. 2006). An offset of $0.07\ mW/cm^2/nm/sr$ was added to the SPECAIR spectrum to compensate for a small continuum that is not modeled. The mole fraction of C_2 is on the order of $(0.5 - 1.0) \times 10^{-5}$ (Figure 4.3). Figure 4.4 shows a comparison between the measured and computed spectra. The good agreement is consistent with the plasma being in thermochemical equilibrium. The SPECAIR calculation is bounded by the maximum and minimum intensities possible given the uncertainties in the temperature measurements.

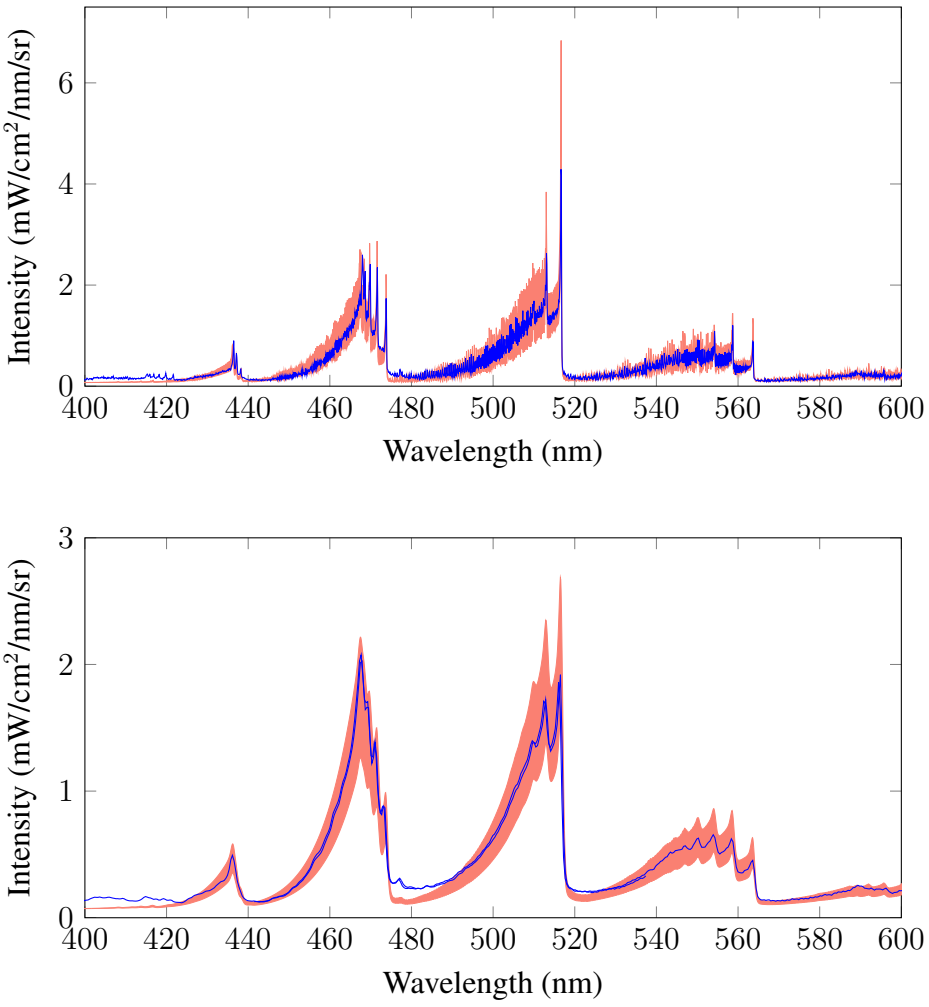

Figure 4.4: (*top*) Comparison between measured C_2 Swan emission (blue) and the SPECAIR calculation (red). (*bottom*) Measurements of the C_2 Swan bands (450–650 nm) using the VUV system in its final configuration. Two experimental measurements are included on this plot and overlap between approximately 440 and 520 nm.

To verify that the VUV system did not perturb the central portion of the plasma responsible for the measured emission, the same C_2 emission measurements were made using the VUV spectrometer. For these measurements, a low resolution grating of 180 grooves/mm was

used. These measurements were compared with SPECAIR calculations that have been shown to reproduce the unperturbed torch signal in Figure 4.4. Figure 4.4 shows the comparison with SPECAIR to be good. Again, a constant background of $0.07\ mW/cm^2/nm/sr$ was added to the SPECAIR calculation to account for continuum radiation not modeled in SPECAIR. Aside from features at 400 nm – believed to be the C_2 Deslandres-d'Azambuja system not modeled in SPECAIR – the good agreement confirms that the presence of the water-cooled copper piece and argon purge adjacent to the plasma are not perturbing the central region of the plasma responsible for the emission.

4.3.2 Modeling

4.3.2.1 Molecular Emission: $CO(4^+)$

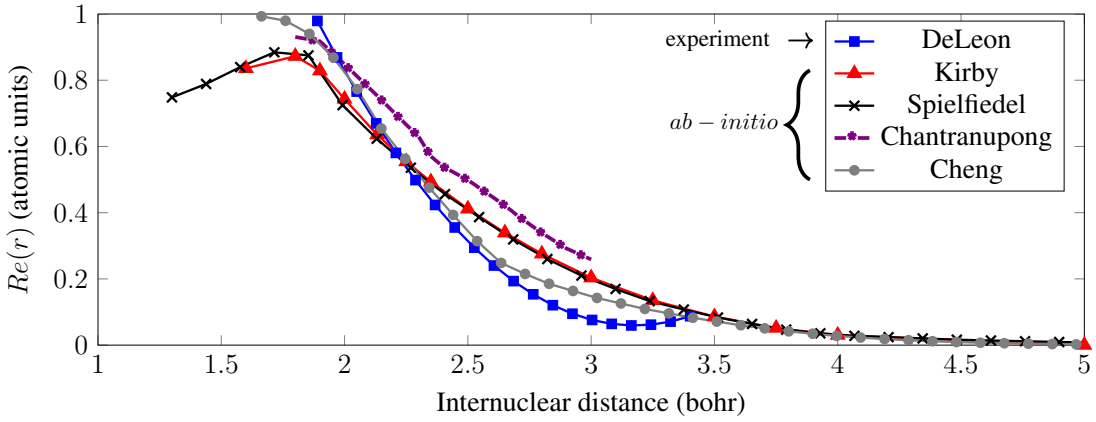

Figure 4.5: Electronic transition moment function $R_e(r)$ for the CO molecule taken from DeLeon (DeLeon 1988, DeLeon 1989), Kirby and Cooper (Kirby and Cooper 1989), Spielfiedel *et al* (Spielfiedel, Tchang-Brillet et al. 1999), Chantranupong *et al* (Chantranupong, Bhanuprakash et al. 1992) and Cheng *et al* (Cheng, Zhang et al. 2018).

For this work, five different electronic-vibrational transition moment functions were tested: DeLeon (DeLeon 1988, DeLeon 1989), Kirby and Cooper (Kirby and Cooper 1989), Spielfiedel *et al* (Spielfiedel, Tchang-Brillet et al. 1999), Chantranupong *et al* (Chantranupong, Bhanuprakash et al. 1992) and Cheng *et al* (Cheng, Zhang et al. 2018). DeLeon supplies an interpolation based on his experimental data and those previously reported by Field *et al* (Field, d'Azy et al. 1983). The ETMF of Kirby and Cooper, Chantranupong *et al*, Cheng *et al* and Spielfiedel *et al* are ab initio calculations. Figure 4.5 shows a comparison of the electronic transition moments. To comply with the convention outlined by Whiting *et al* (Whiting, Schadee et al. 1980), the data of Kirby and Cooper have been divided by a factor of $\sqrt{2}$. The ab initio calculations of Kirby and Spielfiedel are close – to within 5%. In the sections that follow, we

will therefore use the ETMF of Kirby and Cooper for the calculations and treat these ETMFs as identical.

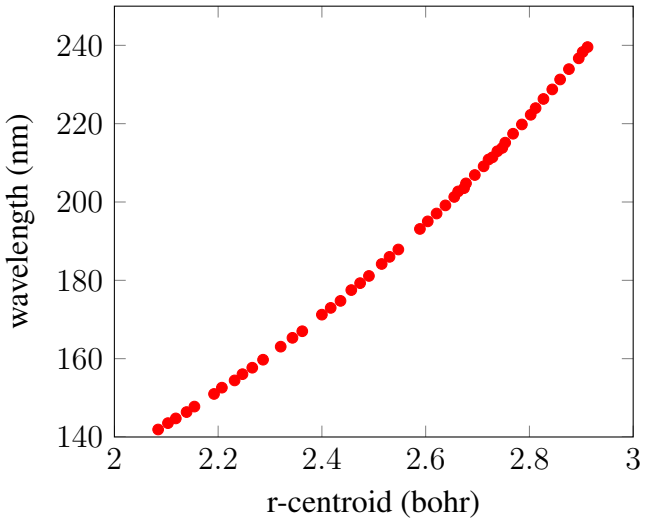

Figure 4.6: Band origin wavelength versus r-centroid for various vibrational bands of CO.

Figure 4.6 shows the band origin wavelengths associated with each r-centroid for the observed transitions. All r-centroids fall between 2 and 3 bohr. In looking at Figure 4.5, we note that this is where there is a large discrepancy between the various models for $R_e(r)$. Note that the r-centroid approximation is not used in the calculation of the Einstein coefficients. However, this approximation proves useful in visualizing where on the $R_e(r)$ curve the vibrational bands are located.

Figure 4.7 and Figure 4.8 show CO(4+) spectra calculated in the optically thin limit for a temperature of 6300 K, which corresponds approximately to the centerline temperature of the jet. Figure 4.7 identifies the bands coming from various vibrational levels of the *A* electronic state. Note that emission from $\nu = 0$ is responsible for the central portion of emission centered around 160 nm, whereas the higher vibrational levels emit mostly on the wings. Figure 4.8 identifies the main vibrational bands in the range 140–240 nm.

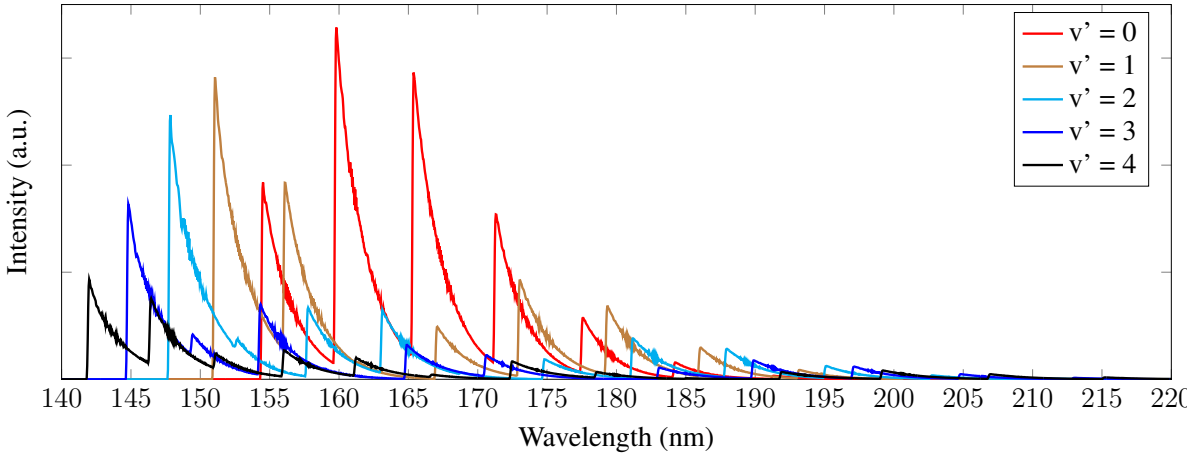

Figure 4.7: Spectra emitted by the first five vibrational levels of the electronic *A* state of CO in LTE at 6300 K, 1 atm (optically thin SPECAIR calculations).

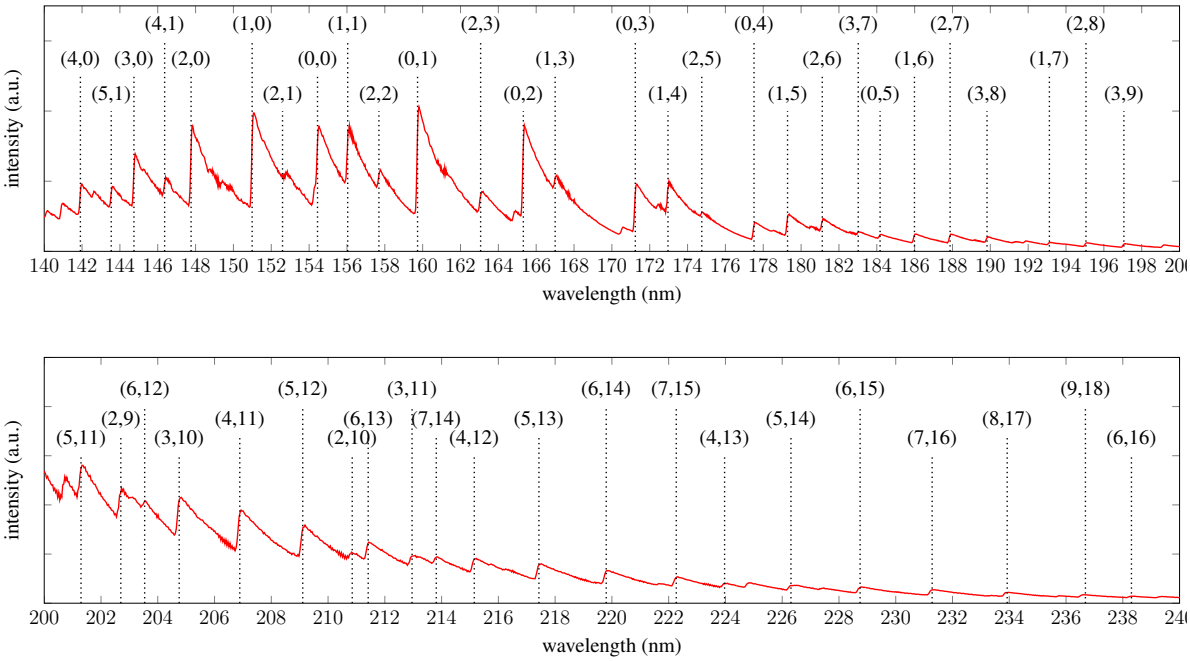

Figure 4.8: Vibrational bands (ν', ν'') of CO present in the calculated spectrum.

4.3.2.2 Atomic Emission: VUV carbon features

The majority of the atomic lines measured in the VUV/UV spectrum, as well as a portion of the CO(4^+) spectrum, are optically thick to varying degrees. To account for self-absorption along the line-of-sight, it is necessary to take into account the appropriate line broadening mechanisms. These include Doppler, Stark, resonance, van der Waals and natural line broadening. All of these are calculated in SPECAIR. The dominant mechanism is found to be

Doppler broadening, which is described by a Gaussian lineshape of full width at half maximum (FWHM) given by:

$$\Delta\lambda_{Doppler} = \lambda_{ul}\sqrt{\frac{8kT\ln 2}{mc^2}} \qquad \textbf{4-4}$$

For atoms, van der Waals broadening is also found to be important and is estimated based upon the approach detailed by Griem (Griem 1974, Griem 1997). We use the following formula, adapted from Griem (Griem 1997), for the Lorentzian FWHM of carbon lines:

$$\Delta\lambda_{vdw} = \sum_p \frac{\lambda^2}{c}\left(\sqrt{\frac{8kT}{\pi}}\right)^{3/5}\left(\frac{\hbar^5\overline{R^2}}{m_e^3}\right)^{2/5}\frac{p}{kT}\left(\frac{X_p}{E_p^{4/5}m_{rp}^{3/10}}\right) \qquad \textbf{4-5}$$

where all values are in SI units. m_e is the mass of the electron, X_p the mole fraction of the perturber, E_p the energy of the excited state of the perturber connected to its ground state by an allowed transition, and m_{rp} the reduced mass of the radiator and the perturber. The formula for the parameter R is taken from Griem:

$$\overline{R^2} = \frac{1}{2}\frac{E_H}{E_\infty - E_i}\left[5\frac{E_H}{E_\infty - E_i} + 1 - 3l_i(l_i+1)\right] \qquad \textbf{4-6}$$

where E_H is the ionization energy of the hydrogen atom, E_∞ is the ionization energy of the radiating atom, and E_i is the excited state energy of the radiator. l_i is the orbital angular momentum quantum number of the radiating state. The FWHM calculated by Eqn. 5 was increased by a multiplicative factor of $n_e^{2/5}$, where n_e is the number of valence electrons of the perturber. This is done based upon a remark by Griem in section 4.8 of his text (Griem 1997).

Table 4-1 shows the parameters used in Eqn. 6 for the van der Waals calculation. Argon is the perturber present in the highest quantities (X_p~0.84) and, for this perturber, values of $E_p = 11.6\,eV$, $m_{rp} = 9.2\,amu$, and $n_e = 6$ were used. Table 4-2 shows the Doppler and van der Waals FWHMs calculated with the above equations for conditions at the center of the plasma jet ($T = 6300\,K, p = 1\,atm$). These are used for the SPECAIR calculation of the carbon lines at 193 nm and 248 nm.

Table 4-1: Parameters used in Eqn. 6 for the line broadening calculation for the 193 nm ($^1P^o - {}^1D$) and 248 nm ($^1P^o - {}^1S$) carbon lines.

$E_H\,(eV)$	$E_\infty\,(eV)$	$E_i\,(eV)$	l_i
13.6	11.3	7.68	0

Table 4-2: Dominant broadening linewidths for two of the atomic carbon lines in the VUV.

	Doppler (FWHM, pm)	Van der Waals (FWHM, pm)
C I (193 nm)	3.17	0.38
C I (248 nm)	4.07	0.63

4.3.3 Results and Discussion

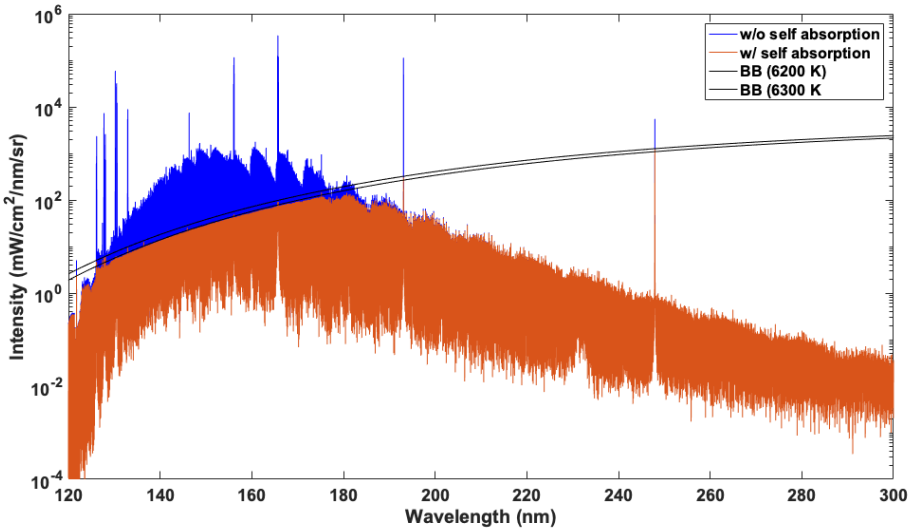

Figure 4.9: SPECAIR calculation with and without self-absorption to illustrate the optically thick nature of the emission in the VUV. The Kirby electronic transition moment function was used for the calculation of the CO(4+) bands. This calculation was done without a slit function.

Figure 4.9 shows a SPECAIR calculation of the CO_2/Ar plasma emission at the exit of the torch with and without self-absorption. The calculation was done by assuming thermochemical equilibrium and by solving the radiative transport equation across the profile defined by the measured temperatures reported in Figure 4.3. It is worth noting that the CO(4+) emission becomes heavily optically thick in the VUV below 180 nm. All carbon lines, including the one at 248 nm, are also heavily optically thick. The optically thin and optically thick calculations presented in Figure 4.9 differ by several orders of magnitude for the lines below 200 nm, indicating the extent of optical thickness. Figure 4.10 shows a zoom on the calculated 193 nm carbon line to illustrate the severe impact of self-absorption on the line profile. Figure 4.11 shows the comparison between the measured spectrum and SPECAIR calculations based upon the ETMFs from Kirby (Kirby and Cooper 1989), Chantranupong (Chantranupong, Bhanuprakash et al. 1992), Cheng (Cheng, Zhang et al. 2018), and DeLeon (DeLeon 1988,

DeLeon 1989). Note that the $C_2\ D\ ^1\Sigma_u^+ - X\ ^1\Sigma_g^+$ (Mulliken system) is included in SPECAIR calculations and appears at 230 nm. We used the model of Bruna and Wright for this molecular system (Bruna and Wright 1992). For these plots, the uncertainty in the temperature measurements is carried through the SPECAIR calculation. The bounds on the SPECAIR calculation correspond to the minimum and maximum possible temperature based upon the measured temperature profile shown in Figure 4.3. The Kirby ETMF agrees within the error bars from between 162 – 210 nm. Chantranupong is on the lower end of the error from 162 – 175 nm, outside the range from 175 – 218nm, and in agreement above 218 nm. Cheng agrees well from 162 – 180 nm, and is too high at longer wavelengths. DeLeon is in agreement only from 162 – 170nm, and too high everywhere else. These differences stem from the corresponding differences in the ETMF's shown in Figure 4.5 for radii between 2 and 3 bohr. Concerning the Kirby ETMF calculations, the discrepancy with the experimental measurements below 162 nm can be accounted for by cold gas absorption in the shear layer. This is discussed below. Sources of radiation that could cause the discrepancy above 210 nm were checked, including O_2 Schumann-Runge from entrained oxygen and carbon bound-free emission, though neither were strong enough to account for the difference. Thus, the discrepancy above 210 nm may indicate that Kirby's ETMF should be reevaluated at larger separation distances (see Figure 4.6) that impact this region of the spectrum.

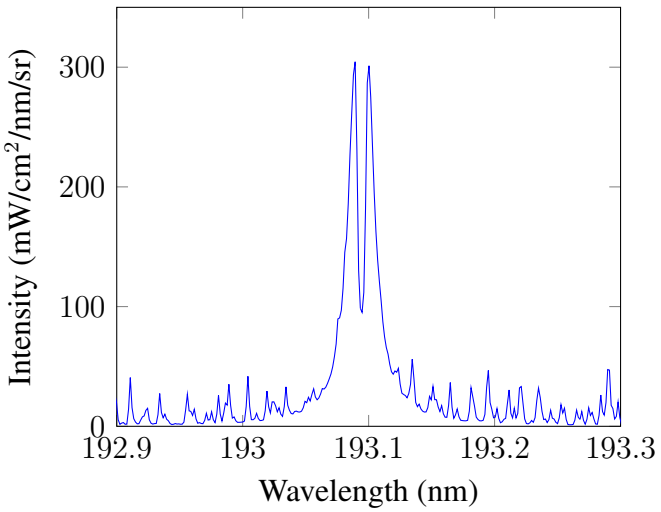

Figure 4.10: Zoom on the calculated 193 nm C line structure from the calculation in Figure 4.9. The slit FWHM of 0.08 nm is wider than the observed feature and, consequently, this "doublet-like" structure cannot be observed in the measured spectrum.

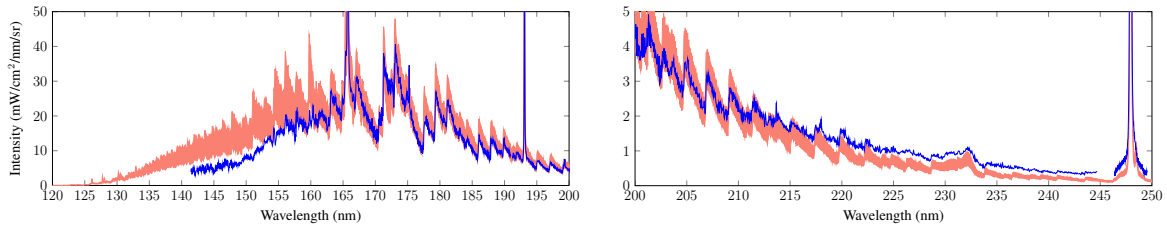

(a) Experiment (blue) and SPECAIR calculations (red) based upon the Kirby electronic transition moment function.

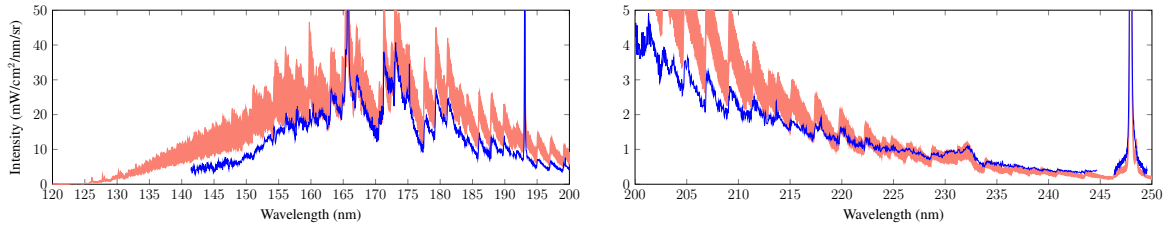

(b) Experiment (blue) and SPECAIR calculations (red) based upon the Chantranupong electronic transition moment function.

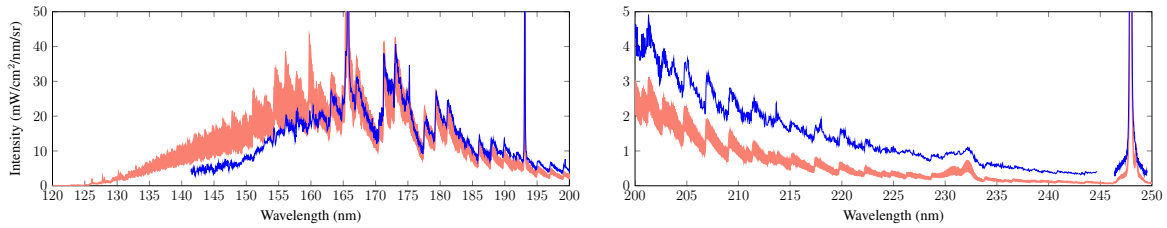

(c) Experiment (blue) and SPECAIR calculations (red) based upon the Cheng electronic transition moment function.

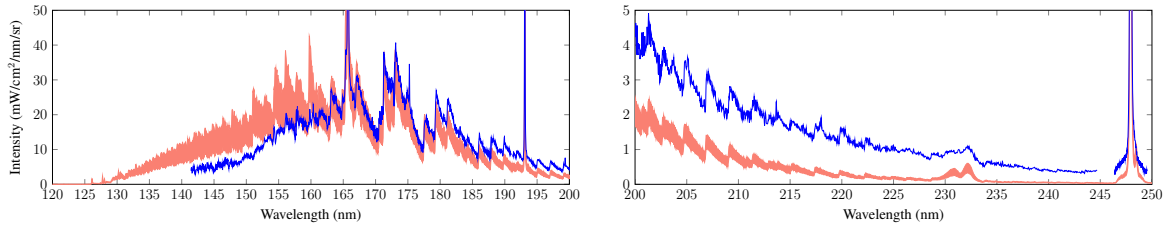

(d) Experiment (blue) and SPECAIR calculations (red) based upon the DeLeon *et al* electronic transition moment function.

Figure 4.11

None of the curves reproduce the spectra accurately below approximately 165 nm. This is attributed to absorption from cold gases in the VUV. CO_2 is present in the shear layer of the jet, where temperatures are cold enough that it remains undissociated. To evaluate the potential impact of CO_2 on the spectra, the cross-sections for cold CO_2 absorption from

Thompson, Harteck and Reeves (Thompson, Harteck et al. 1963) were used. This dataset includes data from Watanabe, Zelikoff and Inn (Watanabe and Inn 1953). Given the injection mixture used for these measurements a CO_2 mole fraction of $x_{CO2} = 0.078$ is calculated at room temperature. Adding about 0.5 cm of cold gas absorption to the measurement reproduces nicely the experimental data (see Figure 4.12). This would be consistent with local cooling of the gas mixture near the water-cooled copper piece. Another possible species for absorption of the signal would be O_2 due to air entrainment around the boundaries of the jet. Adding about 50 μm of cold O_2 absorption also produces the level of absorption needed to match the profile produced by CO_2 absorption. Note that this equivalent path length of O_2 would not be consistent oxygen levels associated with the level of vacuum in the system or the purity of the argon purge. Rather, it would have to come from cold air entrainment into the edges of the jet. The absorption profiles of O_2 and CO_2 are quite similar in shape over the wavelength range 145 – 160 nm and thus produce a similar result using either molecule as the absorber. Therefore, while CO_2 is a likely absorber given that it is known to be present, it is possible that some amount of O_2 is also contributing to the reduced signal at low wavelengths. Based upon the comparison with SPECAIR predictions, the measurements appear to be free from cold gas absorption down to about 165 nm. Table 4-3 shows how the integral of the measured spectrum, from 165 – 220 nm, compares with the model predictions.

Atomic carbon has several lines that emit in the VUV and UV. Figure 4.13 shows zooms on the 193 nm ($^1P^o - {}^1D$) and 248 nm ($^1P^o - {}^1S$) carbon lines that were not visible in the previous figures. The calculation for the underlying CO bands was done with the Kirby ETMF. The Einstein coefficients for these carbon lines were taken from the NIST atomic spectral database (Kramida, Ralchenko et al. 2018) which, in turn, cites Fischer (Fischer 2006) as the source for these coefficients. As discussed earlier, Doppler broadening is the dominant line broadening mechanism. However, for these atomic lines of carbon, van der Waals broadening also plays an important role. The Einstein coefficient accuracy for the 193 nm line is quoted to be within 3%. The Einstein coefficient accuracy for the 248 nm line is quoted to be 18%. Both lines appear to be well captured.

Table 4-3: Integrals of the measured/theoretical spectra between 165 and 220 nm in mW/cm^2/sr. The theoretical spectra used for the calculation correspond to those in Figure 4.12 and include CO_2 absorption. However, the impact of this absorption is minimal given the wavelength bounds of the integral. The uncertainty bounds on the SPECAIR calculations correspond to the minimum and maximum values based upon the uncertainty in the temperature measurement. The uncertainty for the experimental value is estimated to be primarily from the reported uncertainty of the calibration source – ±5% according to (Klose, Bridges et al. 1988). The total uncertainty for the experimental value is estimated at ±6% or ± 36 mW/cm^2/sr.

Experiment = 606	
Chantranupong	819 ± 153
Cheng	502 ± 94
DeLeon	447 ± 83
Kirby	632 ± 117

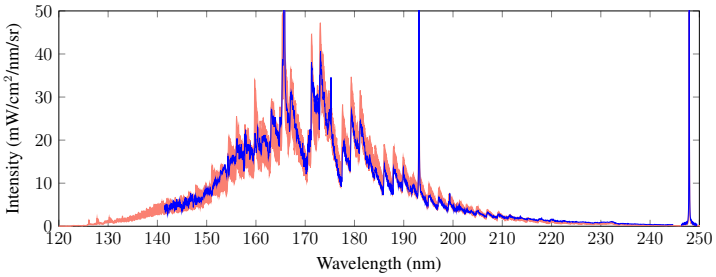

(a) Experiment (blue) and SPECAIR calculations (red) using Kirby electronic transition moment function with a 0.5 cm absorption path length of cold CO_2 ($x_{CO2} = 0.078$).

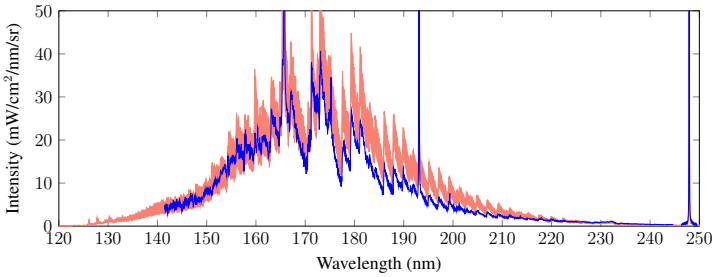

(b) Experiment (blue) and SPECAIR calculations (red) using Chantranupong electronic transition moment function with a 0.5 cm absorption path length of cold CO_2 ($x_{CO2} = 0.078$).

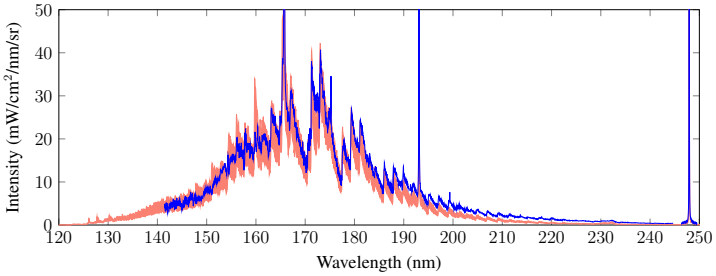

(c) Experiment (blue) and SPECAIR calculations (red) using Cheng electronic transition moment function with a 0.5 cm absorption path length of cold CO_2 ($x_{CO2} = 0.078$).

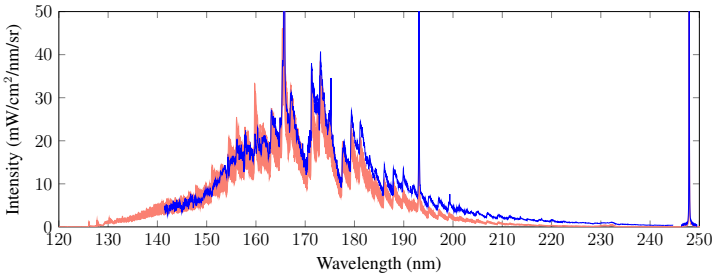

(a) Experiment (blue) and SPECAIR calculations (red) using DeLeon electronic transition moment function with a 0.5 cm absorption path length of cold CO_2 ($x_{CO2} = 0.078$).

Figure 4.12

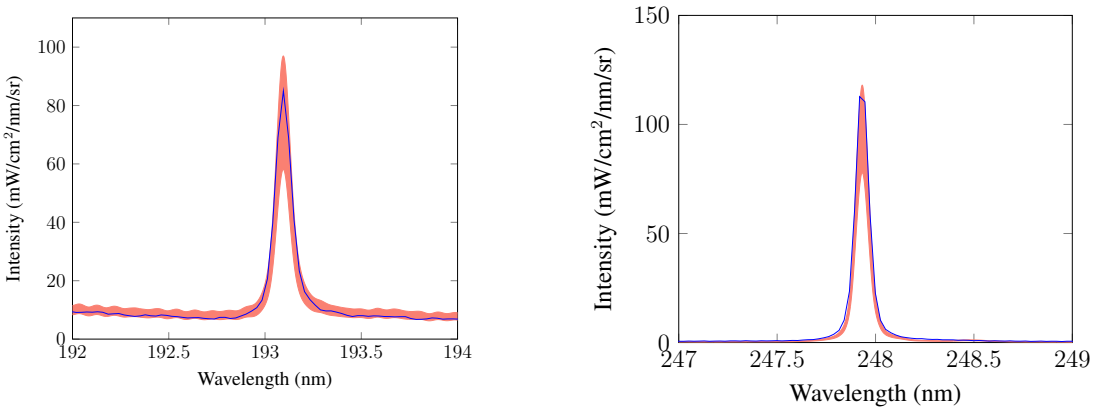

Figure 4.13: (left) Zoom on the 193 nm C feature (left) and 248 nm C feature (right). Experiment is blue and SPECAIR calculation is in red. For reference, the SPECAIR calculation shown here used the Kirby ETMF for the underlying CO(4+) emission.

4.4 NO measurements

When air is heated to high temperatures (4000 – 8000 K), nitric oxide (NO) begins to form in small quantities ($< 5\%$ by volume). Though NO is only present in small quantities, it is one of the dominant radiators in the VUV/UV for temperatures between 4 000 K than 8 000 K. Therefore, correctly predicting air emission across this temperature range requires a validated model for NO emission. This was the goal of the work presented in this section. Measurements of high temperature air emission were first obtained under well-characterized conditions. These measurements were then compared with predictions from the radiative code SPECAIR to assess. As will be discussed, the comparison between the SPECAIR calculation and measurements led to several modifications in the SPECAIR code to improve agreement.

4.4.1 Temperature profile

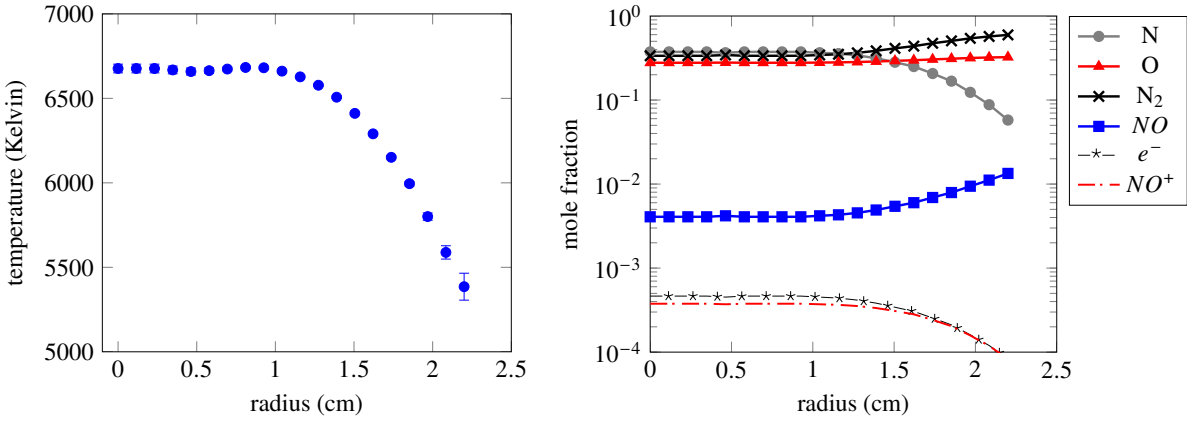

Figure 4.14: (*left*) Temperature profile obtained by measuring the 777 nm oxygen triplet emission. (*right*) Composition of the plasma jet as a function of radius based upon the measured temperature profile.

The temperature profile of the plasma jet was obtained by measuring the absolute emission from the oxygen triplet at 777 nm ($^5P - {}^5S^o$). The setup used for the temperature measurements with the CO_2/Ar mixture was also used here. Once again, intensity measurements are Abel-inverted to provide spatially resolved intensity profiles and the analysis relies upon the assumption of thermochemical equilibrium. While for the CO_2/Ar mixture, additional measurements were performed to confirm this latter assumption, the air mixture has been extensively studied and has been shown to be in equilibrium (Laux 1993, Laux, Spence et al. 2003). Figure 4.14 shows the temperature profile for the conditions studied here. The error bars are small, indicating that the temperature is accurately known. Given this temperature profile, the composition of the air plasma may be calculated using NASA CEA

(McBride, Zehe et al. , McBride and Gordon 1992) and is shown in Figure 4.14. Ar, CO, and C are present in mole fractions on the order of 6×10^{-3}, 2×10^{-4}, and 6×10^{-5}, respectively.

4.4.2 Modeling

The initial SPECAIR model for the nitric oxide bands was developed in (Laux 1993), (Laux and Kruger 1992), and (Laux, Gessman et al. 1993) to include important transitions in the VUV such as the delta and epsilon systems that had not been previously considered in high-temperature air radiation models. The model was then updated in (Laux, Spence et al. 2003) to account for line position perturbations in transitions involving the $^2\Pi$ states. This SPECAIR model was found to give very good agreement with measurements for wavelengths above 200 nm. The code was modified for this work to improve agreement at lower wavelengths. The next two subsections discuss the modeling of molecular and atomic emission, respectively. For each molecular system or atomic feature, the original SPECAIR model is presented, followed by any updates that were incorporated into the model as a result of this work.

4.4.2.1 Molecular Emission: Nitric Oxide Bands

The approach outlined in Section 4.2 was used for the γ, ϵ, and β' systems of NO. Table 4-4 shows the sources used for these calculations. This methodology does not take into account perturbations between quantum states. The wave functions of states perturbed by avoided crossings assume a hybrid form, characterized by a mixture of the quantum states involved in the perturbation. This is the case for emission from excited $^2\Pi$ states of NO and the methodology for these systems will be detailed below.

Table 4-4: Sources for the parameters used in the RKR portion of the NO molecular emission calculations from the A, D, and B' upper states to the X ground state.

State	Molecular constants	Dissociation energy, cm^{-1}
$X\ ^2\Pi_r$	(Amiot 1982)	(Lavrov 1991)
$A\ ^2\Sigma^+$	(Huber and Herzberg 1979)	(Lavrov 1991)
$D\ ^2\Sigma^+$	(Huber and Herzberg 1979)	(Lavrov 1991)
$B'\ ^2\Delta$	(Huber and Herzberg 1979)	(Lavrov 1991)

Emission from NO $^2\Sigma^+$ states : The $\gamma\left(A\ ^2\Sigma^+ - X\ ^2\Pi\right)$ and $\epsilon\left(D\ ^2\Sigma^+ - X\ ^2\Pi\right)$ systems are modeled using the approach outlined above; no perturbations were taken into account. The ETMF of Langhoff, Bauschlicher, and Partridge was used for the NO γ system emission (Langhoff, Bauschlicher et al. 1988). The ETMF for the NO ϵ system was also taken from

calculations done by Langhoff and coworkers (Sheehy, Bauschlicher et al. 1994). Emission from vibrational levels up to $v = 8$ in the A state and $v = 5$ in the D state are accounted for.

In this paper, the maximum vibrational level of the D state was increased from $v = 5$ to $v = 6$. Figure 4.15a shows the effect of this modification on the SPECAIR calculation, which is minor and limited to wavelengths below 175 nm. The curve labeled “additional D states” is the same as the original calculation but with the maximum vibrational level of the D state increased from $v = 5$ to $v = 6$.

The NO $\gamma'\left(E\ ^2\Sigma^+ - X\ ^2\Pi\right)$ system is included in SPECAIR as discussed in(Laux 1993). The electronic transition dipole moment used was that of De Vivie and Peyerimhoff(de Vivie and Peyerimhoff 1988). The spectroscopic constants for the $E\ ^2\Sigma^+$ state were taken from Huber and Herzberg (Huber and Herzberg 1979). The resulting calculations largely overpredict the measured photoabsorption cross sections reported by Chang et al. (Chang, Cooper et al. 1993) discussed in section 4.4.3. Furthermore, the impact of this system on the high-temperature air emission spectrum was minimal. For these reasons, this system is not included in the SPECAIR calculations shown below.

Emission from NO $^2\Delta$ states : Emission from the $\beta'\left(B'\ ^2\Delta - X\ ^2\Pi\right)$ was modeled using the standard approach and no perturbations were taken into account. The β' system primarily affects the spectrum at wavelengths below approximately 180 nm, and even then only weakly with an average magnitude less than $1\ mW/cm^2/nm/sr$. The ETMF for this band was taken from de Vivie and Peyerimhoff (de Vivie and Peyerimhoff 1988). Emission from vibrational levels up to $v = 7$ in the B' state are accounted for.

For this work, the maximum vibrational level of the B' state was D increased from $v = 7$ to $v = 9$. Figure 4.15b shows the effect of this modification on the SPECAIR calculation, which is negligible and limited to wavelengths below 160 nm. The curve labeled “additional B' states” is the same as the curve labeled “additional D states” but with the maximum vibrational level of the B' state increased from $v = 7$ to $v = 9$.

The NO $F\ ^2\Delta - X\ ^2\Pi$ system was also added to SPECAIR. As with the γ' system of NO, the resulting calculations largely overpredict the measured photoabsorption cross sections reported by Chang *et al* (Chang, Cooper et al. 1993). The corresponding impact on the high-temperature air emission spectrum is also minimal. For these reasons, this system is not included in the SPECAIR calculations shown below.

Emission from NO $^2\Pi$ states : Perturbations among the various $^2\Pi$ states of NO have been noted in the literature (Gallusser and Dressler 1982, Qu, Cooper et al. 2021). These

perturbations affect both the line strength and position of individual lines within these systems. This paper uses the notation of Gallusser and Dressler and SPECAIR accounts for emission from the $B\ ^2\Pi - X\ ^2\Pi$, $C\ ^2\Pi - X\ ^2\Pi$, $L\ ^2\Pi - X\ ^2\Pi$, $K\ ^2\Pi - X\ ^2\Pi$, and $Q\ ^2\Pi - X\ ^2\Pi$ systems. The primary $^2\Pi - \ ^2\Pi$ transitions of NO contributing to the observed emission in the UV/VUV are the B−X and C−X systems, also known as the β and δ systems. These $^2\Pi - \ ^2\Pi$ transitions require a special treatment because of the strong perturbations among the various $^2\Pi$ states of NO. The perturbations affect both the line positions and the line strengths. The original SPECAIR calculates the perturbed energies and line positions using the perturbation method outlined by Gallusser and Dressler. However, perturbations in the line strengths were not taken into account.♦ In this paper, SPECAIR was modified as follows:

1. The maximum emitting vibrational level for the $C^2\Pi$ state was increased from $v_{max} = 4 \rightarrow 9$. This impacts emission from the NO δ system.
2. Emission from the $L\ ^2\Pi - X\ ^2\Pi$, $K\ ^2\Pi - X\ ^2\Pi$, and $Q\ ^2\Pi - X\ ^2\Pi$ systems was accounted for.
3. The effect of perturbations on the oscillator strength was accounted for the $B\ ^2\Pi - X\ ^2\Pi$, $C\ ^2\Pi - X\ ^2\Pi$, $L\ ^2\Pi - X\ ^2\Pi$, $K\ ^2\Pi - X\ ^2\Pi$, and $Q\ ^2\Pi - X\ ^2\Pi$ systems.

Note that the $^2\Pi$ states have a multiplicity of two. Each branch of the multiplet is impacted separately by the perturbation calculation of Gallusser and Dressler. The calculations in SPECAIR fully account for this separate dependence on the perturbed energy. However, as a first approximation, this separate dependence on the line strength is ignored. Rather, the oscillator strength for each branch of the multiplet is taken to be the average of the two branches. As a check on this assumption, we replaced the oscillator strength by the maximum or minimum of the two branches (rather than the average) to see what changes this resulted in and found the difference to be minimal.

As a result of these modifications, the SPECAIR calculations in this paper account for emission from vibrational levels up to $v = 9$ in the δ system, $v = 25$ in the β system, $v = 11$ in the L−X ystem, $v = 3$ in the Q−X system, and $v = 4$ in the K−X system. Additionally, the effect of perturbations on the energy levels and on the oscillator strengths is accounted for. Figure 4.15c and Figure 4.15d show the effect of this modification on the SPECAIR calculation. In Figure 4.15c, the perturbation on the energy levels and oscillator strengths is accounted for. In addition, the NO L−X, K−X, and Q−X systems are added. However, the maximum

♦ For a few vibrational levels, the perturbed line positions computed with the Gallusser and Dressler method were then replaced by the more accurate experimental line positions of Amiot and Verges for the $v = 1$ level of the C state (Amiot, C. and J. Verges (1982)).

vibrational quantum number of the C state is limited to $v = 4$ as done in the original SPECAIR calculation, even though the perturbation calculations permit calculations up to $v = 9$. The curve labeled "w/perturbations" is the same as the curve labeled "additional B' states" but with the perturbation calculation for the oscillator strengths of the $^2\Pi$ states accounted for. In Figure 4.15d, the curve labeled "additional C states" is the same as the curve labeled "w/perturbations" but with the maximum vibrational level of the NO C state increased from $v = 4$ to $v = 9$. In comparing Figure 4.15c and Figure 4.15d, it is apparent that increasing the maximum vibrational quantum number of the C state from $v = 4$ to $v = 9$ has a very minimal impact. However, the impact of the perturbations on the oscillator strengths has a substantial impact.

Emission from NO^+ (A-X) and N_2 (a-X) states : Two new electronic systems were added to SPECAIR: the $NO^+\ A\ ^1\Pi - X\ ^1\Sigma^+$ and $N_2\ a\ ^1\Pi_g\ - X\ ^1\Sigma^+$ (Lyman–Birge–Hopfield) transitions. For the $NO^+\ A\ ^1\Pi - X\ ^1\Sigma^+$ system, the electronic transition dipole moment function of Partridge *et al* (Partridge, Langhoff et al. 1990) was used (see Fig. 7 and Table 2 of their article). For the Lyman–Birge–Hopfield system of N_2, the magnetic dipole transition was modeled using the oscillator strengths reported by Pilling *et al* (Pilling, Bass et al. 1971). Figure 4.15e shows that the addition of these two systems has a negligible impact on the predicted emission. The curve labeled "with N_2 a − X and NO^+ A − X" is the same as the curve labeled "additional C states" but with the N_2 a − X and NO^+ A − X systems added.

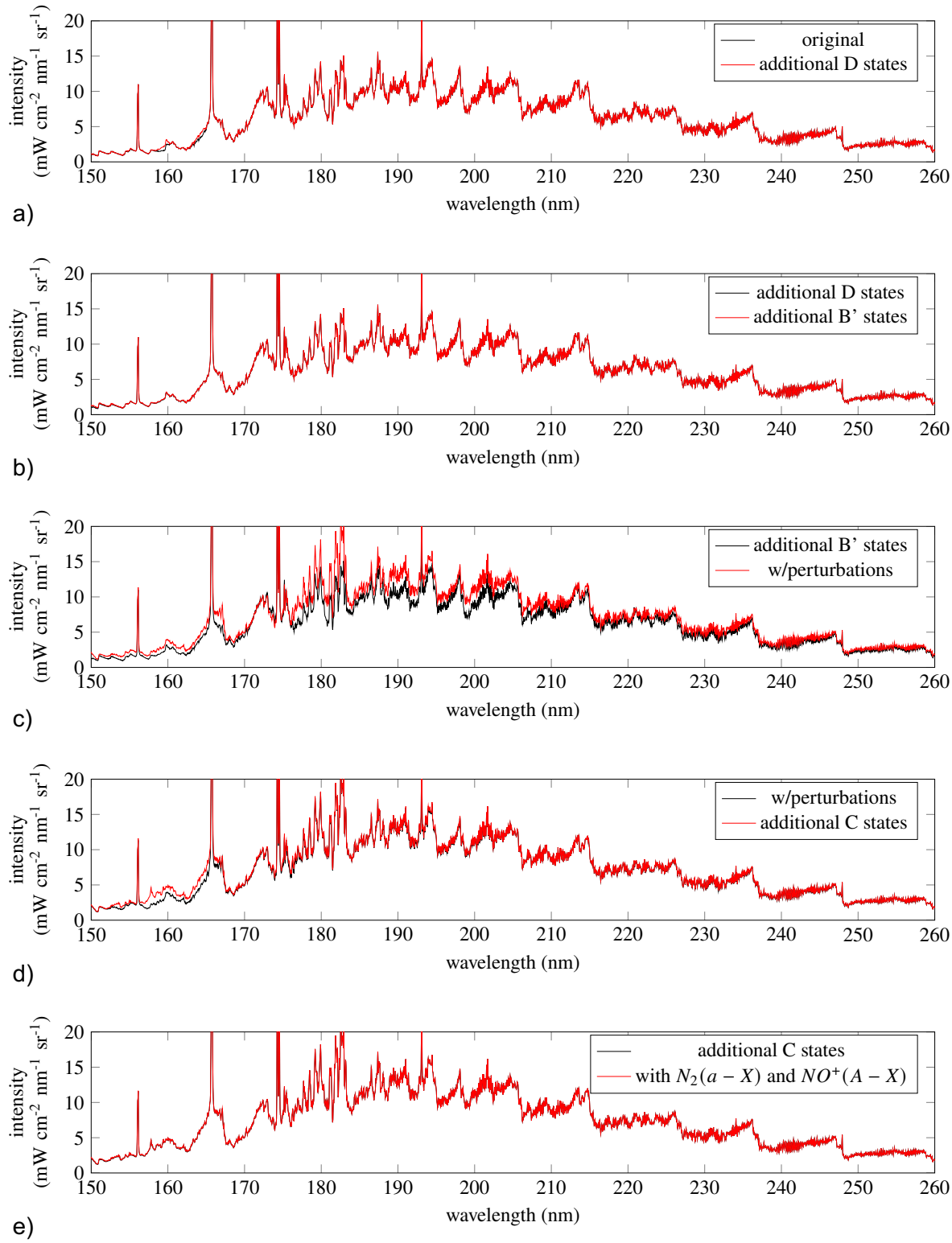

Figure 4.15: Evolution in the SPECAIR calculation after several modifications, as described in the text.

Relative contribution from various systems : Figure 4.16 shows the contributions from various NO bands discussed above as well as other residual sources of the predicted emission calculated based on the temperature profile shown in Figure 4.14. The calculations in Figure 4.16 were performed after updating SPECAIR as described in this section. In Figure 4.16f, the curve labeled CO(4+) contains emission from the CO 4+ system, while the curve labeled "minor systems" contains the combined emission from $N_2\ a\ ^1\Pi_g\ - X\ ^1\Sigma^+$, $NO^+\ A\ ^1\Pi - X\ ^1\Sigma^+$, $NO\ L\ ^2\Pi - X\ ^2\Pi$, $NO\ K\ ^2\Pi - X\ ^2\Pi$, and $NO\ Q\ ^2\Pi - X\ ^2\Pi$ systems.

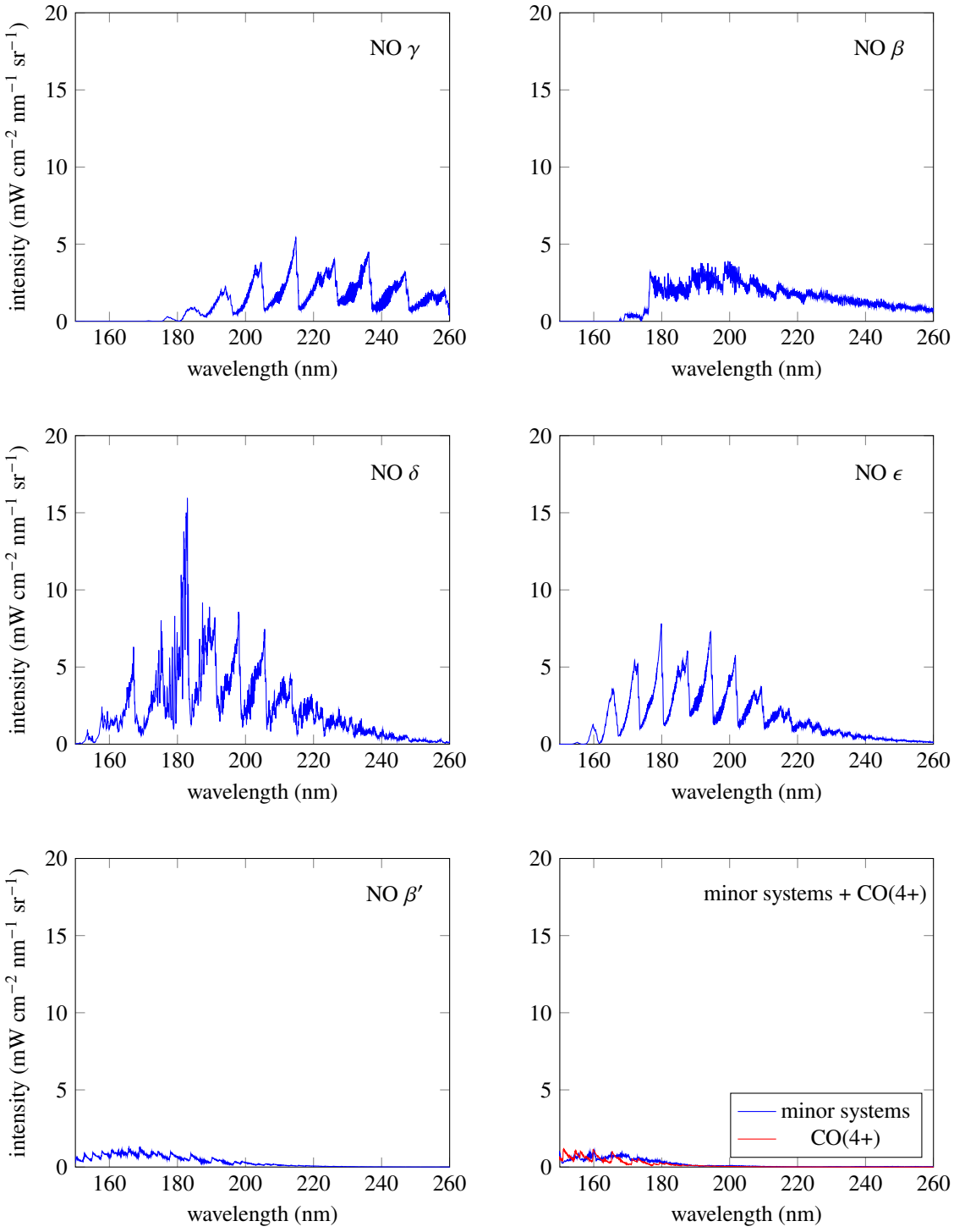

Figure 4.16: Contributions to predicted SPECAIR emission using the temperature profile in Figure 4.14. All calculations were made after SPECAIR was updated as described Section 4.4.2.1.

4.4.2.2 Atomic Emission: 174 nm feature

As for the CO_2/Ar mixture, several atomic lines are heavily optically thick. Of the atomic lines observed, several are due to atomic C, whose intensity is difficult to model accurately without precise knowledge of the CO_2 mole fraction in air. Therefore, we did not focus on these lines. Of the remaining lines, the nitrogen feature at 174 nm ($^2P - {}^2P^o$) is the most important and is heavily optically thick. As before, Doppler broadening is the dominant broadening mechanism, but Van der Waals broadening must be accurately predicted to ensure that the measured intensity is captured. The formulas presented in Section 4.3.2 are also used here to calculate this broadening. Table 4-5 and Table 4-6 show the parameters used in the line broadening calculations. The value of $n_e = 10$ for N_2 is twice the value for an individual N atom. E_p for N_2 corresponds to the energy of the $b\ {}^1\Pi_u$ state, which is the first electronic state connected to the ground state by a dipole allowed transition. For conditions near the center of the plasma jet ($T = 6700\ K$, $p = 1\ atm$), Doppler broadening is calculated to have a FWHM of 2.3 pm, whereas van der Waals broadening is calculated to have a FWHM of 0.3 pm.

Table 4-5: Parameters used in for the line broadening calculation for the 174 nm nitrogen line.

$E_H\ (eV)$	$E_\infty\ (eV)$	$E_i\ (eV)$	l_i
13.6	14.5	10.7	0

Table 4-6: Species-specific parameters used in Eqn. 4-5 for the line broadening calculation for the 174 nm nitrogen line.

Perturber	X_p	E_p , eV	n_e
N	0.31	10.3	5
O	0.29	9.1	6
N_2	0.39	12.6	10

4.4.3 Results and Discussion

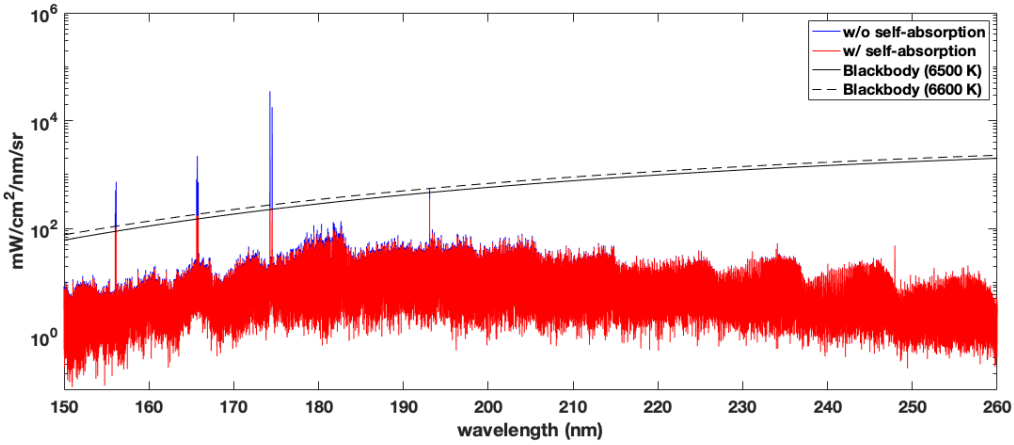

Figure 4.17: SPECAIR calculation based upon the temperature profile in Figure 4.14. Two blackbody curves are included for reference.

Figure 4.17 shows a SPECAIR calculation of equilibrium air emission corresponding to the measured temperature profile in Figure 4.14. The radiative transfer equation is solved along the line of sight to yield the calculated spectrum. The uncertainty in the measured temperature profile leads to a corresponding uncertainty in the calculated intensity profile. This uncertainty is less than 5% across the entire wavelength range and, for wavelengths above 160 nm, is less than 3%. Prominent atomic features include the 174 nm ($^2P - {}^2P^o$) atomic line of nitrogen as well as three atomic carbon lines at 156 ($^3D^o - {}^3P$), 166 ($^3P^o - {}^3P$), and 193 nm ($^1P^o - {}^1D$). The molecular structure is primarily composed of nitric oxide molecular bands: the $\gamma\left(A\,^2\Sigma^+ - X\,^2\Pi\right)$, $\beta\left(B\,^2\Pi - X\,^2\Pi\right)$, $\delta\left(C\,^2\Pi - X\,^2\Pi\right)$, $\epsilon\left(D\,^2\Sigma^+ - X\,^2\Pi\right)$, and $\gamma\left(B'\,^2\Delta - X\,^2\Pi\right)$ systems. The molecular bands of NO are not heavily optically thick. The difference in intensity between the calculations of NO emission with and without self-absorption is very small over a large portion of the spectrum and is maximal around 180 nm, where the difference grows to a factor of 2. The primary effect of self-absorption is on the atomic lines such as the nitrogen feature at 174 nm, which is optically thick. Figure 4.18 (top) shows a comparison between the experimental results and the original SPECAIR calculation, after convolving with the measured slit function. Figure 4.18 (bottom) shows a comparison between experimental results and the updated SPECAIR calculation after convolving the SPECAIR calculation in Figure 4.17 with the measured slit function. The updates to the SPECAIR calculation (red) significantly improve the agreement with the experiment at wavelengths below 200 nm.

The agreement between the updated SPECAIR calculation and the experiment is quite good down to approximately 180 nm. The amplitude of the nitrogen feature at 174 nm—which is very sensitive to line broadening estimates because of strong self-absorption— appears to be

well predicted. Below 180 nm, SPECAIR is found to underpredict the observed molecular structure of the spectrum. This suggests that sources of emission are missing in the SPECAIR calculation. Assuming that the measurements are correct, we see two possible reasons for a discrepancy with the model. These are described in the following two sub-sections.

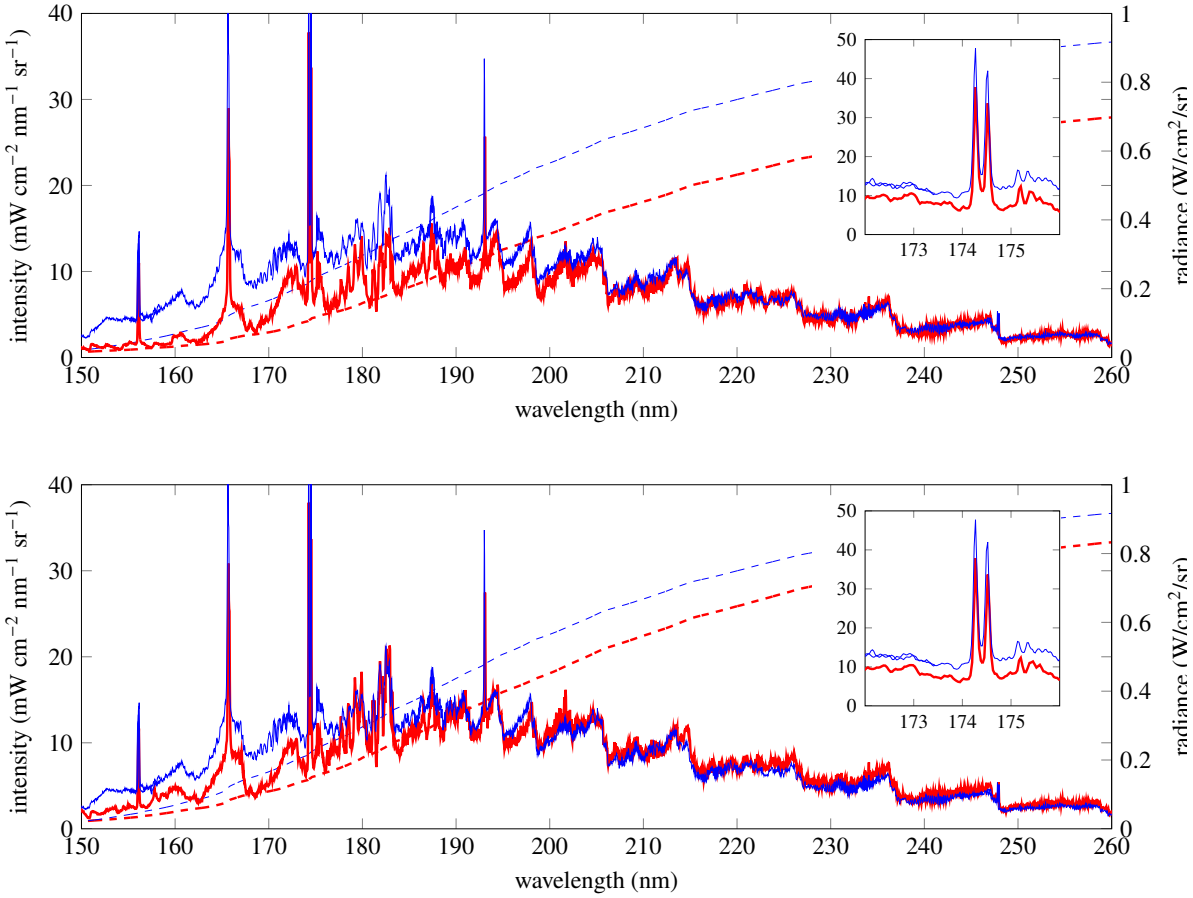

Figure 4.18: ***(top)*** **Comparison between experiment (blue) and original SPECAIR calculation (red).** ***(bottom)*** **Comparison between experiment (blue) and updated SPECAIR calculation (red).**

SPECAIR Comparison with Low-Temperature Photoabsorption Data : Chang *et al* (Chang, Cooper et al. 1993) used electron energy loss spectroscopy to measure photoabsorption cross sections from nitric oxide. In their experiments, NO was taken from a compressed cylinder and would have been essentially at or close to room temperature. In 2007, Kato *et al* (Kato, Kawahara et al. 2007) performed another set of electron energy loss spectroscopy measurements targeting NO and noted good agreement between their measurements and those of Chang *et al*. Figure 4.19 shows digitized data from Figs. 2 and 3 of Chang *et al* (Chang, Cooper et al. 1993). SPECAIR was found to predict the bound-bound transitions fairly accurately down to wavelengths of approximately 145 nm. It does not currently model the continuum that is seen in the measurements of Chang et al. If this

continuum is manually added to the SPECAIR calculations, the resulting agreement with the cross-sectional measurements of Chang *et al* is shown in Figure 4.19 (right). The bound–bound structure below 160 nm is almost entirely dominated by the β', K − X, and Q − X systems of NO. In their paper, Chang *et al* report a spectral resolution FWHM of 0.048 eV for their measurements. However, they do not give the instrument lineshape function. Therefore, a Gaussian lineshape with an FWHM of 0.048 eV is assumed for the instrument function and is applied to the SPECAIR calculation. Because of this assumption, and also because the data were digitized from Chang *et al*, the comparison shown in Figure 4.19 should be taken as indicative only.

Figure 4.19 suggests that there is a continuum source of emission/absorption from nitric oxide in the VUV. To our knowledge, the source of this "continuum" has not been identified. The underlying broadband structure appears to be from a true continuum, as opposed to a large broadening of spectral features such that they are merged. If this is indeed the case, then inverse photodissociation would appear to be the culprit for the missing source – as opposed to predissociation, which would lead to a broadening and weakening of spectral features, but not to a broad continuum. The data reported by Chang *et al* were taken from nitric oxide at room temperature. Therefore, the reported cross sections would have been measured from the ground electronic and ground vibrational level and would not allow us to account for vibrational excitation of the nitric oxide within the plasma jet studied in this work. However, to arrive at an order-of-magnitude estimation of the impact of the observed continuum on the spectrum from high-temperature air as measured in the torch, these cross sections were assumed to be independent of vibrational quantum number. In other words, the cross sections are simply shifted by the energy of the particular excited vibrational level with respect to the ground vibrational level. This enabled an estimation of the emission that might be expected from the recombination $N + O \rightarrow NO$, if this is indeed the source of the observed continuum. Figure 4.20 shows the resulting comparison. The fairly good agreement suggests that such a continuum may indeed explain part or all of the observed discrepancy. Note that the overprediction of SPECAIR below 150 nm when accounting for this continuum is not necessarily problematic because a portion of the actual emitted signal could be absorbed by cold O_2 in the boundary of the plasma jet. Vibrationally specific photoabsorption cross sections for NO, such as those presented for the O_2 molecule by Allison *et al* (Allison, Dalgarno et al. 1971), would help in assessing this hypothesis.

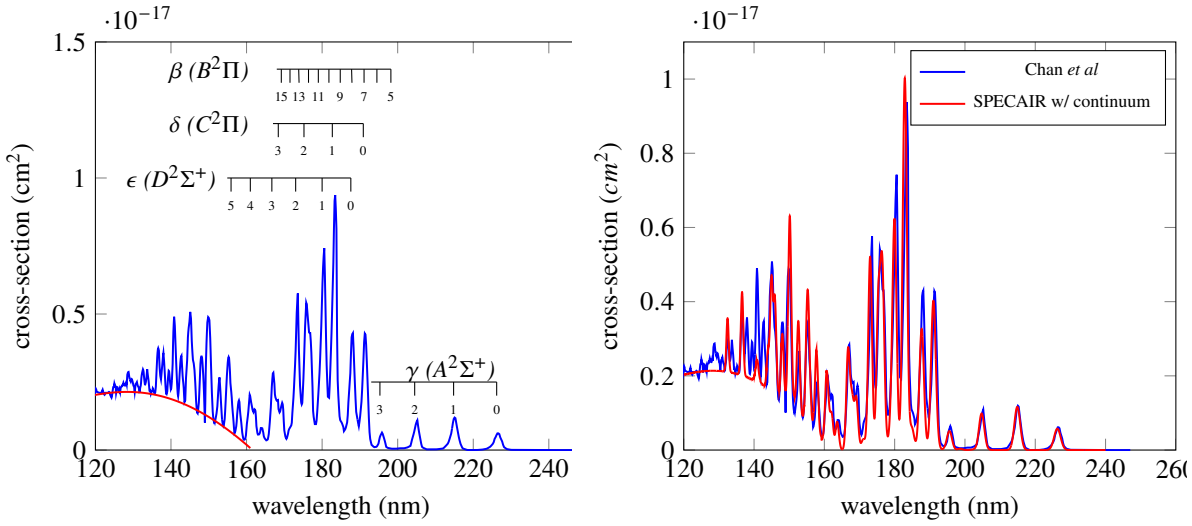

Figure 4.19: *(left)* Photoabsorption cross-sections measured by Chang *et al* – Figs. 2 and 3 of their paper (Chang, Cooper et al. 1993). The red curve denotes the underlying continuum that is observed. *(right)* Comparison between measurements of Chang *et al* and SPECAIR. The continuum shown on the left portion of the figure has been manually added to the SPECAIR calculation.

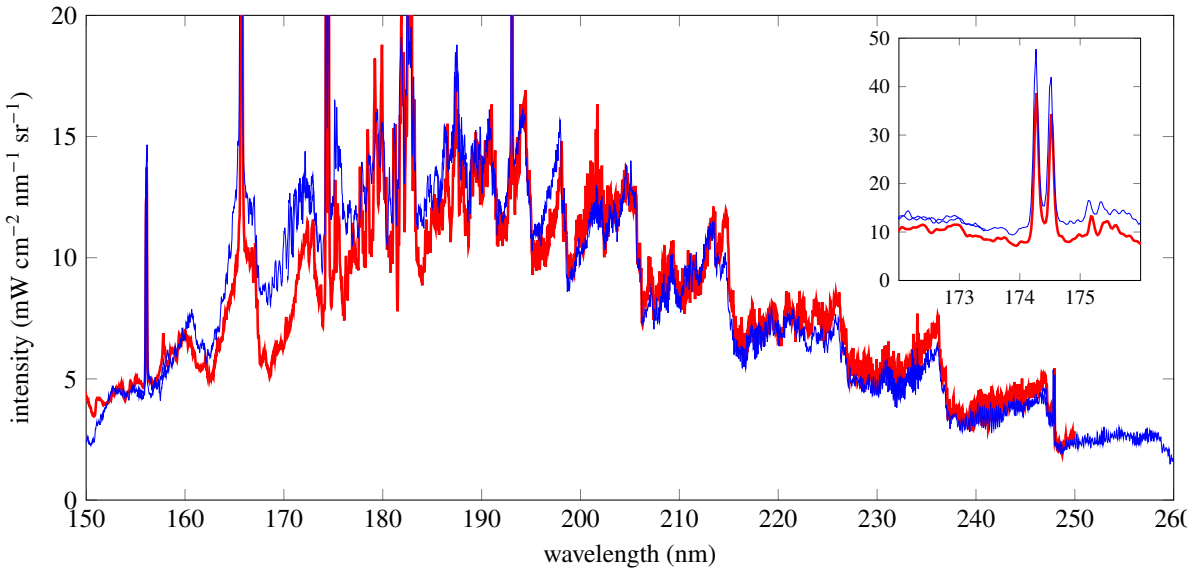

Figure 4.20: Experiment and SPECAIR comparison – SPECAIR is red and experiment is blue. The SPECAIR calculation includes the estimate of continuum based upon the data of Chang *et al* (Chang, Cooper et al. 1993).

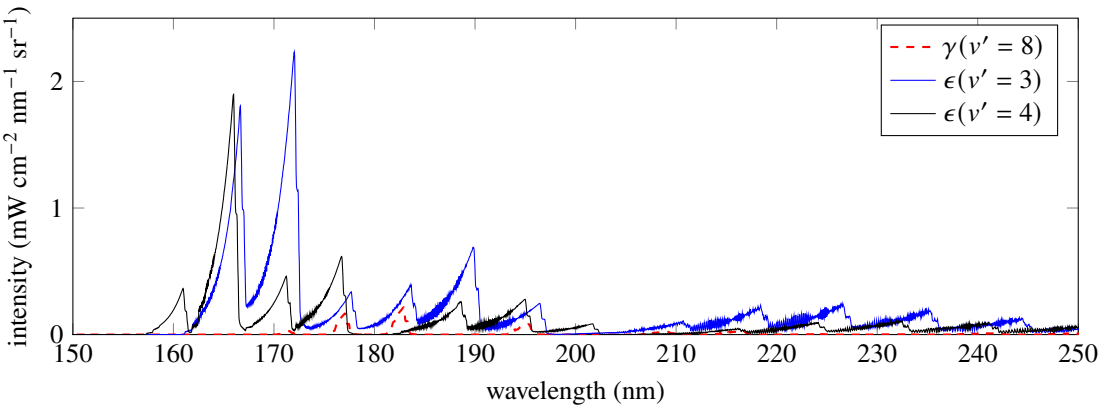

Figure 4.21: Calculated emission from specific vibrational levels of the ϵ and γ systems of NO using the temperature profile in Figure 4.14.

Perturbations Between the $^2\Sigma^+$ States of NO : A second potential candidate for the observed discrepancy would be additional excited state perturbations in the NO molecule that are not accounted for. De Vivie and Peyerimhoff (de Vivie and Peyerimhoff 1988) performed a comprehensive set of calculations with the goal of identifying and characterizing all electronic states of NO – including perturbations among the various states – up to the dissociation limit. They used a basis set composed of molecular and atomic orbitals in order to fully describe the molecular eigenstates and to calculate electronic transition dipole moments. They noted that their calculations are slightly less accurate than studies focused on a more limited subset of electronic states because of computational limitations. Indeed, the electronic transition dipole moment functions provided by De Vivie and Peyerimhoff are not used in SPECAIR calculations as other models were found to provide a better comparison with experimental data (Laux 1993). However, a big advantage of their calculation is the relatively complete picture that it provides of the various electronic states. They address the aforementioned perturbations among the various $^2\Pi$ states that were modeled by Gallusser and Dressler (Gallusser and Dressler 1982) and that are accounted for in SPECAIR. In addition, they also discuss perturbations among certain $^2\Sigma^+$ states. They note that the $A\,^2\Sigma^+$ and $D\,^2\Sigma^+$ (associated with the γ and ϵ molecular systems) interact with the $I\,^2\Sigma^+$ state and a second repulsive state that they label the $2\,^2\Sigma_v^+$ state (referred to as the $A'\,^2\Sigma^+$ state by Miescher (Miescher 1978). These interactions lead to perturbations in the $v = 8$ vibrational level of $A\,^2\Sigma^+$ and $v = 3 - 4$ of $D\,^2\Sigma^+$. Figure 2 in the article by De Vivie and Peyerimhoff (de Vivie and Peyerimhoff 1988) shows the results of these perturbations on the electronic structure. A SPECAIR calculation of high-temperature air emission (using the temperature profile in Figure 4.14) accounting only for the emission coming from these vibrational levels is shown in Figure 4.21. These levels are responsible for a large portion of the emission at wavelengths between

160 and 180 nm, where the discrepancy between calculation and experiment is largest (see Figure 4.18). Perturbations of these levels could therefore potentially account for the discrepancy seen with the measurements.

4.5 Perspectives

The work presented in this chapter resulted in improved accuracy in the modeling of high temperature radiation from CO and air. In the case of CO, five electronic transition moment functions available in the literature (2 of which were virtually identical) were tested against our experimental measurements. The models of Kirby (Kirby and Cooper 1989) and Spielfiedel (Spielfiedel, Tchang-Brillet et al. 1999) were found to give the best agreement with the experiment. In the case of air, discrepancies remain between the predictions and measurements. However, by accounting for perturbations among the $^2\Pi$ states of *NO*, the agreement between prediction and measurement was significantly improved. The current iteration of SPECAIR therefore accounts for these perturbations.

Chapter 5 : Chemical non-equilibrium studies in a CO_2/Ar mixture

The work in this chapter was funded by the ANR JCJC (« jeunes chercheurs ou des jeunes chercheuses ») grant CO2REC and was performed by Corentin Grimaldi during his thesis at laboratoire EM2C. The thesis was directed by Christophe Laux and co-supervised by the author (Sean McGuire). The material presented here was taken or adapted from the thesis manuscript. The work addressed two scientific goals. The first goal was to experimentally characterize a chemically recombining non-equilibrium CO_2 plasma by conducting measurements showing the evolution of the temperature and chemical composition. The second goal was to then compare the measurements against predictions from chemical kinetic models in the literature, to see if the measurements were consistent with these predictions. The motivation behind these goals is explained in the next section.

5.1 Background and Context

5.1.1 CO_2 conversion

CO_2 reforming – specifically the conversion of CO_2 into CO – has received a significant amount of attention over the past 20 years. Lebouvier *et al* published a 2013 review article giving an overview of this technology (Lebouvier, Iwarere et al. 2013). They specifically concentrated on the potential for plasma-based CO_2 reforming schemes. The CO produced via the reforming process may be used as an input for various chemical processes that generate value-added products. There are different potential uses for such a reforming process (Bogaerts and Centi 2020, Centi and Perathoner 2020) which remains limited to laboratory scale experiments. One example is production of syngas which, among other things, is used in the coal-to-liquids (CTL) and gas-to-liquids (GTL) processing techniques that produce liquid hydrocarbons. Figure 5.1 summarizes the basic steps involved in these processing techniques, as they are currently implemented. Either coal gasification or natural gas reforming is used to produce a syngas (CO/H_2) mixture. Fischer-Tropsch synthesis is then used to produce liquid hydrocarbons. Optimal use of Fischer-Tropsch synthesis requires a H_2:CO ratio of approximately 2 (Lebouvier, Iwarere et al. 2013). Therefore, if the initial goal gasification or natural gas reforming phase does not produce this ratio, an additional step involving the water-gas shift can be employed wherein the original syngas mixture is reacted with water vapor to alter the hydrogen and carbon monoxide ratios:

$$CO + H_2O \rightleftharpoons CO_2 + H_2$$

From the standpoint of greenhouse gas emissions, both coal gasification and the water-gas shift reaction emit significant quantities of CO_2. Furthermore, these reactions generally require high temperatures, and the furnaces used to provide the required thermal energy result in additional greenhouse gas emissions. Natural gas reforming is a much cleaner alternative. The main inconvenience associated with natural gas reforming is that the current mechanisms used require the use of a catalyst, which introduces the problem of catalyst deactivation.

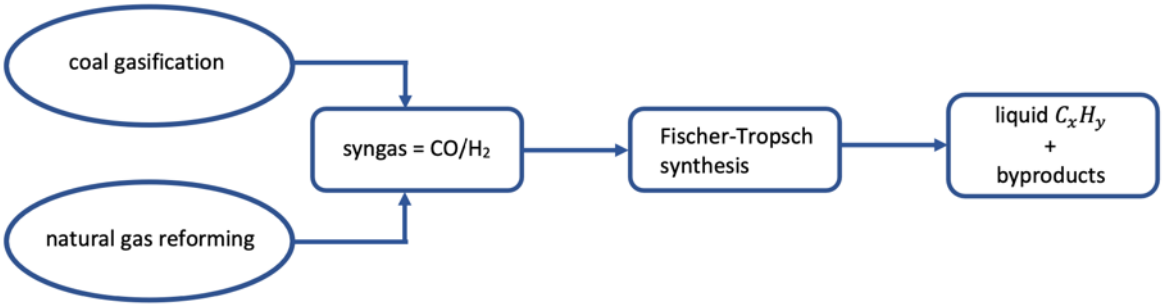

Figure 5.1: Steps involved in the coal-to-liquid and gas-to-liquid processing techniques. Either coal gasification or natural gas reforming can be used to produce the syngas (H_2/CO) which is then processed to produce the liquid hydrocarbons. Figure adapted from(Lebouvier, Iwarere et al. 2013).

Plasma dissociation of CO_2 into CO is a proposed alternative to the coal gasification and natural gas reforming steps that produce syngas. With this process CO_2 is converted into CO and O_2 via the following global reaction:

$$2CO_2 \rightleftharpoons 2CO + O_2$$

This reaction is highly endothermic and thus requires energy input that is provided via the plasma. Upon dissociation of CO_2, the CO is mixed with water-vapor and reacted via the water-gas shift reaction to produce the desired syngas. While the water-gas shift reaction involves the emission of CO_2, the emitted quantity of CO_2 remains less than the original quantity of CO_2 at the start of the CO_2 dissociation step (neglecting any CO_2 emissions from the use of any furnace used to supply the thermal energy). For this approach to provide a clean alternative to syngas production, a clean source of energy must be used. For it to be viable, the CO_2 must be dissociated into CO in a quick and efficient manner.

Current plasma-based approaches for CO_2 dissociation into CO can be broken down into two categories: *thermal* and *non-thermal* approaches (Kobayashi, Osaki et al. 2002, Oberreuther,

Wolff et al. 2003, Fridman 2008, Paulussen, Verheyde et al. 2010, Kozák and Annemie 2014, Bak, Im et al. 2015). Thermal techniques heat CO_2 to high temperature (4000 – 5000 K) where it dissociates naturally to CO. These techniques are often inefficient but achieve high conversion rates, meaning that they can convert large quantities of CO_2 relatively quickly. Non-thermal techniques involve non-equilibrium electrical discharges. The high electric fields lead to ionization, excitation, and dissociation processes. Vibrational excitation of CO_2, in particular, leads to efficient production of CO. Though more efficient, these non-thermal approaches are typically limited to relatively low conversion rates. Examples of non-thermal approaches include nanosecond repetitively pulsed discharges (NRP) (Bak, Im et al. 2015) and dielectric barrier discharges (DBD) (Paulussen, Verheyde et al. 2010), among others. One goal of current research in this scientific community is to design a reactor capable of converting large quantities CO_2 with an efficiency as close to the ideal limit as possible.

A primary problem that limits the conversion efficiency of a reactor is the rate at which the CO produced recombines back into CO_2. If a large percentage of the CO produced recombines into CO_2, the reactor will have a low efficiency. This recombination rate therefore represents an important constraint in the design of an efficient reactor. The challenge is to design a system where CO recombination pathways are kinetically blocked, preventing recombination back into CO_2. This, requires a detailed understanding of the recombination kinetics, sufficiently detailed to permit the state-specific recombination rates to be calculated. To that end, vibrationally specific codes have been developed to model recombination kinetics(Kozák and Bogaerts 2015, Ponduri, Becker et al. 2016). However, these codes are based on cross-section sets measured only at low temperatures. Recombination kinetics have been experimentally studied. Of note are the measurements of Huczko and Szymafiski (Huczko and Szymański 1984), Yang et al (Li, Zhang et al. 2017, Yang, Shen et al. 2018), Brabbs and Belles (Brabbs and Belles 1967), and Hardy et al (Hardy, Gardiner Jr et al. 1978). Huczko and Szymafiski and Yang et al used an arc discharge to produce a high temperature CO_2 mixture before studying its recombination. Both authors targeted maximum mixture temperatures of around 3 500 K, as estimated using power balance arguments. Meanwhile, Brabbs and Belles and Hardy et al used shock tubes to produce the heated CO_2 mixture. Brabbs and Belles achieved temperatures of around 3 600 K in their study. Measurements at lower temperature have also been pursued by Kondratiev and Intezarova (Kondratiev and Intezarova 1969) and Slanger et al (Slanger, Wood et al. 2003). Though there seems to be general agreement within the CO_2 conversion community that a cooling rate of $10^7\ K/s$ is needed to avoid back recombination of CO and O into CO_2 (Lebouvier, Iwarere et al. 2013, Bogaerts and Centi 2020), researchers continue to cite the need for recombination studies as a means for improving the energy efficiency of plasma-based CO_2 conversion (Bogaerts and Centi 2020).

The ANR project CO2REC proposed to extend this dataset to temperatures ranging from 3000 – 9000 K. Such a dataset would provide critical information needed to ultimately design a research reactor. Note that, under equilibrium conditions, a gas composed of CO_2 at 300 K will be predominantly composed of CO between approximately 4000 – 6000 K and thus the proposed temperature range is ideal for looking at CO recombination into CO_2 (McBride and Gordon 1992).

5.1.2 Mars/Venus atmospheric entry

The chemical kinetics of CO_2 mixtures are relevant for hypersonic entry into Mars and Venus atmospheres, which are composed primarily of CO_2. Such missions necessarily involve chemically reacting CO_2 mixtures. Properly modeling the nonequilibrium dynamics of such flows requires validated chemical models. Furthermore, characterization of ground testing facilities used to conduct tests in preparation for these missions also requires validated chemical models. Among these facilities, shock tubes reproduce very accurately the shock whereas plasma arcjets or torches reproduce the enthalpy of the shock layer and the heat flux experienced by the vehicle. Arcjets heat the tested gas to the desired enthalpy, and the flow is then expanded to supersonic or hypersonic velocities using a nozzle. As in the real flight case, the expansion can lead to a recombining nonequilibrium flow. Numerical simulations are then required to predict the conditions in the test section. To that end, three mechanisms for CO/CO_2 dissociation kinetics have been developed at NASA and used in atmospheric entry calculations. These were the three mechanisms tested in this work and are as follows:

- *Park mechanism*: Chul Park introduced his CO/CO_2 model in 1994 (Park, Howe et al. 1994). His objective was to propose a kinetics model for future NASA missions to Mars. It quickly became the standard model used at NASA for Mars entry flow field simulations. The Park model is a two-temperature model in which the electron temperature is taken to be equal to the vibrational and electronic excitation temperature. This common temperature is denoted T_{ve}. The translational and rotational temperatures of heavy particles are taken to be equal and denoted as T_{tr}.The flow behind a high-speed shock in a low-density gas tends to be in a state of thermochemical nonequilibrium and Park's two-temperature model is capable of describing cases where $T_{ve} \neq T_{tr}$. The same assumptions were used and validated in his 1993 model for Earth entry missions (Park 1993).
- *Johnston and Brandis mechanism*: Johnston and Brandis proposed an update of the Park chemical kinetic model in 2014, 20 years after Park's 1994 paper (Johnston and Brandis

2014). Up until that point, Mars entry simulations using the Park model focused on accurate convective heating predictions. These are less sensitive to the chemical kinetics of the shock-heated mixture than the radiative heating component. However, concerns began to arise because radiative heating was expected to be significant for the new concepts that were being proposed, such as Hypersonic Inflatable Decelerators (HIADs). In 2010, Cruden measured the CO 4th positive, and the CN Violet bands at pressures and velocities ranging from 0.1 – 1.0 Torr and 6 – 8 km/s, respectively (Cruden, Prabhu et al. 2010). Johnston and Brandis tuned the Park model to fit the EAST measurements, focusing on the dissociation rates of CO_2, CO, O_2, and NO along with the CN + O = NO + C and CO + N = CN + O reaction rates. The most notable modification was an increase in the CO dissociation rate by a factor larger than five, while keeping the original CO_2 dissociation rate proposed by Park – thus increasing the rate at which CO dissociates with respect to CO_2. These modifications provided good agreement with the EAST measurements.

- *Cruden mechanism:* In 2018, Cruden performed experiments in the NASA EAST facility in pure CO(Cruden, Brandis et al. 2018). The goal was to isolate the CO kinetics. The measurements were performed at a pressure of 0.25 Torr and shock velocities ranging from 3.4 – 9.5 km/s. The emission and absorption signals were used to measure the density of CO, C, and C_2, and to extract temperature relaxation behind the shock. These data were then used to derive the rate of CO dissociation, the rate of C_2 dissociation, and the rate of neutral exchange between CO and C_2. Cruden found that the Johnston model matched the data obtained at velocities above 6.6 km/s but not below. Therefore, he proposed an update of the Johnston model for shock velocities below 6.6 km/s (in other words, at lower temperatures) using dissociation rates from Hanson (Hanson 1974), Fairbairn (Fairbairn and Gaydon 1997), Warnatz (Warnatz 1984) and Ebrahim (Ebrahim and Sandeman 1976). The possibility of reconciling the two kinetic mechanisms of Johnson and Cruden by proposing a single set of rates that describes all data remains an open question.

5.2 Experimental setup and methodology

As discussed in Section 3.2, the plasma torch produces a plasma at or close to equilibrium with a temperature of 6 500 – 7 500 K. To trigger chemical recombination and force the mixture out of chemical equilibrium, a water-cooled tube is used. The water-cooled tube is referred to as the recombination tube in this manuscript, and has a constant diameter of 1 cm. The wall temperature is maintained at $20\ °C$ because of the water-cooling system. A schematic of the recombination tube mounted to the plasma torch is shown in Figure 5.2. The velocity of the

plasma as it traverses the tube varies but is generally on the order of several hundred meters per second. The length of the tube is modular but is usually varied between 5 – 40 cm. Given the velocity, the time for the plasma to transit the tube is on the order of several hundred microseconds. Meanwhile, the temperature varies from a temperature of several thousand Kelvin on centerline to a temperature of 300 K at a radial distance of $r = 0.5\ cm$ where the wall is located. This enormous thermal gradient results in a large transfer of thermal energy from the plasma to the wall. This thermal gradient leads to rapid gas cooling which, in turn, triggers chemical recombination. The temperature at the outlet of the tube depends upon the tube length and mixture used. A typical result and order-of-magnitude estimate would be a drop in temperature of about 3 000 K over a tube length of $\sim 20\ cm$, with a corresponding transit time on the order of $500\ \mu s$. This corresponds to a cooling rate on the order of $10^7\ K/s$.

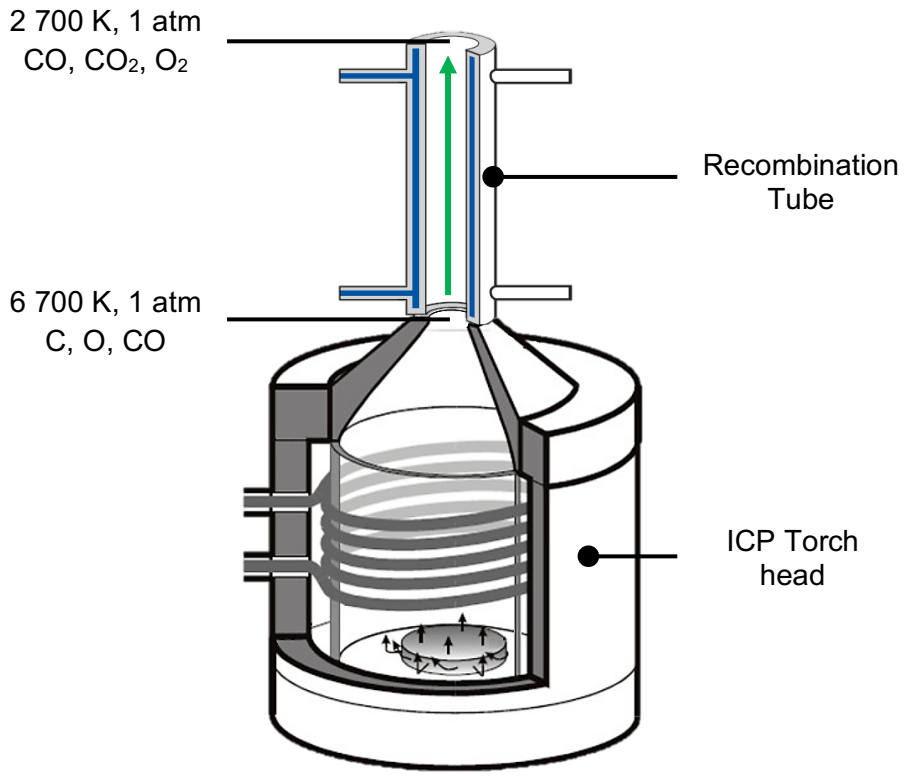

Figure 5.2: The recombination tube is water-cooled (indicated in blue) and mounted above the torch to rapidly cool the plasma and trigger chemical recombination.

The operating conditions used for the measurements presented here are summarized but explained in detail in (Grimaldi 2023). A total gas flow rate of 3.47 g/s was used, with a CO_2/Ar composition of 10%/90% by mass. For torch operation, a plate power of 39 kW was used and the gas was injected via the radial and swirl injectors in equal quantities (radial: 50%, swirl: 50%). These choices were made based upon several criteria involving the symmetry of the jet

produced by the torch, the stability of the plasma torch when operating with the mixture, the velocity of the plasma jet, and the proximity to thermochemical equilibrium at the torch exit.

Figure 5.3 shows the optical setup used for Infrared Optical Emission Spectroscopy (IR-OES) measurements. The camera used was an IRC-800 camera produced by IR Cameras LLC. Parabolic mirrors were used to avoid dispersion given that a wide wavelength range was targeted. All measurements were calibrated in wavelength and absolute intensity. For calibration in absolute intensity, a modified Tungsten ribbon lamp (Optronics Laboratory model 550A lamp) calibrated to NIST standards was used. The calibration accounted for absorption of water vapor and carbon dioxide in the ambient air optical pathway. Finally, the measured line-of-sight spectra were Abel-inverted to produce a radially resolved local volumetric emission profile. This profile was then averaged to determine the gas temperature, CO concentration, and CO_2 concentration. A detailed explanation of the optical setup and measurement procedure can be found in (Grimaldi 2023).

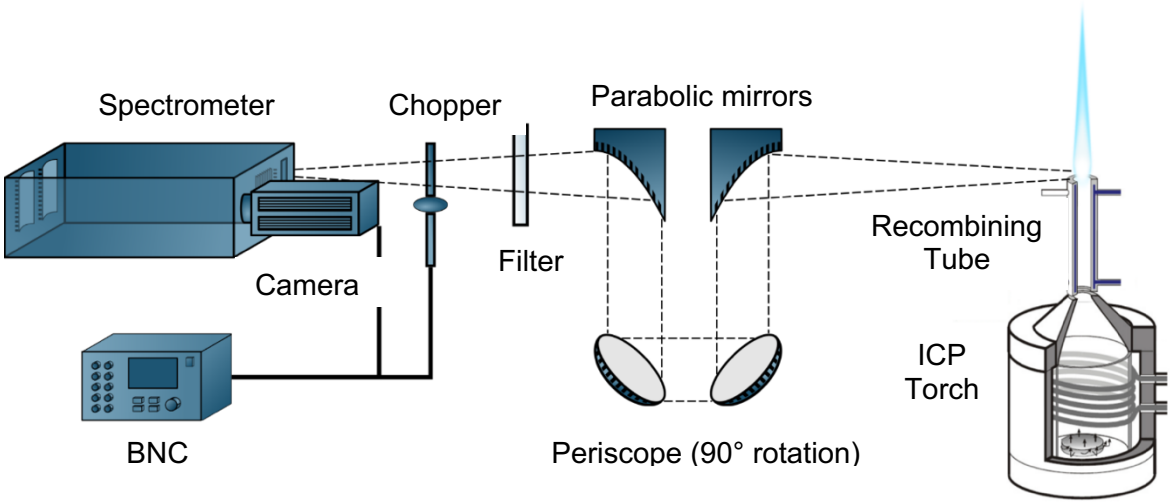

Figure 5.3: Experimental setup used for Infrared Optical Emission Spectroscopy (IR-OES) measurements.

5.3 Spectral analysis

The measured spectra are path integrated along the line-of-sight of the spectrometer. To obtain a spatially resolved volumetric emission profile, these spectra must be Abel inverted. For recombination tube lengths less than 20 cm, this Abel inversion resulted in unacceptably high uncertainties on jet centerline at $r = 0\ cm$. Nonetheless, at slightly off-center radii of $r =$

$0.1\ cm$, the uncertainty remained reasonable. Given that our prior assumption of axisymmetry implies that the radial slope on centerline goes to zero, all values measured at $r = 0.1\ cm$ were assumed equal to the centerline values. This assumption was only necessary for recombination tube lengths less than 20 cm because, above this tube length, the uncertainties after Abel inversion remained acceptably small for all radial points.

Once the spectra were Abel inverted, a spectral fitting procedure was used to determine the corresponding temperature, CO mole fraction, and CO_2 mole fraction. Two separate spectral regions were analyzed – the $4.1 - 5.6\ \mu m$ and the $2.3 - 3.4\ \mu m$ regions. The $4.1 - 5.6\ \mu m$ region contains the CO fundamental bands and CO_2 ν_3 bands. The $2.3 - 3.4\ \mu m$ region contains the CO first overtone, CO_2 $\nu_1 + \nu_3$, and CO_2 $2\nu_2 + \nu_1$ bands. A separate analysis of both spectral regions yielded the same results in terms of temperature and chemical composition. Therefore, only the analysis of the $4.1 - 5.6\ \mu m$ spectral region is presented here.

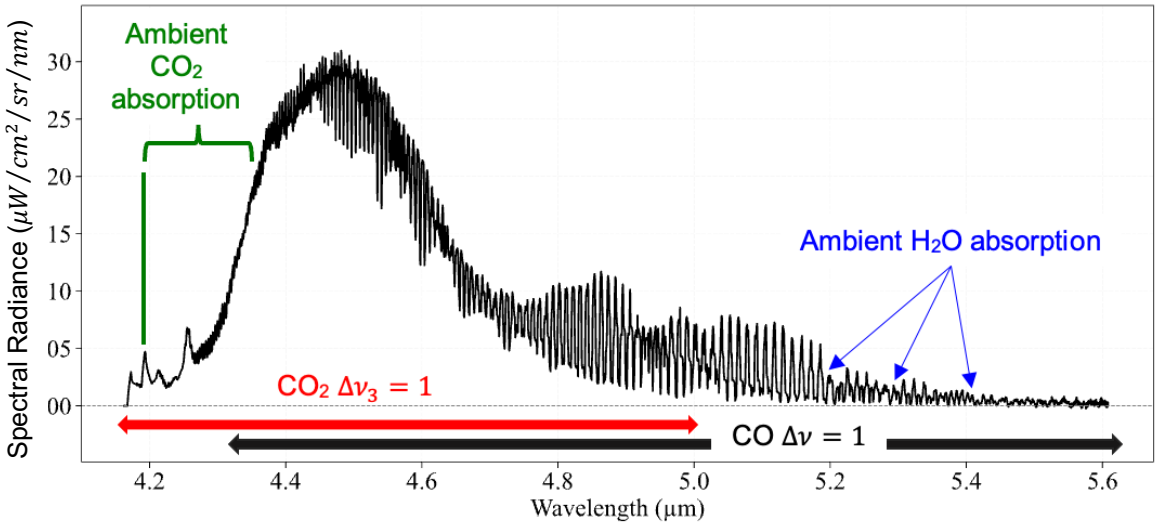

Figure 5.4: Sample measured spectrum after Abel-inversion and taken at a radius of $0.15\ cm$ and a recombination tube length of 30 cm.

Figure 5.4 shows a sample spectrum obtained after Abel-inversion. This specific example includes emission from both CO and CO_2 bands, which overlap one another across a wide wavelength range. Ambient absorption from CO_2 has a large impact on the spectrum between $4.2 - 4.3\ \mu m$, with absorption from water vapor in the ambient air having a minor impact at larger wavelengths. To fit the measured spectra, the RADIS radiation code was used (Pannier and Laux 2019), along with the following fitting procedure:

1. The rotational temperature for CO_2 was first determined by fitting the CO_2 $\Delta\nu_3$ bandhead ($00^01 \rightarrow 00^00$) located at $\sim 4.2\ \mu m$. This bandhead is very sensitive to rotational temperature and thus served as a good indicator for the corresponding value.

At this stage, the vibrational temperature of CO_2 was assumed equal to the rotational temperature so that a preliminary estimation of emission from CO_2 bands was obtained at this step.

2. The CO density and temperature were determined by fitting the spectrum in the $5.0 - 5.6\ \mu m$ region which contains only emission from CO bands. The CO density was first determined by matching the amplitudes of emission lines between 5.181 µm and 5.190 µm. Next, the temperature was varied to fit the surrounding structure. Only a single temperature was varied as it was assumed that $T_{vib} = T_{rot}$. This region is impacted by ambient H_2O absorption present in the optical path. Absorption by H_2O was computed at 300 K using the HITEMP-2010 database and added to the calculation of CO emission to match the observed absorption. The mole fraction of H_2O present along the 4.25 m optical path was also found by minimizing the residuals. Once this was done, the CO temperature was once again varied, but now accounting for the estimated H_2O absorption. These two last sub-steps – the CO 1T fit and the H_2O absorption fit – were repeated iteratively until convergence, which was typically obtained after two to three iterations.
3. The CO_2 vibrational temperature ($T_{vib} = T_{v1} = T_{v2} = T_{v3}$) was allowed to vary while fitting the spectrum over the $4.5 - 5.6\ \mu m$ interval. The CO 1T fitting routine (performed in step 2) depends on the CO_2 emission and vice versa. Therefore, steps 2 and 3 were performed in an iterative manner until convergence, which was typically obtained after a few iterations.
4. The last step consisted of fitting the absorption from ambient CO_2 present in the optical path. The absorption of CO_2 was computed at 300 K using the HITEMP-2010 database and added to match the level observed. The mole fraction of CO_2 present along the 4.25-m optical path was found by minimizing the residuals over the 4.2 – 4.5 µm region. Once the ambient CO_2 mole fraction was found, the CO_2 2T (Step 3) and the CO 1T (Step 2) fits were run again in an iterative fashion to obtain a final fit.

Figure 5.5 shows the final fit obtained for the spectrum presented in Figure 5.4. This fitting procedure was carried out for all recombination tube lengths studied, and as a function of radius for each tube length. The result was a database of temperature and chemical composition. Table 5-1 shows the fitting results obtained on jet centerline as a function of recombination tube length. A detailed description of all results – including an analysis of the $2.3 - 3.4\ \mu m$ spectral region – can be found in the thesis of Corentin Grimaldi (Grimaldi 2023).

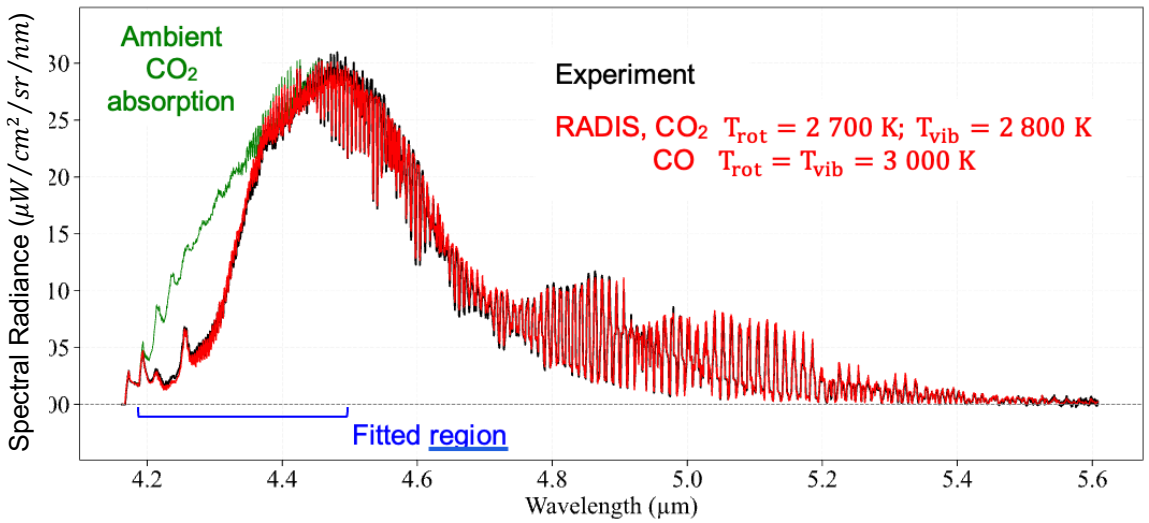

Figure 5.5: Final fit obtained for the measured spectrum presented in Figure 5.4. Note that $T_{vib}^{CO} = T_{rot}^{CO}$ and $T_{vib}^{CO2} = T_{v1}^{CO2} = T_{v2}^{CO2} = T_{v3}^{CO2}$.

Table 5-1: Summary of fitting results on jet centerline ($r = 0\ cm$) for various recombination tube lengths. Below a tube length of 20 cm, no CO_2 is observed at the center of the jet due to the high temperature.

Tube length (cm)	CO T_{rot}=T_{vib} (K)	CO_2 T_{rot} (K)	CO_2 T_{vib} (K)	CO density (m^{-3})	CO_2 density (m^{-3})
0	7 000	-	-	3.9e+22	-
5	6 100	-	-	4.9e+22	-
10	5 800	-	-	6.3e+22	-
15	5 300	-	-	7.6e+22	-
20	4 000	2 900	3 100	1.1e+23	1.3e+22
25	3 400	2 900	3 000	1.3e+23	2.0e+22
30	3 100	2 800	2 900	1.4e+23	2.9e+22
35	3 000	2 700	2 800	1.4e+23	3.5e+22

5.4 Chemical kinetic simulations

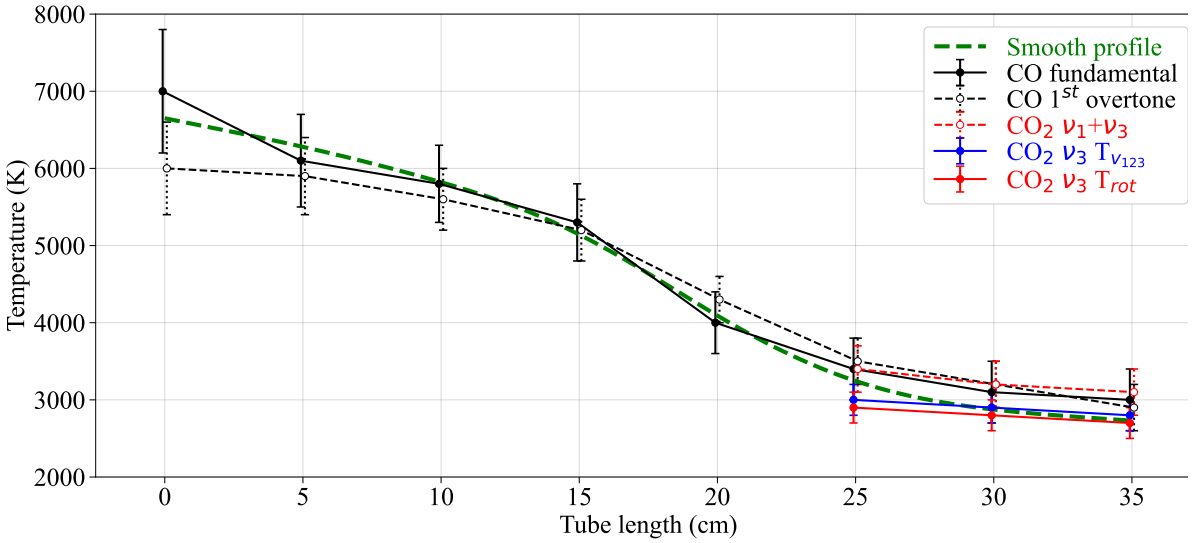

Figure 5.6 : Measured temperature on centerline as a function of tube length. All measurements are shown in the figure to highlight their good agreement.

The goal of this section is to compare the measurements summarized in Table 5-1 with kinetic model predictions. The three kinetic models presented in Section 5.1.2 will be tested against these measurements. Figure 5.6 shows the measured centerline ($r = 0$) temperature profile as a function of tube length. While all temperature measurements agree to within their respective uncertainties, a single curve must be chosen as a nominal input into the chemical kinetic simulations. The chosen curve is shown in green and represents a smoothed average of the measured profiles. To make the desired comparison with kinetic simulations, a 0D assumption is made. This assumption implies that, along the $r = 0$ streamline, the chemical composition only evolves due to chemical reactions and not transport processes such as diffusion or turbulence. We believe that such a hypothesis is justified on the following grounds:

- Radial variations in the flow properties are much larger than axial variations. Axial variations occur over distances of several centimeters whereas radial variations occur over the flow radius of $5\ mm$.
- For an axisymmetric jet, the radial derivatives are zero on centerline. This implies that diffusion processes may be neglected at the radial position $r = 0$.

While the above arguments do not constitute a proof, they suggest that a 0D assumption is reasonable. Once a 0D assumption is made, the measured variation in flow properties with axial distance must be converted to a variation in time. Only then can the measurements be compared with the model predictions as these calculate the evolution of the chemical

composition with time. The correspondence between axial distance and time is governed by the axial flow velocity. Unfortunately, this parameter is not measured directly. However, the mass flow rate of the jet is known. Furthermore, the pressure ($1\ atm$) and temperature in the flow are also known. These parameters are linked by the following equation:

$$\dot{m} = \int_0^R \rho\, u_z(r)\, 2\pi r dr = \int_0^R \frac{p}{rT}\, u_z(r)\, 2\pi r dr \qquad \textbf{5-1}$$

where only the axial velocity profile $u_z(r)$ remains unknown. Three radial profiles were tested for the axial velocity:

- Plug flow velocity profile, $u_z(r) = constant$: This simple model neglects the boundary layer and, as a consequence, corresponds to a fully turbulent flow in a tube where the laminar sublayer is very thin.
- Laminar flow velocity profile, $u_z(r) = A(r - R)(r + R)$: This corresponds to the case of a fully developed laminar flow with temperature-independent properties in a tube of circular cross-section.
- Self-similar velocity profile: $u_z(r) = B\ (h_{gas}(r) - h_{wall})$: In viscous flows with constant mass density ρ, heat capacity c_p, dynamic viscosity μ and thermal conductivity λ, the local momentum balance equation and the local energy balance equation are found to be self-similar and the above relation holds when the Prandtl number is one. For the mixture and temperature range considered, the Prandtl number is indeed close to one. It should be noted, however, that the parameters such as the mass density vary substantially throughout the flowfield in the test case considered and are, therefore, not constant.

The above cases are intended to provide bounds on the possible velocity profiles. Each velocity profile may be used to compute the axial variation in temperature to a temporal profile in temperature, as shown in Figure 5.7. It is found that the centerline velocity is smallest for the plug flow velocity profile and the time to transit the tube is therefore the longest in this case. Meanwhile, the opposite is true for the parabolic velocity profile. The self-similar velocity profile falls in between these two limits. Power balance measurements, wherein the power removed by the water-cooling circuit is compared with the enthalpy drop in the plasma, suggest that the constant velocity profile is the closest to the actual velocity profile. Details are provided in Chapter 5 of (Grimaldi 2023). As can be seen in Figure 5.7, the time to transit the tube varies between $\sim 500\ \mu s$ and $\sim 1200\ \mu s$ depending on the profile chosen. While this uncertainty is large, the results that follow indicate that this uncertainty is acceptable as the differences in the simulated composition don't change drastically between the two limiting cases.

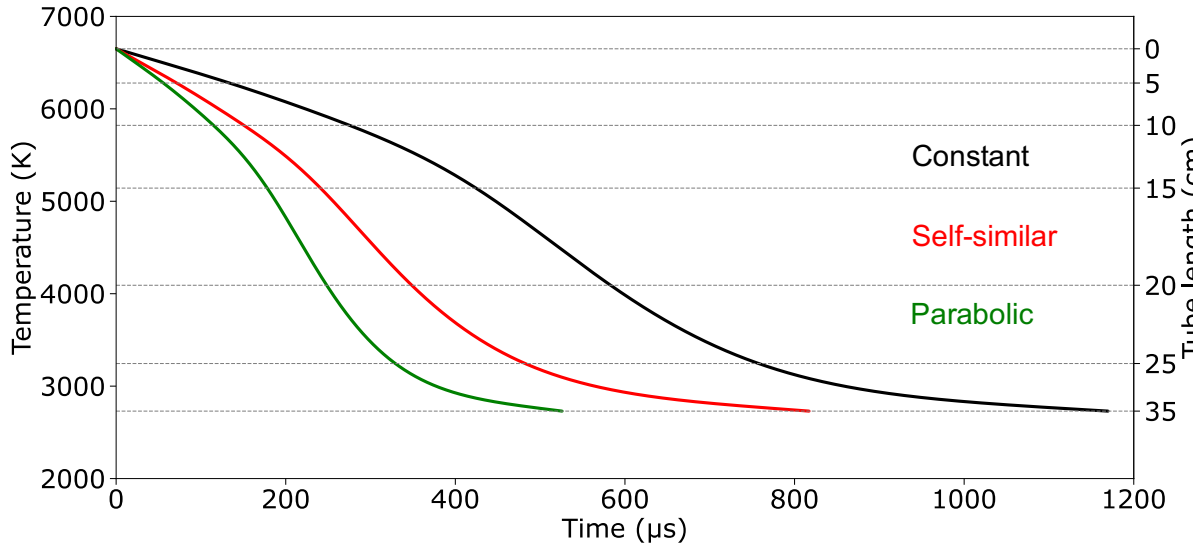

Figure 5.7: Temporal profile of temperature calculated for the various velocity profiles tested.

Now that the temporal evolution of the temperature profile is determined, it is possible to compare the simulations with the measurements. The simulations start from the initial chemical state of the gas at the exit of the torch. This initiation accounts for a small disequilibrium observed at the exit of the torch as described in Chapter 6 of(Grimaldi 2023). Although the temporal profile of the temperature is used for the simulations, we will present all results as a function of tube length. Figure 5.8 - 5.9 show the comparisons between the measured and simulated CO density and CO_2 density. Comparisons with the equilibrium density at the measured temperature and the chemical kinetic simulations using the three velocity profiles are shown. The CO densities are predicted quite well by the models, especially the Johnston model. However, the measured CO_2 densities are between a factor of 5 – 10 larger than the simulated values. This is true regardless of the velocity profile used and thus, even despite the factor of 2 difference in transit times that the various velocity profiles give, the uncertainty in the velocity profile does not account for the discrepancy observed.

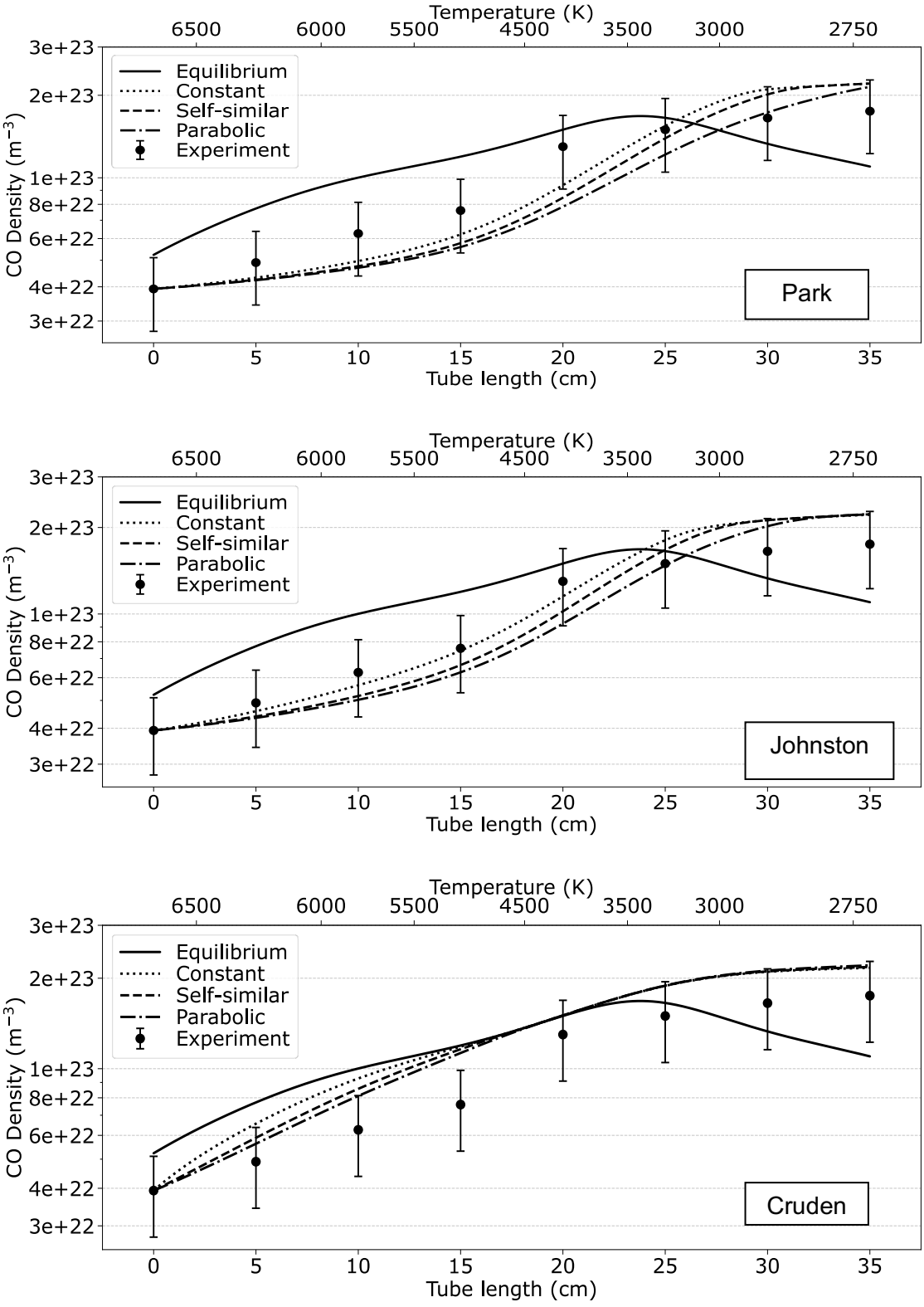

Figure 5.8 : CO density predictions using Park (top), Johnston (middle), and Cruden (bottom) kinetic models, with the constant, self-similar, and parabolic velocity profiles.

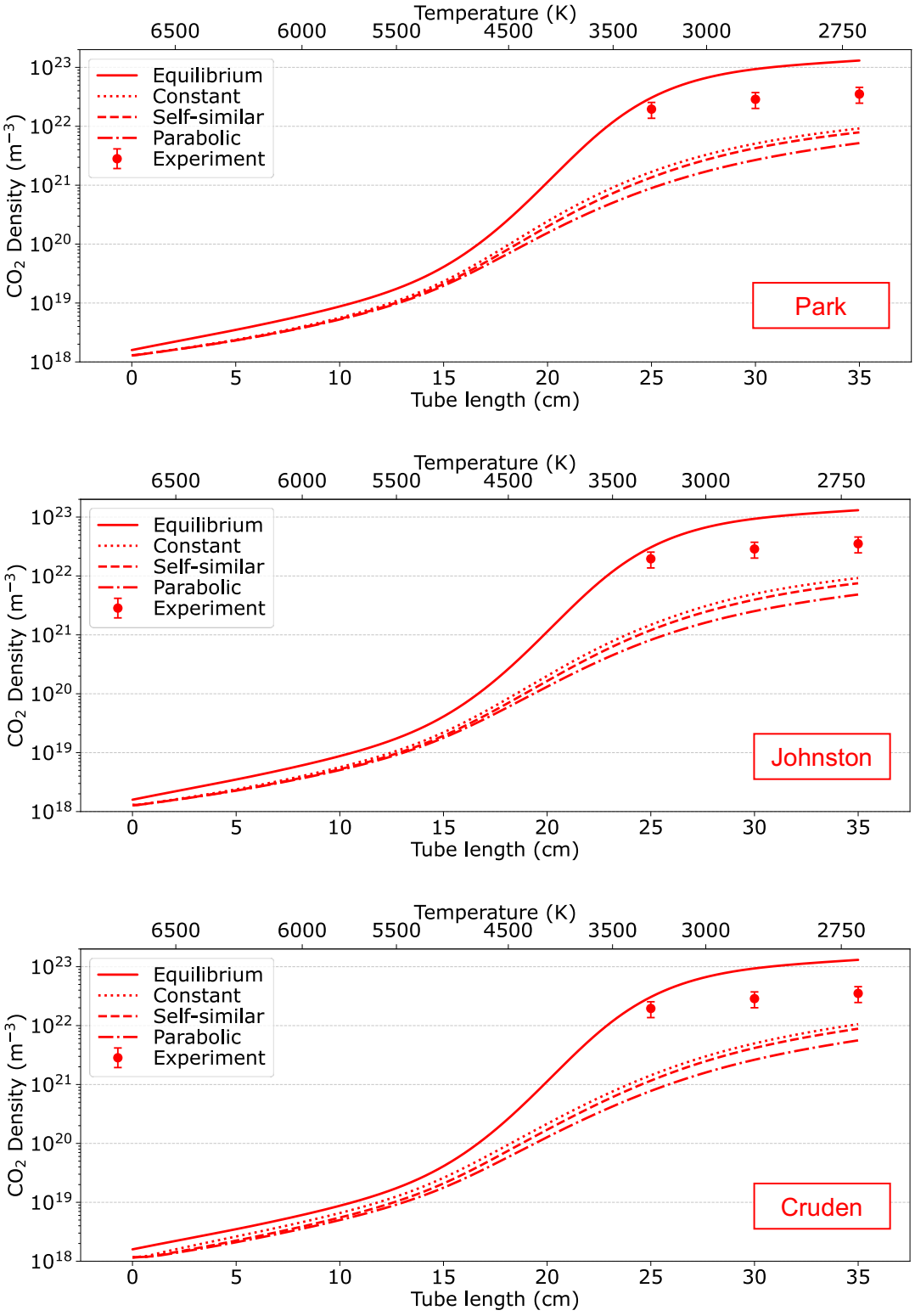

Figure 5.9 : CO_2 density predictions using Park (top), Johnston (middle), and Cruden (bottom) kinetic models, with the constant, self-similar, and parabolic velocity profiles.

5.5 Perspectives

The previous section showed that the models cannot reproduce our measurements of CO_2 density. This fact could be explained by three possible scenarios.

1. The plasma on tube centerline does not behave in a manner consistent with our assumption of a 0D flow. For example, turbulent transport not accounted for in our 0D model could also alter the chemical composition of the jet.
2. The models are not sufficiently detailed to capture the CO_2 recombination process. Indeed, the models used for the chemical simulation are not state specific. A non-Boltzmann vibrational distribution function and any subsequent impact on the global rate is not considered. However, our measurements indicated that both CO and CO_2 follow a Boltzmann vibrational distribution.
3. The kinetic model rate constants are incorrect or important reactions are missing.

The first and third possibilities are, in our view, the most likely. Future work will study the first point. The third point was explored by investigating possible modifications to the models that improve the agreement between the predictions and our measurements. This was done in such a way as to minimize the modifications to the nominal rates proposed by the kinetic models by as small a factor as possible. Indeed, the models themselves are based on experimental data and there is no *a priori* reason to favor one data set over another. The strategy for finding possible modifications can be broken down into three sequential steps:

1. A global sensitivity analysis is performed wherein a large number of modifications to all reaction rates are tested (within a given kinetic model). The resulting spread in the CO_2 density predictions provides an estimate of the sensitivity of the kinetic models to these variations. This global sensitivity analysis showed that the measurements cannot be reproduced by a “small” modification of the rates. Rather, a large modification is required to fit our data.
2. A local sensitivity analysis is conducted wherein the reaction rates are separately modified one by one to identify which modifications have the most impact on the CO_2 density prediction. This local sensitivity analysis shows that 5 reactions determine the CO_2 density predictions. Other reactions play a minor role and are subsequently neglected.

3. A Quasi Monte-Carlo (QMC) investigation is conducted to identify possible modifications that give an acceptable agreement between the predictions and the measurements. Here, simultaneous modifications to the rates of the five previously identified reactions are considered. This is done to account for any potential coupling effects amongst these five reactions. Two different metrics must be introduced at this stage. First, a metric must be defined to determine what constitutes an acceptable level of agreement. Second, a metric must be defined to classify reactions providing an acceptable level of agreement according to their "distance" from the nominal solution. Both metrics can be altered, for example, to favor modifications to certain reactions over others.

The tables below show two of the primary results from the QMC investigation. Each table shows a *mean*, *min*, and *max* value for each model. All of these correspond to a factor by which the nominal rate is multiplied to produce the modified model. The *min* and *max* values show the spread in the possible modifications that give an acceptable agreement. The *mean* value is the average value. Table 5-2 shows the modifications giving the best agreement with experiment. However, the best agreement doesn't account for the uncertainty in the measurements. An alternate classification would be to take all modifications that give an acceptable level of agreement and to classify these modifications according to their proximity to the nominal solution. Table 5-3 shows the modification which is closest to the original models based upon our criterion for classifying this distance. In other words, Table 5-3 shows the minimum change to the model that gives an acceptable level of agreement. Finally, note that there are plenty of other modifications that give acceptable level of agreement. Indeed, the QMC analysis gave several different types of modifications as detailed in(Grimaldi 2023).

Table 5-2 : Reaction rate factors found to give the best agreement between the CO_2 density prediction and the measurements.

Model / Reaction	Park		Johnston		Cruden	
	mean	min – max	mean	min – max	mean	min – max
$x_{O_2+M \leftrightarrow O+O+M}$	41	19 – 88	45	19 – 107	2614	1324 – 5160
$x_{CO+M \leftrightarrow C+O+M}$	1	0.20 – 5.0	1	0.18 – 5.2	1	0.23 – 4.4
$x_{CO_2+M \leftrightarrow CO+O+M}$	28	25 – 32	28	24 – 32	1[1]	0.20 – 2.8
$x_{CO+O \leftrightarrow C+O_2}$	1	0.24 – 3.9	1	0.24 – 4.3	1[1]	0.14 – 2.8
$x_{CO_2+O \leftrightarrow CO+O_2}$	0.14	0.03 – 0.63	0.14	0.03 – 0.74	4.1	3.6 – 4.7

[1] The exact values of the means of these reactions rates are different from 1. However, it appears that the same agreement is achieved with whether an increase or a decrease of these rates, as shown by the extremal values. Thus, the nominal rates should be conserved. Furthermore, the simulation score

Table 5-3 : Closest modifications from the nominal simulation while preserving an acceptable agreement between the CO_2 density predictions and the measurement.

Model / Reaction	Park		Johnston		Cruden	
	mean	min – max	mean	min – max	mean	min – max
$x_{O_2+M \leftrightarrow O+O+M}$	2.7	2.0 – 3.7	2.1	1.4 – 3.0	77	68 – 88
$x_{CO+M \leftrightarrow C+O+M}$	1	0.50 – 2.2	1	0.52 – 2.1	1	0.45 – 2.36
$x_{CO_2+M \leftrightarrow CO+O+M}$	9.7	8.4 – 11.2	9.8	7.5 – 12.9	10.1	9.1 – 11.1
$x_{CO+O \leftrightarrow C+O_2}$	1	0.48 – 2.3	1	0.52 – 2.1	1	0.64 – 1.5
$x_{CO_2+O \leftrightarrow CO+O_2}$	1[1]	0.34 – 1.4	1[1]	0.32 – 1.23	1	0.62 – 1.6

of the updated simulations is still within 5% of the minimal score achieved. The exact value of the mean can still be retrieved by taking the geometric mean of the min and max values.

Chapter 6 : Chemical non-equilibrium studies in a N_2/Ar mixture

6.1 Background and Context

The work presented in this chapter built upon prior work by Gessman and Laux looking at experimental and numerical studies of a recombining nitrogen plasma (Gessman 2000, Laux, Gessman et al. 2001, Laux, Pierrot et al. 2012). For their work, these authors looked at the evolution of an initially equilibrium plasma as it was driven out of chemical equilibrium. Their experimental measurements used the same recombination tube setup as presented in Chapter 5 (see Figure 5.2) and targeted air, air/Ar, and N_2/Ar mixtures. As before, the centerline temperature of the plasma was $\sim 7\,000\,K$ and the plasma was in thermochemical equilibrium at the torch exit. The temperature dropped rapidly upon transiting the water-cooled tube at high speed, provoking chemical recombination. The gas temperature was measured using emission spectroscopy. At high temperatures (e.g. for short recombination tube lengths), the absolute intensity of atomic lines was used to measure the gas temperature (Laux, Pierrot et al. 2012) as described in (Laux 1993). At lower temperatures, emission from atomic lines was not strong enough and the rotational temperature of the $N_2^+(B)$ state was measured (Laux, Gessman et al. 2001). In both cases, the measured temperature was assumed to be equal to the gas temperature.

Gessman and Laux found that, whereas the air mixture remained in equilibrium during its transit of the recombination tube, the air/Ar and N_2/Ar mixtures did not. For these nonequilibrium cases, they observed non-boltzmann vibrational population distributions in the excited *B* state of molecular nitrogen by performing optical emission spectroscopy measurements of the nitrogen first positive system (Laux, Pierrot et al. 2012). These results were used to infer the atomic nitrogen density and show that atomic nitrogen is highly overpopulated with respect to its equilibrium value. Computational fluid dynamic (CFD) calculations were performed and the results compared with the measurements (Nagulapally, Kolman et al. 1998). In all cases, including the equilibrium test cases, the CFD calculations failed to predict the experimental measurements. For example, measurements indicated a centerline temperature drop of $1\,000\,K$ (from $7\,200\,K$ to $6\,200\,K$) for the air mixture test case which remains in equilibrium. CFD calculations predicted a temperature drop of only $200\,K$ (see Fig. 10 of (Nagulapally, Kolman et al. 1998)). This discrepancy led us to reconsider the assumptions made concerning the gas temperature measurements.

In cases where the absolute intensity of atomic lines is used to measure temperature, the analysis assumes that the electronic temperature of the atoms is equal to the gas kinetic temperature. In cases where the rotational temperature of the $N_2^+(B)$ is measured, the rotational temperature was assumed equal to the gas temperature. However, as discussed by Bruggeman (Bruggeman, Sadeghi et al. 2014), it is common to encounter cases where temperatures measured using emission spectroscopy are not necessarily equal to the gas temperature and therefore care needs to be taken when making such hypothesis. The goal of the work presented in this chapter was therefore to reexamine the measurement of gas temperature.

To address our goal, we proposed an alternate measurement of gas temperature using the spontaneous Raman scattering laser diagnostic. Spontaneous Raman scattering relies upon the inelastic scattering of photons from molecules (Eckbreth). A monochromatic laser is focused down to a point of interest and the spectral profile of inelastic Raman scattering is measured using a spectrometer. The spectral profile depends upon known Raman scattering cross-sections and on the rovibrational temperature of the targeted molecule. The measured spectra can thus be analyzed and used to determine the rovibrational temperature. Here we targeted molecular nitrogen and were thus measuring the rovibrational temperature of the molecular nitrogen ground electronic state. Because Raman scattering targets the ground electronic state, the rovibrational temperature can reasonably be expected to be equal to the gas temperature. Furthermore, the signal is not susceptible to quenching, making temperature estimates quite easy. It was for these reasons that we chose spontaneous Raman scattering technique.

The main drawback of spontaneous Raman scattering is that the signal is very weak. The signal level even from atmospheric pressure nitrogen is already small in contrast to the Rayleigh scattering signal. Furthermore, the signal scales linearly with density. Given that the torch is at a fixed pressure ($1\ atm$), the high temperatures imply low density and thus a small signal level. Indeed, the signal levels we encountered in our measurements within the plasma torch were quite low. A large amount of signal averaging was required to reduce the experimental uncertainty to the point where a reasonable temperature estimate could be made. Typical signal collection times were on the order of ~ 8 minutes per spectrum within the torch.

My coauthors on this work were Christophe Laux and Augustin Tibère-Inglesse. Augustin conducted this work as a PhD student, with Christophe as his thesis director and myself as a co-supervisor. Therefore, a portion of the results presented here was taken from Augustin's doctoral thesis.

6.2 Experimental setup

For the experiments presented here, a 1 cm diameter exit nozzle was used with the plasma torch. Calibrated flow meters were used to control the mass flow rate of each gas through the system. Several mixtures were studied. The measurements presented here were taken from(McGuire, Tibère-Inglesse et al. 2017), where a N_2/Ar mixture was used. The flowrate was $1.5\ g/s$ (50 slpm) for argon and $1.9\ g/s$ (90 slpm) for N_2. 75% of the argon was injected via the swirl injectors and 25% via the axial injectors. All of the N_2 was injected through the radial injectors. Directly at the exit of the torch, which corresponds to the inlet of the water-cooled test-section, temperature measurements could be obtained by measuring the absolute emission from lines of atomic nitrogen and argon as described in (Laux 1993).

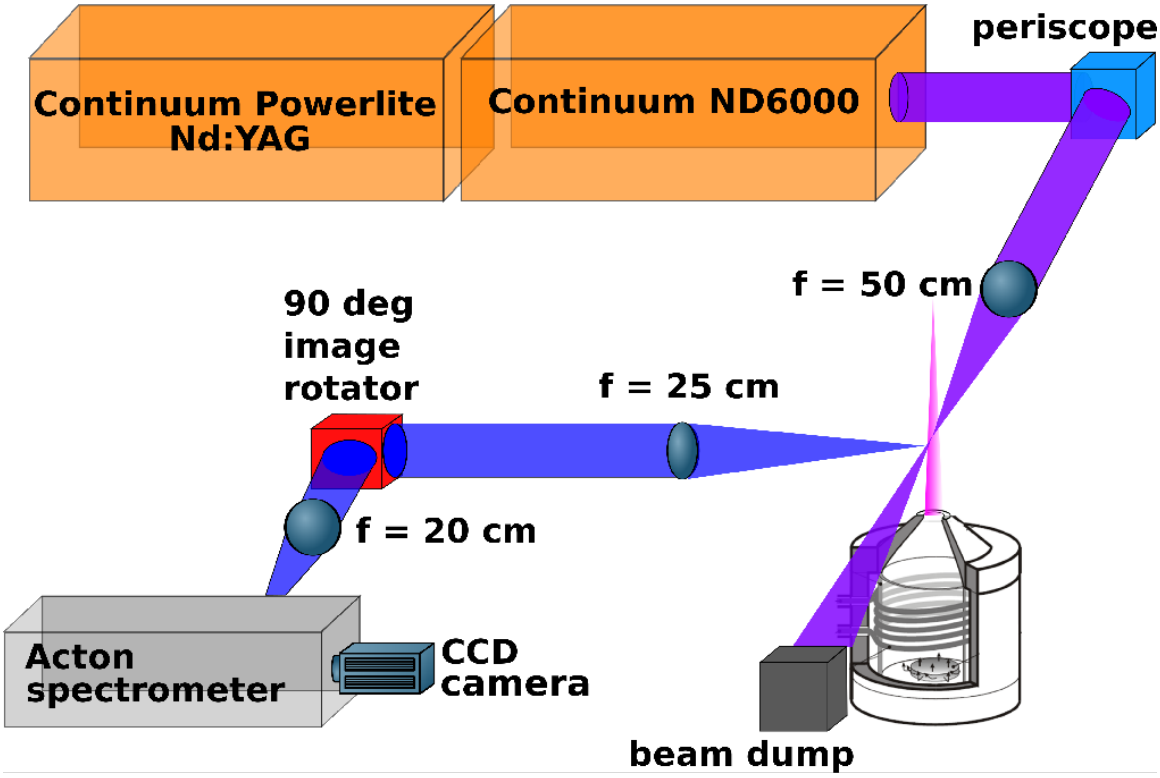

Figure 6.1: Experimental setup for Raman scattering measurements. The periscope consists of two quartz prisms for adjusting the height and direction of the laser beam.

For Raman measurements, a frequency doubled continuum dye laser was used to generate a 10 ns, 30 mJ ultraviolet pulse at 281 nm. Rhodamine 590 dye was used to supply a laser beam at 562 nm which was then frequency doubled to produce the final output at 281 nm. While the quadrupled output of a Nd:YAG laser at 266 nm may have sufficed for the measurements, the ability to tune the dye laser offered the ability to avoid potential laser-

induced interferences in the UV. The wavelength used for these measurements, namely 281 nm, represented a compromise between avoiding laser-induced interferences and maximizing laser power. The laser output at 281 nm was focused onto the exit of the torch at the point of interest via a 50 cm CaF_2 lens (Figure 6.1). The laser was polarized vertically and scattered light was collected at a right angle to the laser propagation axis. For imaging, two quartz lenses were used in conjunction with a 90° image rotator in order to image the spectrometer slit parallel to the laser axis (Figure 6.2). The optical magnification from measurement point to camera was approximately 0.8. The spectrometer was a Princeton Instruments SP500 spectrometer with a UV enhanced Princeton Instruments PI-MAX 1 intensified camera mounted at the exit port. The grating was blazed at 240 nm and has 2400 grooves mm^{-1}. Slit widths between 100 and 300 μm were used for experiments.

The instrumental function was determined by measuring the Rayleigh scattering profile centered on the laser wavelength. For every Raman measurement, a corresponding Rayleigh line profile was measured to determine the instrumental broadening. Figure 6.3 shows a measured Rayleigh scattering profile obtained for a slit width of 100 μm. The choice of slit depended on signal-to-noise ratio considerations: smaller slit widths result in less signal but higher resolution spectra for more accurate determination of temperature. Though the measured instrumental functions are not trapezoidal, it is convenient for the theoretical discussion that follows to approximate them as trapezoidal and to find the equivalent FWHM. In our setup, a slit width of 100 μm corresponds approximately to a trapezoidal instrumental function with a FWHM of 0.04 nm. Slit widths of 200 μm and 300 μm correspond to trapezoidal instrumental functions with FWHM of 0.08 and 0.10nm, respectively. Note that these trapezoidal instrumental functions are not used in the final analysis of the experimental data: rather, in the analysis we use the exact instrumental function determined from the measured Rayleigh signal.

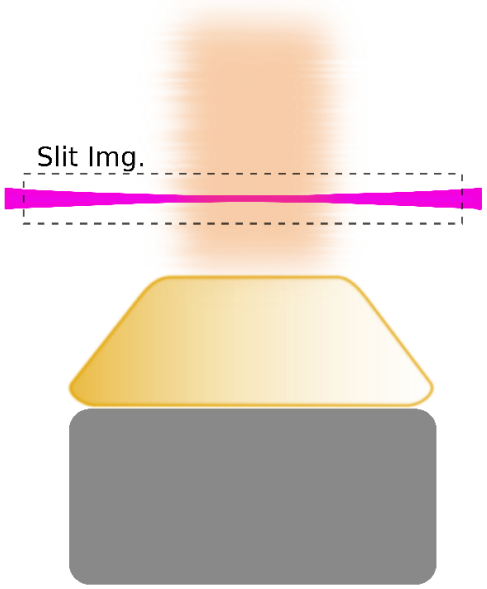

Figure 6.2: Relative positions of the laser focus, imaged spectrometer slit and torch nozzle. The laser is focused approximately 5 mm above the torch nozzle exit.

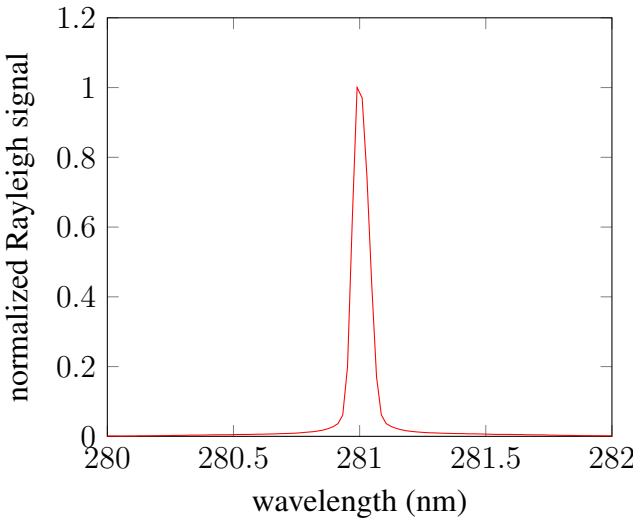

Figure 6.3: Normalized Rayleigh spectrum obtained for a spectrometer slit width of 100 µm. This spectrum was taken in ambient air (300 K, 1 atm).

For imaging the scattered light, the PI-MAX camera was used in gate mode (gate width of 20 ns) with maximum intensifier gain. Measurements were taken over a 4 mm spatial window and pixel binning was used to produce a measured spectrum. Spectral collection could be accomplished by varying the number of accumulations on CCD, by simply averaging several spectra to reduce noise or by some combination of these two. Increasing the number of

accumulations on CCD resulted in an increase in signal, but also noise. Averaging individual spectra reduced the amount of noise but did not increase the signal. To maximize signal-to-noise, we found that averaging 50 individual spectra, each obtained by accumulating 100 images on the CCD yielded the best result. The total time to obtain a single spectrum was then approximately 8 min. Note that these measurements were not synchronized to the RF voltage/current used to generate the plasma in the ICP torch. The plasma properties at the torch exit were assumed to be steady. Minimal interference from laser-induced fluorescence and from torch emission was observed at wavelengths close to the Stokes signal, but were not observed to overlap the signal itself. This interference was attributed to the nitrogen second positive system and was observed only at the torch exit, which corresponds to the water-cooled tube inlet. No fluorescence was observed at the exit of the water-cooled tube. Background spectra were taken by blocking the laser and recording spectra. These background spectra were then subtracted from the signal obtained with the laser to produce a final Raman spectrum. Both anti-Stokes and Stokes signals were observed. However, only the Stokes signal was used for analysis because it was stronger and because the camera efficiency was better at the Stokes wavelength.

6.2.1 Raman spectrum modeling

For temperature measurements, the spectral profile of the Raman signal was fitted with a theoretical model. Only Q-branch rotational transitions ($\Delta J = 0$) were accounted for, as these are much stronger than the O- and S- rotational branches ($\Delta J = \pm 2$). Furthermore, for the Q-branch transitions, the anisotropy contribution was ignored as it is much weaker than the mean of the polarizability tensor. This removed any dependence of the Raman cross-section on rotational level. Given these assumptions, the relative intensity of the Stokes-shifted Raman transition at frequency $\omega_{laser} + \Delta\omega$ was taken to be:

$$I(\omega_{laser} + \Delta\omega) = N_{vJ}(v + 1) \qquad \textbf{6-1}$$

where v and J represent the vibrational and rotational quantum numbers of the initial state. $\Delta\omega$ is the Raman shift corresponding to $\Delta v = 1$ and $\Delta J = 0$. N_{vJ} is the fractional population of N_2 in the initial state corresponding to vibrational level v and rotational level J: this includes the relevant Boltzmann factor, rotational degeneracy and nuclear spin degeneracy for the particular state. Note the dependence on the vibrational level expressed by the factor $(v + 1)$ which arises from the Raman cross-section. After applying this equation across all populated levels of N_2, the resulting intensity profile was convolved with the appropriate instrumental function. As an input, the model accepts both vibrational and rotational temperatures. For

temperature analysis, both the theoretical and experimental spectra were normalized. A fitting routine then minimized the residual between the experimental and theoretical curves to produce a final estimate of the vibrational and rotational temperatures.

Figure 6.4 shows three normalized theoretical Raman spectra, one at $T_{vib} = T_{rot} = 300\ K$, a second at at $T_{vib} = T_{rot} = 3\,000\ K$ and another at at $T_{vib} = T_{rot} = 7\,000\ K$. The different vibrational transitions are highlighted in the figure and illustrate the dependence of the spectrum on vibrational temperature. The rotational temperature impacts the shape of each vibrational feature, and is thus also a parameter that can be inferred from the Raman spectrum. This provides an estimate of the translational temperature given the fast equi-libration between rotation and translation in ground state N_2 at atmospheric pressure(Laux, Spence et al. 2003).

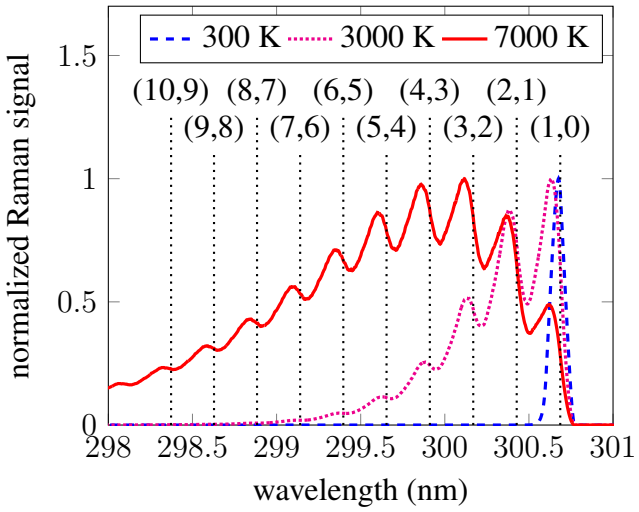

Figure 6.4: Modeled Raman spectra for $T_{vib} = T_{rot} = 300\ K$, $T_{vib} = T_{rot} = 3000\ K$ and $T_{vib} = T_{rot} = 7000\ K$. The instrumental function used here was triangular with FWHM = 0.08 nm, which closely approximates the instrumental function when using a slit width of 200 µm. Each spectrum has been normalized to its maximum. The vertical dotted lines and labels identify the various vibrational bands (v', v''), where v' and v'' represent the vibrational quantum numbers of the upper and lower states, respectively.

For density measurements, the absolute magnitude of the signal was measured relative to Raman scattering from room temperature air. The total area under the Raman spectrum depends linearly on the density, but also on the vibrational temperature. This temperature dependence is a result of the dependence of the scattered intensity on the vibrational level (Eqn. 6-1). The total area can thus be written as follows:

$$A = \frac{N_{N_2}}{N_{N_2}^{ref}} F(T, N_{N_2}^{ref}) \qquad \textbf{6-2}$$

where N_{N_2} is the total density of N_2. $F(T, N_{N_2}^{ref})$ represents the area under the Raman curve calculated at vibrational temperature T and at reference density $N_{N_2}^{ref}$. The A parameter was measured both in the plasma and in room temperature air. Then, by setting $N_{N_2}^{ref} = 1$, the ratio of these areas could be used to determine the density in the plasma as follows:

$$\frac{A_{plasma}}{A_{air}} = \frac{N_{plasma} F(T_{plasma}, 1)}{N_{air} F(T_{air}, 1)} \qquad \textbf{6-3}$$

where $T_{air} = 300\ K$ and N_{air}, the density of N_2 in ambient air, are known. T_{plasma} is determined from the theoretical fit to the normalized experimental spectra. N_{plasma} , the density of N_2 in the plasma, is the only remaining unknown in Eqn. 6-3 and can thus be determined directly.

Fitting routine and error analysis: For temperature measurements, a fitting routine was used to minimize the residual between the normalized experimental and theoretical spectra for various temperatures. Before fitting, any background offset was first subtracted and the experimental spectrum then normalized to its maximum value. Note that this maximum value includes the experimental noise intrinsic to the measurement. For low signal-to-noise situations, the normalization can be biased by this noise. To avoid this bias, an amplitude scaling factor was also varied within the fitting routine and used to scale the experimental spectra to obtain the best fit. The fitting residual is given by:

$$R = \frac{\sqrt{\sum_{\lambda_i} [E(\lambda_i) - T(\lambda_i)]^2}}{\sqrt{\sum_{\lambda_i} E(\lambda_i)^2}} \qquad \textbf{6-4}$$

where $T(\lambda_i)$ and $E(\lambda_i)$ denote the theoretical and experimental values of the spectrum at wavelength λ_i , respectively. This dimensionless residual represents the total error as a percentage of the total signal.

Under non-equilibrium conditions, there can exist a large uncertainty in vibrational and/or rotational temperature. To illustrate, a normalized theoretical curve was generated for $T_{vib} = T_{rot} = 3\,500\ K$. Next, the fitting routine was used to calculate the residual between this normalized spectrum and normalized spectra generated for various other combinations of T_{vib} and T_{rot}. For this test case, no artificial noise was added and thus the best fit is necessarily for $T_{vib} = T_{rot} = 3\,500\ K$ with $R = 0$. As illustrated in Figure 6.5, however, the residual can remain quite low along certain trajectories (black lines) in the domain defined by T_{vib} and T_{rot}

coordinates. This results in a large uncertainty. Where permissible due to signal-to-noise considerations, narrower spectrometer slit widths reduce the uncertainty and permit a more accurate determination of the vibrational and rotational temperatures. Note that under equilibrium conditions, the uncertainties are reduced because it is known that $T_{vib} = T_{rot} = T$ and the measurement is constrained.

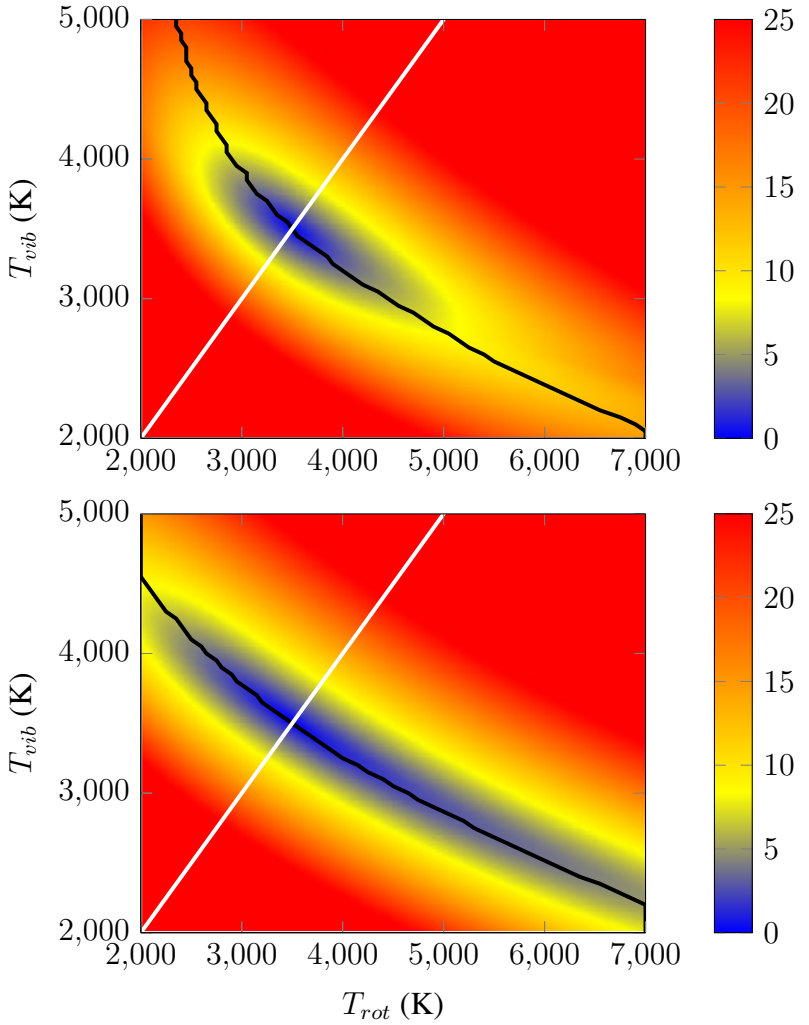

Figure 6.5: Residual contours (in %) showing the residual of a fit between a theoretical spectrum generated at (T_{rot}, T_{vib}) and a theoretical spectrum generated for $T_{vib} = T_{rot} = 3500\ K$. In all cases, the white line denotes equilibrium temperature coordinates $T_{vib} = T_{rot}$. For each rotational temperature, the black line denotes the corresponding vibrational temperature where the minimum residual was achieved. The absolute minimal residual is achieved for $T_{vib} = T_{rot} = 3500\ K$ as expected. Top: trapezoidal instrumental function with a FWHM of 0.04 nm, which corresponds to a spectrometer slit width of 100 µm. Bottom: trapezoidal instrumental function with a FWHM of 0.10 nm, which corresponds to a spectrometer slit width of 300 µm.

The minimum residual between experiment and theoretical spectra is denoted R_{min} and corresponds to the best estimate of (T_{vib} , T_{rot}). We assume that our model perfectly accounts for the experimental trends and that only Gaussian noise is present. The standard deviation of this Gaussian noise, σ, is estimated by taking the standard deviation over several camera pixels in regions where there is no signal. Given the residual defined in Eqn. 6-4 it is natural to then define a parameter R_m:

$$R_m = \frac{\sqrt{\sum_{\lambda_i} \delta_i^2}}{\sqrt{\sum_{\lambda_i} E(\lambda_i)^2}} \qquad \textbf{6-5}$$

where δ_i denotes the normally distributed error with standard deviation σ at the pixel corresponding to wavelength λ_i. This provides an estimate of the minimum residual that would be achieved for a perfect fit in the presence of pure Gaussian noise. In fact, we found that the minimum residuals achieved are only slightly higher than this value. Thus, the assumption of white Gaussian noise appears valid. In order to determine the uncertainty in the measurement, an estimate for residuals which correspond to a bad fit was needed. If indeed the error is well described by Gaussian noise and corresponds to a standard deviation σ then, for every pixel, 95% of the measured values will fall within $\pm 2\sigma$ of the true value. Given this, we defined a cutoff value for the residual as:

$$R_c = \frac{\sqrt{\sum_{\lambda_i} (2\sigma)^2}}{\sqrt{\sum_{\lambda_i} E(\lambda_i)^2}} = \frac{2\sigma\sqrt{N}}{\sqrt{\sum_{\lambda_i} E(\lambda_i)^2}} \qquad \textbf{6-6}$$

where N is the number of data points. This was used as the cutoff value between good and bad fits. All combinations of T_{vib} and T_{rot} for which $R < R_c$ were considered acceptable.

6.3 Results

6.3.1 Measurements of N_2 rovibrational temperature

Measurements at the exit of the torch: Raman measurements of temperature and density were first performed directly at the exit of the torch, which corresponds to the inlet of the water-cooled test section. The Raman measurements correspond to an average over a spatial window of approximately 4 mm centered on the nozzle axis. The high temperature and low gas

density resulted in a relatively low signal-to-noise ratio for the measurement. This prohibited measurements from being made at the narrowest spectrometer slit width, which in turn reduced the sensitivity of the measurement to temperature. The residual contour shown in Figure 6.6 illustrates the uncertainty in the measurement. Assuming equilibrium conditions ($T_{vib} = T_{rot}$), the best fit resulted in a temperature of $6\,600 \pm 1\,000\,K$. This best fit is shown in Figure 6.6. The measured temperature, along with Eqn. 6-3 and the corresponding Raman spectrum taken in room temperature air, can be used to estimate the density of molecular nitrogen. This yielded a value of about $4.2(\pm 1.1) \times 10^{17}\ cm^{-3}$, corresponding to a nitrogen mole fraction of 0.4 ± 0.1. At a temperature of $6\,600 \pm 1\,000\,K$, given the injection mixture of N_2 and Ar, the equilibrium density of N_2 corresponds to $4.0(\pm 3.5) \times 10^{17}\ cm^{-3}$. At a temperature of $6\,600\,K$, the equilibrium density corresponds to a mole fraction for molecular nitrogen of 0.36.

Spatially resolved measurements of temperature were also obtained by measuring the absolute emission of atomic nitrogen and argon lines. The measured temperature profiles are shown in Figure 6.7 and are compared with the Raman measurements. To within the uncertainty of both measurements, they are in agreement with one another. Thus, despite the relatively large uncertainty in the Raman measurement, this confirms the assumption of thermal and chemical equilibrium at the torch exit.

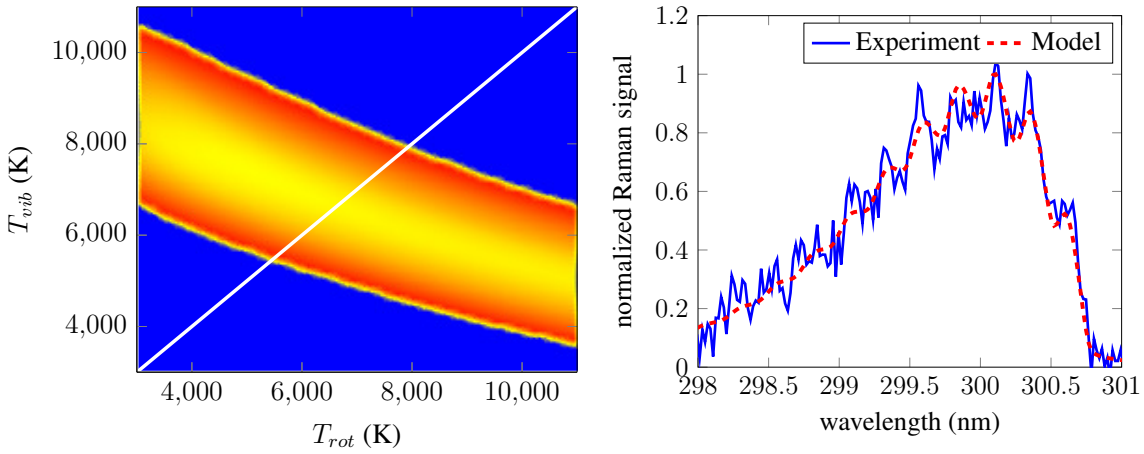

Figure 6.6: (left) Residual of various fits to the experimental spectrum obtained at the torch exit. The color indicates the goodness of the fit: yellow corresponds to the best fits and red to the worse fits. Only the residuals of acceptable fits are shown: fits outside the acceptable window are colored blue. This contour surface represents the range of uncertainty in the measurement. The white line indicates the equilibrium coordinates $T_{vib} = T_{rot}$. (right) Best fit achieved under equilibrium assumption for $T_{vib} = T_{rot} = 6\,600\,K$.

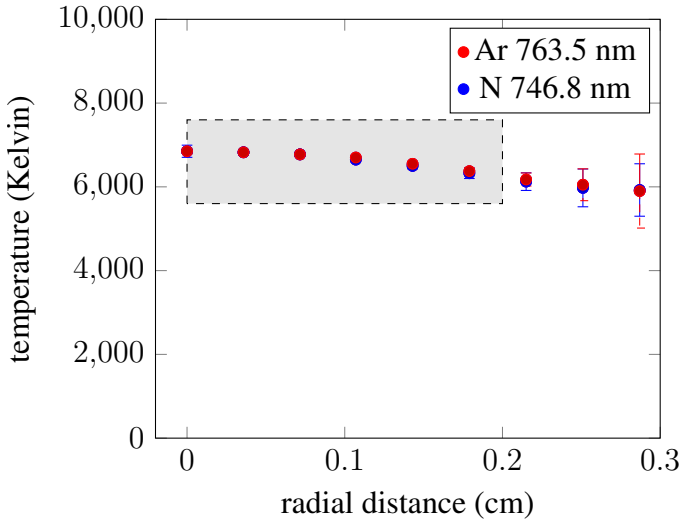

Figure 6.7: Temperature profile measured directly at the torch exit via absolute emission of the atomic N transition at 746 nm ($^4S^o - {}^4P$) and the atomic Ar transition at 764 nm ($^2[3/2] - {}^2[3/2]^o$). The Raman spectroscopy measure- ment of temperature is represented by the highlighted gray region. The horizontal width of this gray box represents the spatial window over which the Raman measurement was taken. The vertical height of the box represents the uncertainty in the Raman measurement. Note the extent of the radial axis: the nozzle perimeter is located at $r = 0.5\ cm$.

Measurements at exit of water-cooled tube: Raman measurements of temperature and density were also first performed at the exit of the $15\ cm$ water-cooled brass tube. As before, they correspond to an average over a spatial window of approximately 4 mm centered on the nozzle axis. Here, because the gas density is higher, the signal-to-noise was much better and a slit width of 100 µm (approximately 0.04 nm FWHM slit function) was used. This resulted in higher spectral resolution and an increased sensitivity to the vibrational and rotational temperatures.

As at the exit of the torch, the residual contour is centered on equilibrium temperature coordinates ($T_{vib} = T_{rot}$) suggesting that these degrees of freedom are equilibrated (Figure 6.8). If it is assumed that $T_{vib} = T_{rot}$, the best fit temperature occurs for $T = 3\ 300 \pm 100\ K$: this fit is shown in Figure 6.8. The measured density is estimated at $1.4(\pm 0.3) \times 10^{18}\ cm^{-3}$, which corresponds to a mole fraction of 0.6 ± 0.1 at a temperature of $3\ 300\ K$. At $3\ 300 \pm 100\ K$, the equilibrium nitrogen density is $1.43(\pm 0.05) \times 10^{18}\ cm^{-3}$. At $3\ 300\ K$, the equilibrium mole fraction is 0.64. Note that atomic emission cannot be used for measurements of temperature at the exit of the 15 cm tube. Not only is the emission of atomic lines here too

weak to measure, but these measurements rely on an assumption of full thermochemical equilibrium. The plasma at the exit of the 15 cm tube has been previously demonstrated to be out of equilibrium so this approach is no longer valid (Laux, Pierrot et al. 2012).

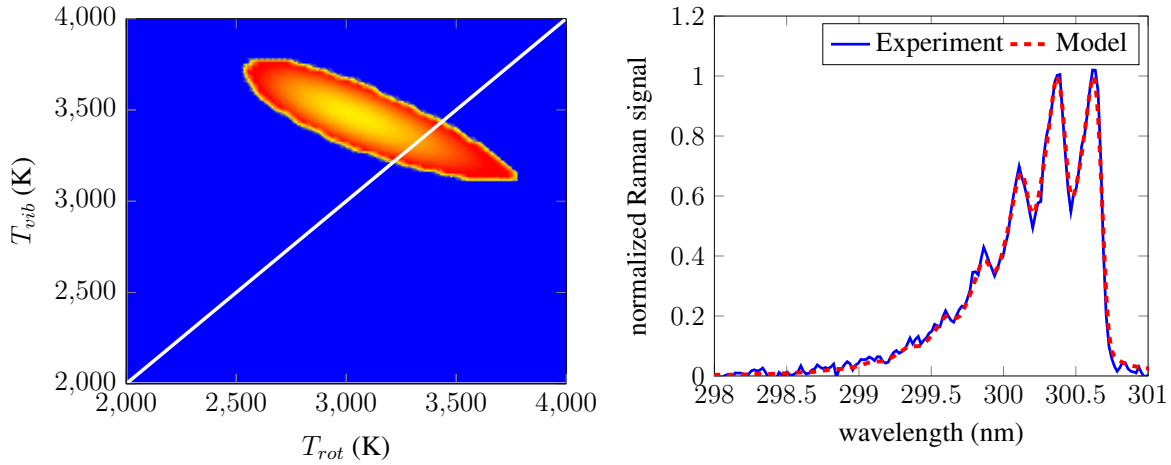

Figure 6.8: (left) Residual of various fits to the experimental spectrum obtained at the exit of the water-cooled brass tube. The color indicates the goodness of the fit: yellow corresponds to the best fits and red to the worse fits. Only the residuals of acceptable fits are included: fits outside the acceptable window are colored blue. As with Figure 6.6, this contour surface represents the range of uncertainty in the measurement. The best fit temperature was achieved for $T_{vib} = 3\,475\,K$ and $T_{rot} = 3\,000\,K$. The white line indicates the equilibrium coordinates $T_{vib} = T_{rot}$. (right) Best fit achieved (under equilibrium assumption) between experimental spectra obtained at exit of water-cooled brass tube and the model corresponding to $T_{vib} = T_{rot} = 3\,300\,K$.

Rayleigh scattering measurements: A separate measure of temperature at the exit of the 15 cm water-cooled tube was desired for verification. For this, Rayleigh scattering was used to measure the total gas density. This total gas density, together with the known gas pressure of 1 atm, could be used to estimate the temperature via the gas equation of state. For a single temperature estimate, two Rayleigh scattering measurements were taken. The first one was taken at the exit of the 15cm water-cooled tube. A second one was also taken at the exit of the 15 cm water-cooled tube but with the plasma torch turned off, providing a reference Rayleigh measurement at a temperature of 300 K in the N_2/Ar gas mixture. Given the known gas pressure of 1 atm, the ratio of these two measurements could be converted to a temperature estimate through the gas equation of state. The measurements were performed at the exact same location and under the same conditions as the Raman measurements at the exit of the 15 cm water-cooled tube. A laser wavelength of 281 nm was used and the laser was polarized vertically as with the Raman measurements. Scattered light was collected at a

ninety degree collection angle from the laser propagation axis. The Rayleigh scattered signal was assumed to come solely from atomic argon and molecular nitrogen:

$$I_{RL} = \eta V I_L n_0 (\chi_{N2}\sigma_{N2} + \chi_{Ar}\sigma_{Ar}) \qquad \textbf{6-7}$$

where I_{RL} corresponds to the intensity of the Rayleigh scattered light, η represents a collection efficiency factor for the optical collection system, V represents the collection volume for Rayleigh scattering, I_L the intensity of the laser at the collection point and n_0 the total gas density at the collection point (Richard, Walter et al. 2001). σ_{N2} and σ_{Ar} represent the right-angle Rayleigh scattering cross-section at the laser wavelength for molecular nitrogen and argon respectively. Note that the cross-sections σ_{N2} and σ_{Ar} are unknown at the laser wavelength. Limbach et al (Limbach, Dumitrache et al. 2016) report cross sections for various species, including N_2, N, Ar as well as their respective ions, at a laser wavelength of 532 nm. The values for N, N+ and Ar+ are comparable to those of N_2 and Ar. Though we see strong evidence of chemical non-equilibrium as documented in Laux et al(Laux, Pierrot et al. 2012), the total densities of these species are still estimated to be significantly lower than those of N_2 and Ar under our conditions. Therefore, the assumption that the Rayleigh scattering signal comes solely from atomic argon and molecular nitrogen was viewed as reasonable. Furthermore, σ_{Ar} does not depend on the gas temperature and σ_{N2} changes by less than a few percent below $7\,000\ K$ (Limbach, Dumitrache et al. 2016).

If I_{plasma} denotes the Rayleigh measurement with the torch ignited and $I_{ambient}$ denotes the Rayleigh measurement in the ambient gas mixture at 300 K, the ratio of these two signals yields:

$$\frac{I_{plasma}}{I_{ambient}} = \frac{n_{plasma}}{n_{ambient}} \frac{(\chi_{N2}\sigma_{N2} + \chi_{Ar}\sigma_{Ar})_{plasma}}{(\chi_{N2}\sigma_{N2} + \chi_{Ar}\sigma_{Ar})_{ambient}}$$
$$= \frac{T_{ambient}}{T_{plasma}} \frac{(\chi_{N2}\sigma_{N2} + \chi_{Ar}\sigma_{Ar})_{plasma}}{(\chi_{N2}\sigma_{N2} + \chi_{Ar}\sigma_{Ar})_{ambient}} \qquad \textbf{6-8}$$

where n_{plasma} and $n_{ambient}$ represent the total gas density with the torch ignited and in the ambient mixture, respectively. T_{plasma} and $T_{ambient}$ represent the temperature with the torch ignited and in the ambient mixture, respectively. The values in parentheses depend upon temperature and the subscripts '*plasma*' and '*ambient*' on these terms denote these values in the plasma and ambient mixture, respectively. The hypothesis that the chemical composition of the gas is approximately equal to that of the ambient mixture, and that the temperature dependence of the cross-section is negligible, removes any temperature dependence from the terms in parentheses in Equation 6-8. It follows that $I_{plasma}/I_{ambient} = T_{ambient}/T_{plasma}$.

For the measured Rayleigh scattered intensity, we integrated across the total line profile to obtain values for I_{plasma} and $I_{ambient}$. These measurements and the corresponding density estimates, yield a gas temperature estimate of $3\,100 \pm 100\,K$. Because Rayleigh cross-section data are typically reported at 532 nm, the use of a 281 nm wavelength for Rayleigh scattering measurements is not optimal, but this wavelength was more easily accessible in our experimental setup and still provided measurements in good agreement with the Raman measurements. As a verification step, similar measurements were done in the visible at the fundamental wavelength of the dye laser ($\lambda = 532\,nm$). Here, the cross-sections for $\lambda = 532\,nm$ reported by Limbach et al (Limbach, Dumitrache et al. 2016) were used along with equilibrium mole fraction calculations for N, N_2 and Ar species as a function of temperature. This was done to account for any potentially significant variations in the Rayleigh cross-section or mole fractions. These calculations, when compared with the experimental data taken at $\lambda = 562\,nm$, returned the same estimate of temperature.

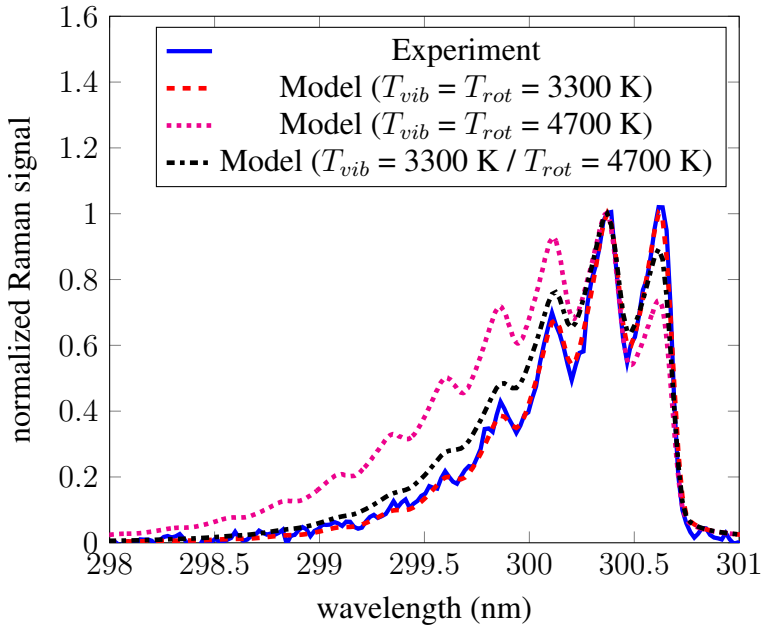

Figure 6.9: Same spectra as shown in figure 11 but with a theoretical spectrum calculated for $T_{vib} = T_{rot} = 4\,700\,K$ and a theoretical spectrum calculated for $T_{vib} = 3\,300\,K$ / $T_{rot} = 4\,700$ added for comparison. All plots are normalized to their maximum value.

Comparison with prior measurements: In the initial measurements of Gessman *et al* and Laux *et al*, they reported a measured temperature of $7\,200 \pm 100\,K$ at the water-cooled tube inlet(Gessman, Laux et al. 1997, Gessman 2000, Laux, Pierrot et al. 2012). Our measurements, from both emission using atomic nitrogen and argon and by the Raman scattering profile, indicate a slightly lower centerline temperature of about $6\,800 \pm 100\,K$

(Figure 6.7). The slight discrepancy may be due to differences in the torch power or gas injection procedure used. Because some of the RF torch components were modified since the original experiments of Gessman et al, it was not possible to reproduce the exact same injection scheme. However, the emission measurements show that the two conditions are reasonably close.

At the exit of the 15 cm water-cooled brass tube, Laux et al (Laux, Gessman et al. 2001) report rotational temperature measurements of $4\,715 \pm 100\,K$. These were measured by fitting rotational lines of the N_2^+ first negative system. We repeated these emission measurements and found essentially the same results – see(Tibère-Inglesse 2019). Namely, we obtained a comparable estimate of the rotational temperature and observed similar non-equilibrium distributions in the N_2 B and C electronic states as reported in(Gessman, Laux et al. 1997, Gessman 2000, Laux, Pierrot et al. 2012). This served as another indicator that, while the operating conditions used were slightly different than those of Gessman *et al* and Laux *et al*, the essential characteristics of their experiment were reproduced. The Raman measurements presented in this paper offer a new perspective on this recombining plasma by targeting the nitrogen ground state. They supply a measure of the vibrational temperature, previously unavailable by emission measurements, in addition to measures of rotational temperature and density. These results show that $T_{vib} = T_{rot} = 3\,300 \pm 100\,K$. Figure 6.9 shows a comparison between the measured Raman spectrum, a theoretical Raman spectrum calculated for $T_{vib} = T_{rot} = 3\,300\,K$, a theoretical Raman spectrum calculated for $T_{vib} = T_{rot} = 4\,700\,K$ and a theoretical Raman spectrum calculated for $T_{vib} = 3\,300\,/\,T_{rot} = 4\,700\,K$ to illustrate that a temperature of $4\,700\,K$ cannot be explained by the experimental Raman measurements.

While the Rayleigh scattering measurements support the Raman measurements, the discrepancy between the emission measurements remains. Such discrepancies can arise when production and/or decay mechanisms are faster than rotational-translational relaxation(Bruggeman, Sadeghi et al. 2014). While the Raman measurements show that $T_{vib} = T_{rot}$, the measured distributions of the N_2 B and C states observed via emission spectroscopy suggest that these electronic and vibrational levels do not follow a Boltzmann distribution(Gessman, Laux et al. 1997, Gessman 2000, Laux, Pierrot et al. 2012). Furthermore, the electron density, measured via Stark-broadened hydrogen emission in (Gessman 2000), is much higher than the equilibrium values for both $4\,700$ and $3\,300\,K$. It was also shown in (Gessman 2000) that there is a significant overpopulation of N atoms at the exit of the 15 cm water-cooled tube. Any of these observed non-equilibrium phenomena could potentially perturb the rotational temperature measurements made via emission spectroscopy of the N_2^+ ion. Studer and Vervisch (Studer and Vervisch 2007) report similar discrepancies in rotational temperature between emission measurements of the first negative

system and Raman measurements. They argue that, as a recombining plasma, excited species such as $B\ ^2\Sigma_u^+$ state of N_2^+ that are produced via chemical reactions are rapidly depopulated and do not have time to equilibrate to the background rotational temperature of the gas. Bruggeman et al (Bruggeman, Sadeghi et al. 2014) give additional examples of scenarios in which OES measurements yield incorrect estimates of the gas rotational temperature.

6.3.2 Gas temperature measurements using the N_2 first and second positive emission bands

The difference between the temperature measurements obtained from N_2^+B molecular emission and Raman scattering from $N_2\ X$ meant that we had two disparate measurements of temperature. For the reasons discussed in Section 6.1, it was felt that the Raman scattering temperature measurement should be closest to the gas translational temperature. However, as a final confirmation step, emission measurements of the molecular nitrogen first and second positive systems were conducted at high resolution to obtain two additional estimates of rotational temperature. Figure 6.10 – taken from (Tibère-Inglesse 2019) – shows the results obtained. The rotational temperature measurement from the N_2^+B state is, as expected, much higher than the Raman measurement. Meanwhile, the rotational temperature measurements from the N_2B and N_2C states agree with the Raman measurement. As discussed in (Tibère-Inglesse, McGuire et al. 2021), this is because N_2^+B is produced at an elevated temperature and does not thermalize before it is depopulated. The population mechanism could not be definitively identified but is believed to be a charge exchange reaction mechanism.

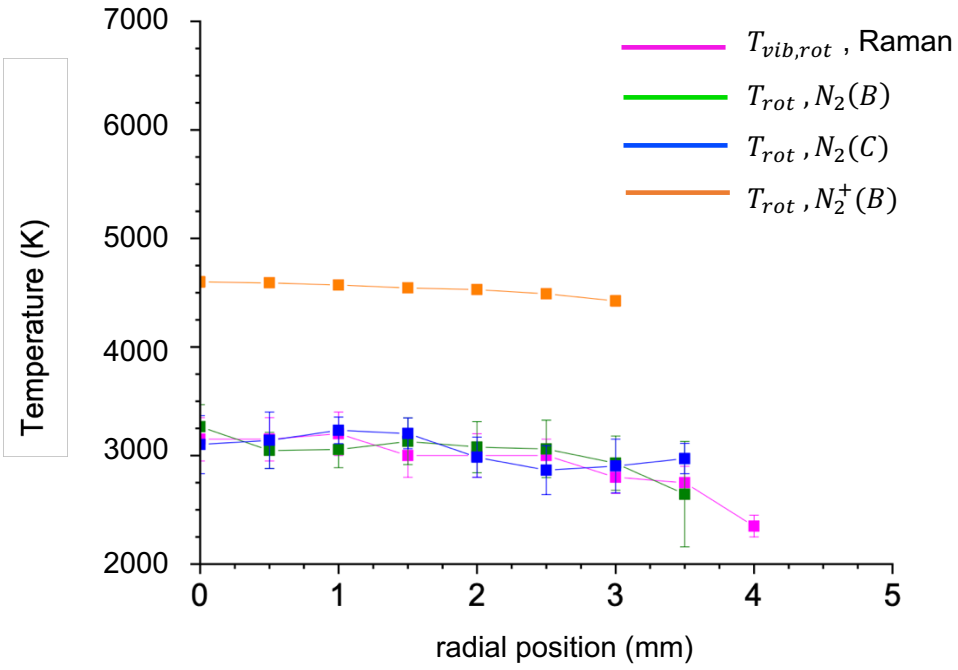

Figure 6.10 : Comparison of three separate measurements of temperature at the exit of the 15 cm recombination tube.

6.4 Perspectives

The work in this chapter showed that the rotational mode of the N_2^+B state is not thermally equilibrated. Prior measurements of gas temperature had assumed thermal equilibration and, therefore, provided an incorrect measurement of gas temperature. Raman scattering and emission measurements targeting the N_2B and N_2C states yielded an updated temperature measurement of $3\,300\,K$, which was much lower than the measured rotational temperature of $4\,700\,K$ associated with the N_2^+B state. An explanation for the elevated temperature of the N_2^+B state was published in (Tibère-Inglesse, McGuire et al. 2021). Furthermore, these results led to a follow-on publication wherein a simple model was developed to determine under what conditions the rotational temperature of a given molecular state can be considered to be equal to the gas translational temperature (Tibère-Inglesse, McGuire et al. 2023).

Unfortunately, and unexpectedly, the updated temperature measurements amplify the discrepancy with the CFD estimate of temperature. For the case studied here, CFD calculations estimate a temperature drop of roughly $\sim 300\,K$ between the entrance and exit of the 15-cm recombination tube. The updated temperature measurements show a temperature drop of $\sim 3\,700\,K$. Chapter 7 will present one ongoing project that might shed light on this problem. However, there is currently no explanation for this discrepancy.

Chapter 7 : Conclusion

My current research plans involve three areas of focus. The first is a continuation of my work in the field of atmospheric entry and involves the plasma torch. The second concerns a technology known as plasma methane pyrolysis, which is being actively pursued as a carbon neutral (or perhaps even a carbon negative) way of producing hydrogen as a clean source of hydrogen production. The third and final area is related to the study of laser plasma interactions leading to the emission of GHz and THz frequency radiation. Each of these areas will be presented in more detail in the following sections.

7.1 Atmospheric entry

Current research involving the plasma torch is being pursued via Cyrine Merhaben, who began her doctoral thesis in late 2022 and is now in her second year of doctoral studies. I obtained permission from the doctoral school to act as her thesis director without having an HDR. Christophe Laux is a co-director on the thesis. The thesis is funded by a grant from the SMEMAG doctoral school. Cyrine's thesis will continue the work presented in Chapter 5 and Chapter 6. Her work involves the recombination tube but targets a separate mixture relevant for space missions to Titan – a moon of Saturn. Titan's atmosphere is composed of $98\%\ N_2$ and $2\%\ CH_4$ by volume. Titan is of particular interest because of the planned NASA Dragonfly mission to Titan. The launch date is currently scheduled for 2028, with a landing on Titan several years later. (Wright, Herath et al. 2019) provides an overview of the Entry, Descent, and Landing (EDL) portion of the Dragonfly mission. To correctly predict the radiative heat load to the capsule surface, models must be able to accurately predict both CN concentration and excited state densities. Meanwhile, the flow field is not expected to be in equilibrium (Olejniczak, Prabhu et al.). The CN molecule is formed in concentrations higher than those associated with equilibrium and, furthermore, the population distribution of the CN electronic states is not expected to follow an equilibrium distribution (Bose, Wright et al. 2006). The goal of Cyrine's thesis is to provide experimental data associated with a recombining N_2/CH_4 flow to test against model predictions. There is a particular interest in measuring the electronic state population distribution within CN as this distribution is not expected to be in equilibrium at flight conditions.

The work presented in Chapters 5 – 6 has introduced additional questions that could potentially be subjects of future thesis work. Two interesting scientific questions involving the CO/CO_2 and air recombination studies will be addressed in the following paragraphs.

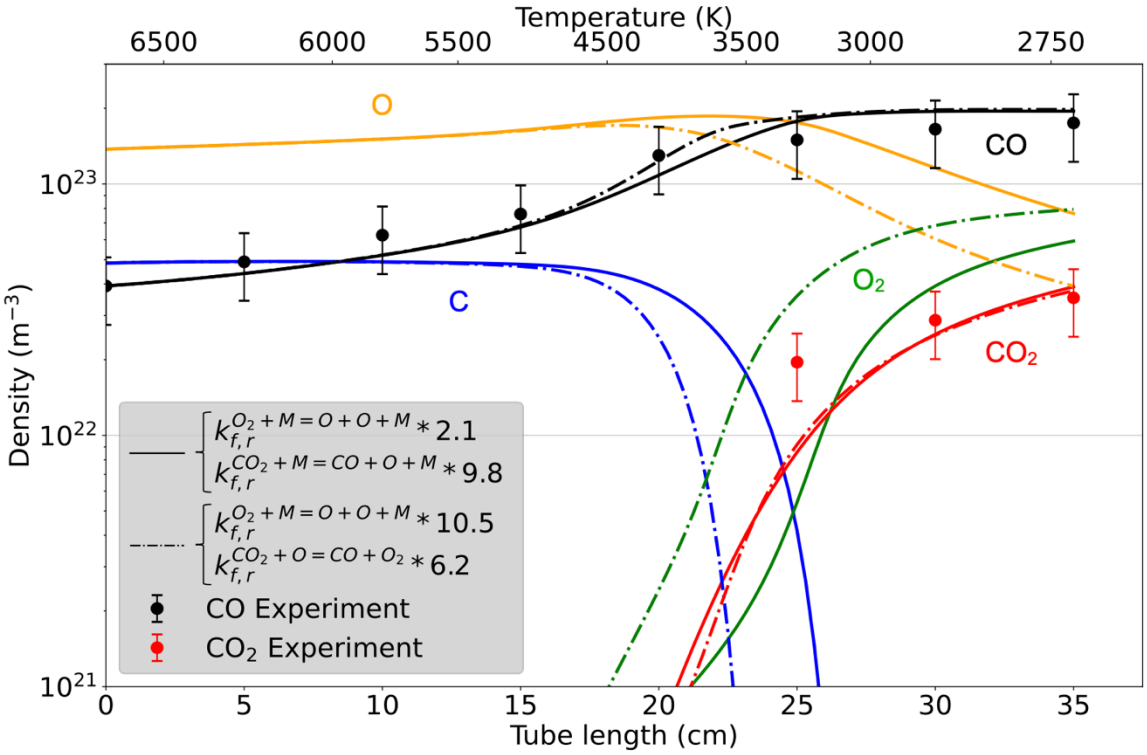

Figure 7.1: Two possible modifications of the Johnston model that give good agreement with the CO and CO_2 concentration measurements taken in the recombination tube.

CO recombination studies: Section 5.5 discussed possible variations in the baseline kinetic models that would allow for matching the experimental data obtained in the recombination tube. Some of these modifications were obtained by looking at which modifications gave the best possible agreement (see Table 5-2). These modifications were found to require rather large changes to the baseline kinetic models. However, Table 5-3 gives an alternate set of modifications which provide an acceptable level of agreement with the experimental data, yet which involve much smaller modifications to the baseline model rates. These solutions are of particular interest. Figure 7.1 shows two modifications presented in Table 5-3. These modifications were chosen because they are among the smallest possible modifications to the baseline model that give good agreement with the recombination tube measurements. It is interesting to note that, while both the modifications presented give very similar CO and CO_2 concentration profiles, the atomic oxygen and molecular oxygen profiles are very different. Neither of these species were targeted in the thesis of Corentin Grimaldi. A follow-on project,

conducted in collaboration with Mragank Singh of the University of Queensland, is looking to implement laser-induced fluorescence measurements of atomic oxygen density to evaluate if one of the modifications presented in Figure 7.1 provides good agreement with the measured atomic oxygen density.

Air recombination studies : The motivation for the work presented in Chapter 6 was the large discrepancy between CFD predictions and measurements of gas temperature at the exit of the recombination tube. Chapter 6 attempted to resolve this discrepancy by pursuing spontaneous Raman scattering measurements of temperature, as it was believed that the prior estimates of temperature did not yield an accurate estimate of bulk gas temperature. Indeed, this hypothesis proved to be correct – the prior Optical Emission Spectroscopy measurement of temperature did not yield a value representative of the bulk gas temperature. Unfortunately, the updated Raman measurements were even further away from the CFD predictions and thus the underlying question that motivated the work in Chapter 6 remains open. To address this open question, we are currently considering two categories of solutions which will be discussed in the following paragraphs.

The first category of solution looks to employ more advanced measurement techniques to have a better understanding of the actual recombining plasma dynamics. For example, all measurements to date have been time-averaged and yield no information on any unsteady phenomena that may be occurring in the flow. A collaboration is currently being pursued with ONERA as part of a LaSIPS collaborative grant. This collaboration is attempting to implement hybrid fs/ps coherent anti-Stokes Raman scattering (hybrid fs/ps CARS) measurements in the recombining plasma. It is hoped that such measurements will have significantly strong signal levels to permit single-shot measurements of temperature with “instantaneous” temporal resolution ($< 10\ ps$). If successful, such a measurement would enable us to track unsteady phenomena and see if such phenomena could be contributing to the discrepancy. Unsteady phenomena of potential interest include turbulence. A related follow-on project is looking to apply this same hybrid fs/ps CARS technique to study the temporal evolution of gas temperature within a nanosecond pulsed electric discharge, where measurements with good temporal resolution are required. Another measurement technique of potential interest is NO molecular tagging velocimetry, which provides a measure of gas velocity. Recent work by Jiang *et al* (Jiang, Hsu et al. 2024) has shown that long lived NO fluorescence can be excited using a $1 + 1$ REMPI scheme. NO is known to be present in the air-based mixtures used in the torch. To date, the gas velocity has never been directly measured in the plasma torch – it has only been inferred indirectly (see, for example, Section 5.4).

A second category of solution that we are pursuing involves altering and simplifying the experimental setup to such a degree that a reasonable level of agreement can be achieved between measurement and CFD predictions. The air plasma exits the torch with a temperature of $\sim 7\,000\,K$. Rather than passing this air directly into the recombining tube, one simplification would be to first pre-mix this hot air directly with cold air in such proportions as to lower the mixture temperature (e.g. $\sim 4\,000\,K$). Once this lower temperature has been established, the air mixture would then be injected into the recombination tube as before. Such a procedure would drastically lower the inlet temperature, and presumably lead at some point to good agreement with CFD calculations. Furthermore, the lower inlet temperature is variable – reducing the cold air mass fraction will continuously raise the inlet temperature. Therefore, once a benchmark agreement with CFD predictions is achieved, the inlet temperature can be easily raised in a continuous manner until discrepancies with CFD predictions start to appear. Such a procedure would allow us to get a more detailed view of the causes leading to the discrepancy.

7.2 Plasma methane pyrolysis

The national energy and climate plan of France aims to reduce emissions across several sectors (2020). Hydrogen is widely considered to be a promising clean alternative to conventional fossil fuel combustion (2017, 2020). However, although hydrogen combustion does not produce CO_2, many challenges stand in the way of achieving widespread clean hydrogen production. Today, more than 90% of hydrogen is produced using steam methane reforming, which emits ~11 tons of CO_2 per ton of hydrogen produced (2020). The main clean alternative - water electrolysis – requires a high electricity input of at least 40 kWh/kg H_2. A recent alternative is methane plasmalysis, wherein plasma converts methane directly into hydrogen H_2 and unoxidized solid carbon C(s) by-products. The solid carbon by-product can be easily separated from the gaseous hydrogen. Methane plasmalysis has zero CO_2 emissions, and in theory requires as little as 5 kWh/kg H_2.

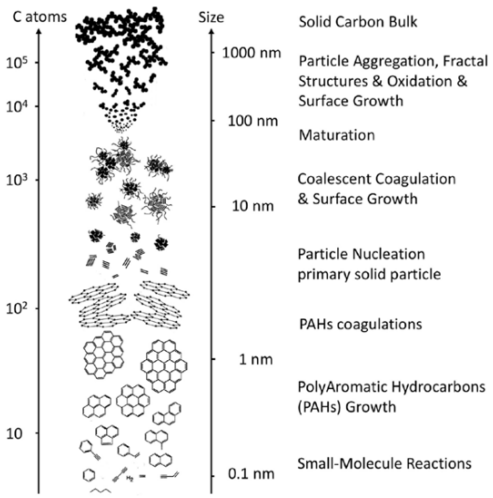

Figure 7.2 : Sequence of steps leading to C(s) formation in methane plasmalysis (source Ref (Gautier, Rohani et al. 2017)).

Plasmalysis is limited by slow reaction kinetics (Fincke, Anderson et al. 2002). While equilibrium diagrams show H_2 and C(s) as the dominant species when methane is heated to temperatures between 1000–2500 °C, methane does not directly decompose into these products. The formation of solid carbon soot begins with the formation of intermediate species: starting with methyl (CH_3), and followed by ethane (C_2H_6), ethylene (C_2H_4), and acetylene (C_2H_2). Benzene (C_6H_6) and polycyclic aromatic hydrocarbons (PAH) then form from these elements producing carbon soot particles (see Figure 7.2). The soot particle size increases via addition of hydrocarbon molecules, while the carbon purity increases due to dehydrogenation by reactions with atomic hydrogen. This process is rate-limited, and the finite-rate chemistry makes it difficult to reach the equilibrium composition of H_2 and C(s).

Accelerating the chemical kinetics generally involves heating the methane to high temperatures (> 1500 °C). Results from the research group of Laurent Fulcheri at MINES-ParisTech (Gautier, Rohani et al. 2017) have successfully demonstrated this technology and resulted in its implementation at an industrial scale (14 tons H_2/day) (https:// monolith - corp.com). The technology used by Monolith requires an estimated input of 20 kWh/kg H_2 using data in Ref. (Diab, Fulcheri et al. 2022) (half the energy for water electrolysis). To improve the efficiency further and get closer to the theoretical minimum of 5 kWh/kg H_2, it is necessary to limit the gas heating. This is possible by using non-thermal (or non-equilibrium) plasmas. However, maintaining a non-thermal plasma at the high pressures required for treating large volumes of gas is challenging. The startup SPARK Cleantech (http:// spark - cleantech.eu) has developed a novel approach to produce non-thermal plasmas at atmospheric pressure using Nanosecond Repetitively Pulsed (NRP) discharges. These discharges accelerate the chemical conversion to H_2 and C(s) at reduced temperatures (<

1500 °C). However, non-equilibrium kinetics in methane discharges are not well understood and this is impeding further optimization. The objective of this work is to provide a validated model capable of describing the electron-driven kinetics during the discharge as well as molecular growth and soot formation kinetics that occur at longer times.

At higher temperatures (> 1500 °C), the plasmalysis process follows the mechanism identified by Fincke *et al* and described above. At lower temperatures (20 – 120 °C), a different process involving polyyne molecules has been identified. The temperature range of interest that enables the best energy efficiency lies in between these two bounds and, as of now, a validated mechanism does not exist. Indeed, carbon nucleation reaction routes are sensitive to the gas temperature, pressure, and feed gas carbon content (Hassouni, Mohasseb et al. 2006, Tetard, Michau et al. 2022). The peculiar dynamics of NRP discharges in methane-based mixtures also lead to unique types of reactive species - i.e., atoms, radicals, and ions. This, along with the intermediate temperature level and the transient conditions that characterize the NRP afterglow, will probably result in a variety of currently unexplored molecular growth routes. Identifying these reaction routes is a key scientific challenge of this work.

To address these scientific objectives SPARK, LSPM, and laboratoire EM2C are pursuing a collaboration via an ANR PRCE grant. In addition, SPARK is financing 2 doctoral thesis (theses CIFRE) with laboratoire EM2C.

7.3 GHz/THz frequency generation

Femtosecond filaments occur when a high intensity ($> 10^{13}\ W/cm^2$) short pulse laser ($< 100\ fs$) generates a weakly ionized plasma via photoionization (Hercher 1964, Couairon and Mysyrowicz 2007). A detailed overview of femtosecond pulses is provided by Couairon and Mysyrowicz (Couairon and Mysyrowicz 2007). Defocusing of the optical beam occurs due to the filament ionization. This effect counters the tendency of the optical pulse to self-focus due to the nonlinear Kerr effect. The interplay between these two nonlinear propagation effects limits the intensity of the focused beam and the level of photoionization. Femtosecond filaments are therefore limited to electron densities of $n_e < 10^{18} cm^{-3}$ in air. An interesting phenomenon associated with femtosecond filaments is their emission of radiation in the GHz and THz frequency ranges (Figure 7.3) (Hamster 1993, Thiele, Nuter et al. 2016, Garrett, Elle et al. 2021). Emission in the THz frequency range was first observed by Hamster in the early 1990's (Hamster 1993, Hamster, Sullivan et al. 1993, Hamster, Sullivan et al. 1994) and generated significant interest due to the notable lack of practical emission sources in this frequency range – the so-called *THz gap*. The angular distribution of the THz emission is case

dependent, but generally occurs either in the forward or side directions (Hamster, Sullivan et al. 1994, Thiele, Nuter et al. 2016). Recent work has focused on the use of a 2-color optical field for generating THz emission as this produces a much larger THz signal compared to the 1-color mechanism studied by Hamster *et al* – Tailliez *et al* (Tailliez, Stathopulos et al. 2020) report conversion efficiencies on the order of 10^{-4} for the 2-color approach compared to efficiencies $< 10^{-8}$ for the 1-color approach reported by Sprangle *et al (Sprangle, Peñano et al. 2004)*.

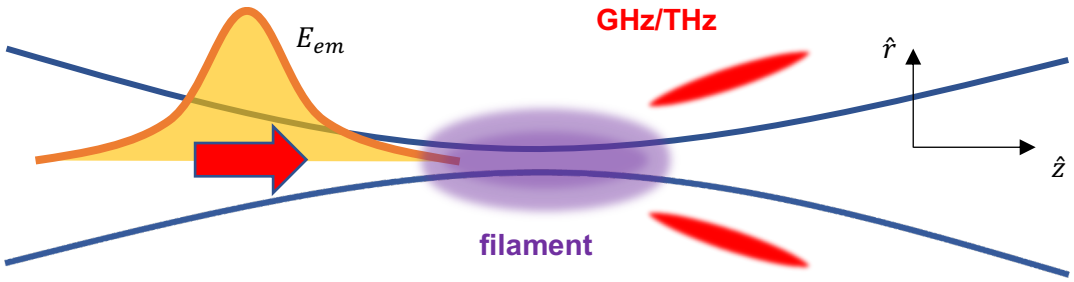

Figure 7.3 : Experimental configuration used for the generation of THz radiation. The direction of the emitted THz radiation depends upon the experimental parameters used but generally falls between the forward ($+\hat{z}$) and side directions.

The impact of nonlinear laser beam propagation (Kerr self-focusing and plasma defocusing) on the THz signal has received little attention in the literature. Sprangle *et al* perform numerical simulations of THz emission from a femtosecond filament using a 1-color optical pulse (Sprangle, Peñano et al. 2004), and account for nonlinear propagation affects using a *Source Dependent Expansion* method for modeling the evolution of the laser pulse. I am currently working with Mikhail Shneider of Princeton University to understand the impact of nonlinear propagation effects on the THz signal amplitude, frequency content, and angular emission profile. To that end, we propose a beam propagation model that is simple to implement and can be coupled to existing models for THz emission from femtosecond filaments published in the literature. We consider the 1-color *Transition-Cherenkov* THz emission mechanism identified in the literature (D'Amico, Houard et al. 2007, Amico, Houard et al. 2008, Thiele, Nuter et al. 2016), and introduce two models for this emission mechanism, each of which simulates both the current dynamics in the filament and the resulting THz emission due to the *Transition-Cherenkov* mechanism. These two models are adapted from existing models and differ in their level of complexity and capabilities. The first model is a 3D axisymmetric model adapted from the work of Thiele *et al (Thiele, Nuter et al. 2016)*. The second model is a simpler 1D model. Note that, while we limit ourselves to the 1-color Transition-Cherenkov mechanism,

the beam propagation model proposed here can be adapted for use with models of other THz emission mechanisms in femtosecond filaments – including the 2-color mechanism.

Both the 3D axisymmetric and 1D models for the current dynamics and emission are used in conjunction with the proposed beam propagation model to estimate the THz emission from a femtosecond filament. For the cases considered, we show that the numerical beam propagation model is necessary to accurately calculate the amplitude of the THz emission – though not necessarily its angular distribution or frequency content. While the 3D axisymmetric model of current dynamics and emission is admittedly more capable, the corresponding 1D model performs quite well and is much simpler to implement. These observations have practical implications for the estimation of THz emission signatures from femtosecond filaments.

References

(2017). R&D Opportunities for Development of Natural Gas Conversion Technologies, Argonne and Pacific Northwest National Laboratories.

(2020). Hydrogen strategy : enabling a low-carbon economy. U. S. D. o. Energy.

(2020) Integrated National Energy and Climate Plan for France. DOI: https://ec.europa.eu/energy/sites/ener/files/documents/fr_final_necp_main_en.pdf

(http:// spark -cleantech.eu). Spark Cleantech.

(https:// monolith -corp.com). Monolith Inc.

Allen, H. J. (1958). "Hypersonic Flight and the Re-Entry Problem." Journal of the Aeronautical Sciences: 217-227.

Allison, A. C., et al. (1971). "Absorption by vibrationally excited molecular oxygen in the Schumann-Runge continuum." Planetary and Space Science **19**(11): 1463-1473.

Amico, C. D., et al. (2008). "Forward THz radiation emission by femtosecond filamentation in gases: theory and experiment." New Journal of Physics **10**(1): 013015.

Amiot, C. (1982). "The infrared emission spectrum of NO: Analysis of the Δv = 3 sequence up to v = 22." Journal of Molecular Spectroscopy **94**(1): 150-172.

Amiot, C. and J. Verges (1982). "Fine Structure of the C2Π-A2Σ+ and D2Σ+-A2Σ+ Band Systems of the NO Molecule: Homogeneous and Heterogeneous Perturbations." Physica Scripta **25**(2): 302.

Anderson Jr., J. D. (2003). Modern Compressible Flow with Historical Perspective, McGraw-Hill.

Anderson Jr., J. D. (2006). Hypersonic and High-Temperature Gas Dynamics, American Institute of Aeronautics and Astronautics.

Bak, M. S., et al. (2015). "Nanosecond-pulsed discharge plasma splitting of carbon dioxide." IEEE Transactions on Plasma Science **43**(4): 1002-1007.

Bogaerts, A. and G. Centi (2020). "Plasma Technology for CO2 Conversion: A Personal Perspective on Prospects and Gaps." Frontiers in Energy Research **8**.

Bose, D., et al. (2006). "Modeling and Experimental Assessment of CN Radiation Behind a Strong Shock Wave." Journal of Thermophysics and Heat Transfer **20**(2): 220-230.

Brabbs, T. A. and F. E. Belles (1967). "Recombination of carbon monoxide and atomic oxygen at high temperatures." Symposium (International) on Combustion **11**(1): 125-135.

Bruggeman, P. J., et al. (2014). "Gas temperature determination from rotational lines in non-equilibrium plasmas: a review." Plasma Sources Science and Technology **23**(2): 023001.

Bruna, P. J. and J. S. Wright (1992). "Theoretical study of the transition probabilities of the doubly-excited states E1.SIGMA.g+ of C2 and 22.SIGMA.g+ of C2+." The Journal of Physical Chemistry **96**(4): 1630-1640.

Caillaut, L., et al. (2006). Modeling the spectral radiation of a methane/nitrogen plasma test case 4. **629**.

Centi, G. and S. Perathoner (2020). "Chemistry and energy beyond fossil fuels. A perspective view on the role of syngas from waste sources." Catalysis Today **342**: 4-12.

Chang, W. F., et al. (1993). "Absolute optical oscillator strengths for the photoabsorption of nitric oxide (5–30 eV) at high resolution." Chemical Physics **170**(1): 111-121.

Chantranupong, L., et al. (1992). "A configuration interaction study of the oscillator strengths for various low-lying transitions of the CO molecule." Chemical Physics **161**(3): 351-362.

Cheng, J., et al. (2018). "Spectral Study ofA1Π–X1Σ+Transitions of CO Relevant to Interstellar Clouds." The Astrophysical Journal **859**(1): 19.

Couairon, A. and A. Mysyrowicz (2007). "Femtosecond filamentation in transparent media." Physics Reports **441**(2): 47-189.

Cruden, B., et al. (2010). Absolute Radiation Measurement in High Mass Venus and Mars Entry Conditions. 10th AIAA/ASME Joint Thermophysics and Heat Transfer Conference, American Institute of Aeronautics and Astronautics.

Cruden, B. A., et al. (2018). Characterization of CO Thermochemistry in Incident Shockwaves. 2018 Joint Thermophysics and Heat Transfer Conference, American Institute of Aeronautics and Astronautics.

Cruden, B. A., et al. (2012). "Absolute Radiation Measurement in Venus and Mars Entry Conditions." Journal of Spacecraft and Rockets **49**(6): 1069-1079.

de Vivie, R. and S. D. Peyerimhoff (1988). "Theoretical spectroscopy of the NO radical. I. Potential curves and lifetimes of excited states." The Journal of Chemical Physics **89**(5): 3028-3043.

DeLeon, R. L. (1988). "CO (A--X) electric dipole transition moment." The Journal of Chemical Physics **89**(1): 20-24.

DeLeon, R. L. (1989). "Erratum: CO (A--X) electric dipole transition moment [J. Chem. Phys. 89, 20 (1988)]." The Journal of Chemical Physics **91**(9): 5859-5860.

Diab, J., et al. (2022). "Why turquoise hydrogen will Be a game changer for the energy transition." International Journal of Hydrogen Energy **47**(61): 25831-25848.

D'Amico, C., et al. (2007). "Conical Forward THz Emission from Femtosecond-Laser-Beam Filamentation in Air." Physical Review Letters **98**(23): 235002.

Ebrahim, N. A. and R. J. Sandeman (1976). "Interferometric studies of carbon dioxide dissociation in a free-piston shock tube." The Journal of Chemical Physics **65**(9): 3446-3453.

Eckbreth, A. Laser Diagnostics for Combustion Temperature and Species, Gordon and Breach.

Fairbairn, A. R. and A. G. Gaydon (1997). "The dissociation of carbon monoxide." Proceedings of the Royal Society of London. A. Mathematical and Physical Sciences **312**(1509): 207-227.

Field, R. W., et al. (1983). "Radiative decay rates from deperturbed v=0--7 vibrational levels of CO A$^1 \Pi$ measured using synchrotron radiation." The Journal of Chemical Physics **78**(6): 2838-2846.

Fincke, J. R., et al. (2002). "Plasma Pyrolysis of Methane to Hydrogen and Carbon Black." Industrial & Engineering Chemistry Research **41**(6): 1425-1435.

Fischer, C. F. (2006). "Some improved transition probabilities for neutral carbon." Journal of Physics B: Atomic, Molecular and Optical Physics **39**(9): 2159.

Fridman, A. (2008). Plasma Chemistry. New York, Cambridge University Press

Gallusser, R. and K. Dressler (1982). "Multistate vibronic coupling between the excited 2Π states of the NO molecule." The Journal of Chemical Physics **76**(9): 4311-4327.

Garrett, T., et al. (2021). "Generation of radio frequency radiation by femtosecond filaments." Physical Review E **104**(6): L063201.

Gautier, M., et al. (2017). "Direct decarbonization of methane by thermal plasma for the production of hydrogen and high value-added carbon black." International Journal of Hydrogen Energy **42**(47): 28140-28156.

Gessman, R., et al. (1997). Experimental study of kinetic mechanisms of recombining atmospheric pressure air plasmas. 28th Plasmadynamics and Lasers Conference, American Institute of Aeronautics and Astronautics.

Gessman, R. J. (2000). An experimental investigation of the effects of chemical ionizational nonequilibirum in recombining atmospheric pressure air plasmas. Mechanical Engineering Dept. Stanford, CA, Stanford University. **PhD**.

Griem, H. (1974). Spectral line broadening by plasmas, Academic Press.

Griem, H. R. (1997). Principles of Plasma Spectroscopy, Cambridge University Press.

Grimaldi, C. (2023). Experimental Study and Modeling of a Recombining CO2 Plasma. École doctorale Sciences Mécaniques et Energétiques Matériaux et Géosciences (SMEMAG), Université Paris-Saclay **2023**.

Hamster, H. (1993). Generation of Sub-Picosecond Terahertz Radiation by Laser Produced Plasmas. Physics, University of California, Berkeley.

Hamster, H., et al. (1994). "Short-pulse terahertz radiation from high-intensity-laser-produced plasmas." Physical Review E **49**(1): 671-677.

Hamster, H., et al. (1993). "Subpicosecond, electromagnetic pulses from intense laser-plasma interaction." Physical Review Letters **71**(17): 2725-2728.

Hanson, R. K. (1974). "Shock-tube study of carbon monoxide dissociation kinetics." The Journal of Chemical Physics **60**(12): 4970-4976.

Hardy, J. E., et al. (1978). "Recombination of carbon monoxide and oxygen atoms." International Journal of Chemical Kinetics **10**(5): 503-517.

Hassouni, K., et al. (2006). "Formation of soot particles in Ar/H2/CH4 microwave discharges during nanocrystalline diamond deposition: A modeling approach." Pure and Applied Chemistry **78**(6): 1127-1145.

Hercher, M. (1964). "Laser-induced damage in transparent media." Journal of the Optical Society of America **54**: 563.

Huber, K. and G. Herzberg (1979). Molecular Spectra and Molecular Structure. IV. Constants of Diatomic Molecules. New York, New York, Van-Nostrand-Reinhold.

Huczko, A. and A. Szymański (1984). "Thermal decomposition of carbon dioxide in an argon plasma jet." Plasma Chemistry and Plasma Processing **4**(1): 59-72.

Jacobs, C., et al. (2013). Vacuum ultraviolet radiation studies in a plasma torch facility. 44th AIAA Thermophysics Conference.

Jiang, N., et al. (2024). "Long-lived nitric oxide molecular tagging velocimetry with 1 + 1 REMPI." Optics Letters **49**(5): 1297-1300.

Johnston, C. O. and A. M. Brandis (2014). "Features of Afterbody Radiative Heating for Earth Entry." Journal of Spacecraft and Rockets **52**(1): 105--119.

Johnston, C. O. and A. M. Brandis (2014). "Modeling of nonequilibrium CO Fourth-Positive and CN Violet emission in CO2–N2 gases." Journal of Quantitative Spectroscopy and Radiative Transfer **149**: 303-317.

Johnston, C. O., et al. (2013). Radiative Heating Uncertainty for Hyperbolic Earth Entry, Part 1: Flight Simulation Modeling and Uncertainty.

Kato, H., et al. (2007). "Excitation of the A2Σ+, C2Π and D2Σ+ Rydberg-electronic states in NO by 100eV electrons." Chemical Physics Letters **444**(1): 34-38.

Kirby, K. and D. L. Cooper (1989). "Theoretical study of low-lying $^1^+$ and $^1\Pi$ states of CO. II. Transition dipole moments, oscillator strengths, and radiative lifetimes." The Journal of Chemical Physics **90**(9): 4895-4902.

Klose, J. Z., et al. (1988). "Radiometric Calibrations of Portable Sources in the Vacuum Ultraviolet." Journal of Research of the National Bureau of Standards **93**(1): 21-39.

Kobayashi, A., et al. (2002). "Treatment of CO_2 gas by high-energy type plasma." Vacuum **65**(3): 475-479.

Kondratiev, V. N. and E. I. Intezarova (1969). "Interaction between CO and O." International Journal of Chemical Kinetics **1**(1): 105-111.

Kozák, T. and B. Annemie (2014). "Splitting of CO_2 by vibrational excitation in non-equilibrium plasmas: a reaction kinetics model." Plasma Sources Science and Technology **23**(4): 045004.

Kozák, T. and A. Bogaerts (2015). "Evaluation of the energy efficiency of CO2 conversion in microwave discharges using a reaction kinetics model." Plasma Sources Science and Technology **24**(1): 015024.

Kramida, A., et al. (2018). NIST Atomic Spectra Database (version 5.6.1).

Langhoff, S. R., et al. (1988). "Theoretical study of the NO γ system." The Journal of Chemical Physics **89**(8): 4909-4917.

Laux, C. (1993). Optical Diagnostics and Radiative Emission of Air Plasmas. Dept. of Mechanical Engineering, Stanford University. **PhD**.

Laux, C., et al. (1993). Modeling the UV and VUV radiative emission of high-temperature air. 28th Thermophysics Conference, American Institute of Aeronautics and Astronautics.

Laux, C., et al. (2009). Influence of Ablation Products on the Radiation at the Surface of a Blunt Hypersonic Vehicle at 10 km/s. 41st AIAA Thermophysics Conference.

Laux, C. O., et al. (2001). "Rotational temperature measurements in air and nitrogen plasmas using the first negative system of N_2^+." Journal of Quantitative Spectroscopy and Radiative Transfer **68**(4): 473-482.

Laux, C. O. and C. H. Kruger (1992). "Arrays of radiative transition probabilities for the N$_2$ first and second positive, NO beta and gamma, N$^+_2$ first negative, and O$_2$ Schumann-Runge band systems." Journal of Quantitative Spectroscopy and Radiative Transfer **48**(1): 9-24.

Laux, C. O., et al. (2012). "State-to-state modeling of a recombining nitrogen plasma experiment." Chemical Physics **398**: 46-55.

Laux, C. O., et al. (2003). "Optical diagnostics of atmospheric pressure air plasmas." Plasma Sources Science and Technology **12**(2): 125-138.

Lavrov, B. (1991). Calculation of Thermodynamic Functions for N2, O2 and NO. Stanford, CA.

Lebouvier, A., et al. (2013). "Assessment of Carbon Dioxide Dissociation as a New Route for Syngas Production: A Comparative Review and Potential of Plasma-Based Technologies." Energy & Fuels **27**(5): 2712-2722.

Li, J., et al. (2017). "Dissociation of CO2 by thermal plasma with contracting nozzle quenching." Journal of CO2 Utilization **21**: 72-76.

Limbach, C., et al. (2016). Laser Light Scattering from Equilibrium, High Temperature Gases: Limitations on Rayleigh Scattering Thermometry. 47th AIAA Plasmadynamics and Lasers Conference, American Institute of Aeronautics and Astronautics.

MacDonald, M. E., et al. (2014). "Measurements of Air Plasma/Ablator Interactions in an Inductively Coupled Plasma Torch." Journal of Thermophysics and Heat Transfer **29**(1): 12-23.

McBride, B. J. and S. Gordon (1992). Computer Program for Calculating and Fitting Thermodynamic Functions.

McBride, B. J., et al. NASA Glenn Coefficients for Calculating Thermodynamic Properties of Individual Species.

McGuire, S. D., et al. (2017). "Ultraviolet Raman spectroscopy of N_2 in a recombining atmospheric pressure plasma." Plasma Sources Science and Technology **26**(11): 115005.

Miescher, E. (1978). "The I2Σ+ state of the NO molecule." Journal of Molecular Spectroscopy **69**(2): 281-293.

Nagulapally, M., et al. (1998). Numerical simulation of nonequilibrium nitrogen and air plasma experiments. 29th AIAA, Plasmadynamics and Lasers Conference, American Institute of Aeronautics and Astronautics.

Oberreuther, T., et al. (2003). "Volumetric plasma chemistry with carbon dioxide in an atmospheric pressure plasma using a technical scale reactor." IEEE Transactions on Plasma Science **31**(1): 74-78.

Olejniczak, J., et al. An Analysis of the Radiative Heating Environment for Aerocapture at Titan. 39th AIAA/ASME/SAE/ASEE Joint Propulsion Conference and Exhibit.

Pannier, E. and C. O. Laux (2019). "RADIS: A nonequilibrium line-by-line radiative code for CO2 and HITRAN-like database species." Journal of Quantitative Spectroscopy and Radiative Transfer **222-223**: 12-25.

Park, C. (1993). "Review of chemical-kinetic problems of future NASA missions. I - Earth entries." Journal of Thermophysics and Heat Transfer **7**(3): 385-398.

Park, C., et al. (1994). "Review of chemical-kinetic problems of future NASA missions. II - Mars entries." Journal of Thermophysics and Heat Transfer **8**(1): 9-23.

Partridge, H., et al. (1990). "Theoretical study of the spectroscopy of NO+." The Journal of Chemical Physics **93**(10): 7179-7186.

Paulussen, S., et al. (2010). "Conversion of carbon dioxide to value-added chemicals in atmospheric pressure dielectric barrier discharges." Plasma Sources Science and Technology **19**(3): 034015.

Pilling, M. J., et al. (1971). "A curve of growth determination of the f-values for the fourth positive system of CO and the Lyman-Birge-Hopfield system of N2." Journal of Quantitative Spectroscopy and Radiative Transfer **11**(11): 1593-1604.

Ponduri, S., et al. (2016). "Fluid modelling of CO_2 dissociation in a dielectric barrier discharge." Journal of Applied Physics **119**(9): 093301.

Qu, Q., et al. (2021). "A spectroscopic model for the low-lying electronic states of NO." The Journal of Chemical Physics **154**(7): 074112.

Richard, B. M., et al. (2001). "Laser Rayleigh scattering." Measurement Science and Technology **12**(5): R33.

Schadee, A. (1978). "Unique definitions for the band strength and the electronic-vibrational dipole moment of diatomic molecular radiative transitions." Journal of Quantitative Spectroscopy and Radiative Transfer **19**(4): 451-453.

Sheehy, J. A., et al. (1994). "Theoretical study of the nitric oxide ϵ and 11000 Å bands." Chemical Physics Letters **225**(1): 221-228.

Slanger, T. G., et al. (2003). "Kinetics of O(3P) +CO +M Recombination." The Journal of Chemical Physics **57**(1): 233-238.

Spielfiedel, A., et al. (1999). "Ab initio calculation of the dipole transition moment and band oscillator strengths of the CO (A-X) transition." Astronomy and Astrophysics **346**: 699-704.

Sprangle, P., et al. (2004). "Ultrashort laser pulses and electromagnetic pulse generation in air and on dielectric surfaces." Physical Review E **69**(6): 066415.

Studer, D. and P. Vervisch (2007). "Raman scattering measurements within a flat plate boundary layer in an inductively coupled plasma wind tunnel." Journal of Applied Physics **102**(3).

Swenson Jr., L. S., et al. (1989). "This New Ocean: A History of Project Mercury." from https://history.nasa.gov/SP-4201/toc.htm.

Tailliez, C., et al. (2020). "Terahertz pulse generation by two-color laser fields with circular polarization." New Journal of Physics **22**(10): 103038.

Tetard, G., et al. (2022). "Molecular growth paths and dust-particles nucleation precursors in Ar/C2H2 low pressure discharges." Plasma Processes and Polymers **19**(5): 2100204.

Thiele, I., et al. (2016). "Theory of terahertz emission from femtosecond-laser-induced microplasmas." Physical Review E **94**(6): 063202.

Thompson, B. A., et al. (1963). "Ultraviolet absorption coefficients of CO2, CO, O2, H2O, N2O, NH3, NO, SO2, and CH4 between 1850 and 4000 A." Journal of Geophysical Research (1896-1977) **68**(24): 6431-6436.

Tibère-Inglesse, A. (2019). Radiation of non equilibrium recombining plasma flows. Science mécaniques et énergétiques, Université Paris-Saclay.

Tibère-Inglesse, A. C., et al. (2023). "Inferring gas temperature from N2 emission via rotational distribution of the N2 B3Πg and C3Πu states." Plasma Sources Science and Technology **32**(7): 075018.

Tibère-Inglesse, A. C., et al. (2021). "Measurements and analysis of rotational temperatures obtained with Raman and optical emission spectroscopy in a nonequilibrium nitrogen plasma." Plasma Sources Science and Technology **30**(12): 125019.

Warnatz, J. (1984). Rate Coefficients in the C/H/O System. Combustion Chemistry. New York, New York, Springer**:** 197-360.

Watanabe, K. Z. and E. Inn (1953). Absorption coefficients of several atmospheric gases. Technical Report 53-23 Air Force Cambridge Research Center.

Whiting, E. E., et al. (1980). "Recommended conventions for defining transition moments and intensity factors in diatomic molecular spectra." Journal of Molecular Spectroscopy **80**(2): 249-256.

Wright, M., et al. (2019). The Dragonfly Entry and Descent System. NASA Technical Report.

Yang, T., et al. (2018). "Understanding CO2 decomposition by thermal plasma with supersonic expansion quench." Plasma Science and Technology **20**(6): 065502.